Title

Synthesis, Characterization, and Integration of Silicon Nanowires for Nanosystems Technology

Author

Doerk, Gregory Stephen

Publication Date

2010

Synthesis, Characterization, and Integration of Silicon Nanowires for Nanosystems Technology

by

Gregory Stephen Doerk

A dissertation submitted in partial satisfaction of the
requirements for the degree of
Doctor of Philosophy

in

Chemical Engineering

in the

Graduate Division

of the

University of California, Berkeley

Committee in charge:

Professor Roya Maboudian, Chair
Professor Jeffrey Reimer
Professor Liwei Lin

Fall 2010

Synthesis, Characterization, and Integration of Silicon Nanowires for Nanosystems Technology

Abstract

Synthesis, Characterization, and Integration of Silicon Nanowires for Nanosystems Technology

by

Gregory Stephen Doerk

Doctor of Philosophy in Chemical Engineering

University of California, Berkeley

Professor Roya Maboudian, Chair

Silicon's chemical stability, high natural abundance (as the second most common element in the earth's crust), mechanical stiffness, and semiconducting behavior have made it the subject of extensive scientific investigation and the material of choice for both the microelectronics and microelectromechanical device industries. The success of Moore's Law that demands continual size reduction has directed it to a central place in emerging nanoscience and nanotechnology as well. Crystalline nanowires (NWs) are one nanostructured form that silicon may take that has sparked significant interest as they can exhibit considerable confinement effects and high surface-to-volume ratios, but may be interfaced simply along one direction for the determination of material properties and implementation into new technologies. The expense and difficulty involved in the creation of semiconductor nanowires using the "top down" fabrication techniques of the microelectronics industry has promoted an explosion of chemical synthetic "bottom up" techniques to produce high quality crystalline nanowires in large quanitities. Nevertheless, bottom up synthesized Si NWs retain a new set of challenges for their successful integration into reliable, high-performance devices, which is hindered by an incomplete understanding of the factors controlling their material properties.

The first chapter of this dissertation introduces the motivation for studying semiconductor NWs and the benefits of limiting the scope to silicon alone. A brief survey of the current understanding of thermal conductivity in silicon nanowires provides prime examples of how confinement effects and surface morphology may dramatically alter nanowire properties from their bulk crystal counterparts. The particular challenges to bottom up silicon nanowire device integration and characterization are noted, especially related to Si nanowires that are grown epitaxially on crystal silicon substrates, and Raman spectroscopy is introduced as a promising optical characterization and metrology tool for semiconductor nanowire-based devices.

Chapter two describes the vapor-liquid-solid (VLS) mechanism for the synthesis of very high quality, single-crystal silicon nanowires using Au and Pt catalyst nanoparticles. A new

technique is presented for the simplified synthesis of branched silicon nanowires based on the migration of Au catalyst during an hydrogen anneal intermediate between growth stages, and the faceting behavior at synthetic stages is revealed by the analysis of electron microscope images. Synthesis of solid and porous Si nanowires based on Ag-mediated electrochemical silicon etching is described as well.

The third chapter specifies new processing techniques developed with future device integration of epitaxially VLS-grown Si nanowires in mind. Epitaxially bridging nanowires are shown to provide an excellent platform for single-wire electrical and mechanical property measurements. Galvanic displacement through block copolymer micelle/homopolymer surface templates is demonstrated as a means to deposit catalyst nanoparticles with controlled sizes and areal densities in a variety of geometries and with registration to photolithographic patterns. *Ex situ* boron doping by the direct hydrogen reduction of boron tribromide is shown to achieve active concentrations exceeding 10^{19} cm^{-3} with high axial uniformity, while avoiding the adverse impact on nanowire morphology that is often observed with *in situ* boron doping of silicon nanowires.

Chapter four describes the characteristics of Raman spectroscopy that are relevant to studying individual semiconductor nanowires. Careful spectral measurements show that the anharmonic dependence of Raman spectra on temperature for individual Si nanowires remains unchanged from the bulk crystal for diameters down to 30 nm, regardless of surface morphology. Using this result, a new technique for measuring the thermal conductivity of individual semiconductor nanowires is then outlined based on Raman thermal mapping of individual cantilevered nanowires.

Finally, the dissertation is concluded with suggestions for possible future experiments. One avenue is to probe more deeply the morphology of faceted silicon nanowires and nanotrees and its impact on their transport physics. Another possible route for further study would be to explore new characterization and metrological applications of Raman spectroscopy for semiconductor nanowires.

In loving memory of my father.

Contents

Acknowledgments

To start I would like to thank my advisor Roya Maboudian. She has always been keen and enthusiastic when experiments work; patient and helpful when they do not. The freedom she has given in allowing me to direct much of my own research has helped reveal to me the true pleasure of scientific experimentation and discovery, and instills in me a profound sense of how I hope to guide others in future research. She has also provided me with invaluable guidance throughout my graduate school education and found time to meet with me whenever I needed it. Such an asset is not available to all graduate students.

I am also indebted to Carlo Carraro for his extremely helpful consultations, insight and support. He has helped me considerably in understanding the theory behind many of the measurements used during research, particularly in the case of Raman spectroscopy.

A number of collaborators deserve special thanks for their contributions. Under the guidance of Velimir ("Mimo") Radmilovic, my understanding and skill in transmission electron microscopy has improved prodigiously and I realized the great care that must be taken in interpreting electron microscope images. My work at the National Center for Electron Microscopy would not be possible without the assistance of various staff members there, especially John Turner, Doreen Ah Tye and Cheng Yu Song. I am also deeply grateful for the generosity of other collaborators. Megan Lane Hoarfrost and Professor Rachel Segalman freely provided the polymers used for the micelle templating and advice for their use. While as a postdoctoral scholar in the Zettl group, Haibing Peng kindly spent much of his time to help me perform nanowire mechanical resonance measurements. Dr. J Provine in the group of Roger Howe at Stanford performed focused-ion-beam work with me in the darkest hours of the morning. Erik Garnett taught me how to make contacts to individual nanowires using electron beam lithography. I would also like to thank other collaborators and colleagues that I have worked with at various stages of my graduate tenure, including Dr. Alvaro San Paulo, Marta Fernandez, Prof. Nancy Haegel at the Naval Postgraduate School, Prof. Bahman Farahani, Prof. Farzineh Rajabi, and Johnny Ho. I also would like to acknowledge the valuable insights provided by Prof. Jeffrey Reimer and Prof. Liwei Lin as members of my dissertation committee.

I am thankful to many people within the Maboudian group, past and present. Noel Arellano helped me immensely in the early years of my graduate period, and postdoctoral scholar Nicola Ferralis has played a large part in developing my scientific perspective (by engaging with me in many fun, thought provoking discussions). I am forever grateful for the aid, training, advice, and encouragement provided by other members of the lab including Ian Laboriante, Dae Ho Lee, Albert Gutes, Mohammed (Kamran) Shavezipur, Fang Liu, John Alper, Ben Hsia, Guohua Li, Yongkwan Kim, Brian Bush, Chris Roper, Calvin DaRosa, Jingchun Zhang, Wei Cheng Lien, Melitta Hon, Marta Cerruti and Frank DelRio. I have also had the pleasure to work with Gabriella Lestari, Christine Politi (during a summer REU under the aegis of COINS), and Charles Dhong – three bright, inquisitive undergraduates who have contributed significantly to the work presented here, particularly the doping and

block copolymer work.

I am grateful to the College of Chemistry shops, particularly Eric Granlund in the machine shop; Aileen, Rocio, Trish, and all of the departmental administrative support; and the Microlab staff. I am very appreciative of the COINS program, not only for financial support, but for the opportunity to interact and engage in a scholarly forum outside my own lab. Through COINS I have met and become friends with a number of very intelligent, thoughtful people.

I deeply appreciate the many great friendships I have developed at Berkeley. Paul Albertus and Anthony Goodrow were great running pals and willing to put up with my sometimes brilliant, often inane conversations. Katie, Rodrigo, and Zach made the time on long bike rides go by too fast. Cathy and Monica brought me into the world of salsa dancing, to which I will hopefully soon return. Paul made me realize that scientific rigor and artistic acuity are complementary. I also look back fondly at many a summer softball game as a member of his team. Megan Fox is a wonderful person, and I have enjoyed lively debates and delicious baked goods for which she was both responsible. Her value far exceeds the actress of the same name, at least in the small part of the world I occupy. Since being a GSI with her, Priya has been a constant friend. I am always amazed by how well (and how quickly) she can do so many things, from running to painting. Many other friends have elevated my graduate school experience including Brian, Matt, Marisa, Tim, Lisa, Bean, Kyle, Jesse, Cathleen, Sarah, Mike Liszka, Mike Zboray, Penny, Joel, Barbara, Alison, Paul Cordeiro, Tyler, and Dana. There are others forgotten from the list here, but not forgotten in my memory.

I also had simply awesome roommates. Will's southern charm (and sometimes southern cooking) leaves an indelible impression on everyone you meet and I am no different. I also learned much about economics from him. I would tell him to keep smiling, but that is probably a foregone conclusion. Nisita is possibly the best roommate I have had. Living over 5 years together we have grown pretty close, most evident in the fact that we often finish each others sandwiches. Her emails of otter and kitten pictures always brightened my day.

Finally, none of this would be possible without the love and support of my family. My sister Denise showed me the value of working hard if you really want to achieve something personally important, while my brother Bryan sparked much of my intellectual curiosity at an early age. I also thank my grandmother Edna for her loving wishes and prayers, and the rest of my family who has always had confidence in me when my own was lacking. Finally I thank my mother Marleen for her unconditional love. She was at the receiving end of many phone calls where I expressed frustration when things were not always working out as I hoped, but she never tired. The values she brought me up with are the basis for all the successes I have had.

Chapter 1

Introduction

Nanowires (NWs) are high-aspect-ratio solid structures with sizes confined to several hundred nanometers or less in two dimensions (i.e. having an effective diameter less than several hundred nanometers), but that are much longer in the third. Since the emergence of carbon nanotubes as an academic research interest in the 1990s [1] there has been an immense increase in research both in synthesizing NWs (and related nanostructures) and in characterizing their properties. NWs are usually larger in diameter than carbon nanotubes, and their three-dimensional crystal structures – rather than a structure based upon rolled-up graphene as found in carbon nanotubes – renders physical behavior that is at times somewhat less striking; it also makes their possible integration into new technology more straightforward. This is particularly appropriate in the case of semiconducting NWs, which will be discussed exclusively from this point on (In fact, most of the focus will be entirely on Si NWs).

NWs may be fabricated according to two general strategies. The "top down" approach leverages the technologies, processes, and techniques currently used in micro- or nanofabrication for the fabrication of NWs. On the other hand, the "bottom up" approach achieves the synthesis of NWs through chemical processes and/or self-assembly. NWs fabricated by either approach, yet possessing the same final form (i.e. equal crystallinity, composition, size, morphology, defect density, surface roughness, etc...), should exhibit the same properties. The desire to integrate NW components into emerging technology recommends the top down strategy. However, there are potential advantages to the bottom up route. First, bottom up methods may be used to synthesize large quantities of nanostructures with unique structures or morphologies that are impossible or prohibitively difficult to create using strictly top down methods. Under the NW classification of nanostructures, these include axial NW superlattices [2], core-shell NWs [3], and branched NWs or "nanotrees" [4]. Secondly, even for simple nanostructures (e.g. elemental NWs) it may be possible to produce them in higher quantities less expensively through bottom up synthesis rather than top down fabrication. In cases where pattern registry and nanostructure uniformity are not critical, bottom up strategies may be applied directly to emerging technologies. In other cases, substantial improvements in methods to integrate chemically synthesized nanostructures into devices are necessary.

1.1 Motivation for Studying Nanowires

There are three major reasons – with substantial overlap among them – that NWs may be technologically useful and scientifically interesting, engendering a substantial research effort towards their fabrication and characterization. One is the emergence of confinement effects in nanostructures. Perhaps the best-known example, commonly referred to as "quantum confinement", is the increasing electronic bandgap in semiconductor nanostructures when the wire diameter is on the order of the exciton Bohr radius for that material [5]. The term "confinement effect" as used here though refers to a broader set of phenomena that stem from the parity of the confined dimension (the diameter) with important nanometer-scale characteristic lengths. For instance, dielectric mismatch between the NW and its surrounding medium gives rise to resonant interactions with electromagnetic radiation when the wavelength of the incident field is commensurate with the radial dimension of the NW [6]. This in turn manifests as optical absorption resonances [7] and large polarization anisotropies [8].

Another key characteristic generating interest in NWs is their increased surface-to-volume ratio, which scales as $\sim 1/D$, where D is the NW diameter. Surfaces break the translational symmetry inherent in crystal lattices and thus properties of a crystal are often substantially different at their surfaces than in the bulk. Many macroscopically measured crystal attributes are in fact a combination of bulk and surface properties, so as the surface-to-volume ratio increases the characteristics of the surface contribute more, and eventually dominate, the measured behavior. This is particularly evident in the electronic properties of NWs at diameters where quantum confinement is not significant. These NWs are depleted of charge carriers at their surfaces due to interface states and trapped charges in the native oxide [9], as well as increased donor ionization energies as a result of dielectric mismatch with the surrounding medium [10]. As a result NW electrical *resistivities* increase with decreasing diameter. Thus, higher doping levels or careful surface passivation is necessary for using NWs in electronic applications. On the other hand, this sensitivity to surface charge implies that NWs may serve as the basis of extremely effective chemical and biological sensors [11].

A third reason promoting the investigation of NWs is their inherent small size (relative only to larger wires or beams). The simplicity of this reason cannot demean its potentially great technological impact, just as downscaling has lead to serious improvement in electronics for a long period in which the fundamental physics behind transistors has changed relatively little. An exemplary case is the NW-based nanomechanical resonator [12], which promises ultrasensitive mass or force detection through monitoring shifts in the mechanical resonance frequency. The most basic definition for a resonance frequency (ω_o) is derived from the simple harmonic oscillator model:

$$\omega_o = \sqrt{\frac{k_{eff}}{m_{eff}}} \tag{1.1}$$

where k_{eff} is the effective spring constant and m_{eff} is the effective mass of the resonator. In real systems that are damped, mechanical resonators are characterized by the ratio of energy stored to energy lost in a single period, a figure of merit known as the “quality factor” Q, effectively given by $Q = \omega_o/\Delta\omega$, where $\Delta\omega$ is the full width at half maximum of the resonance peak. The quality factor is inversely proportional to the strength of damping. Mass added to the resonator, say by molecular adsorption, redshifts the resonance frequency. When the adsorbed mass is much less than the resonator effective mass, the sensitivity of the frequency shift ($\delta\omega$) to the adsorbed mass (δm) is given by:

$$\frac{\delta\omega}{\delta m} = \frac{\omega_o}{2m_{eff}}. \tag{1.2}$$

Assuming that the minimal frequency shift should be larger than $\Delta\omega$, the minimum mass sensitivity is

$$\delta m_{min} \approx \frac{2m_{eff}}{Q} \tag{1.3}$$

Thus, a nanomechanical resonator exhibits higher mass sensitivity the smaller it is if high quality factors can be maintained.

1.2 Why Silicon?

The research presented in this dissertation addresses NWs synthesized *via* bottom up processes. While one of the advantages of bottom up NW synthesis is the wide material accessibility while maintaining excellent crystal qualities, the focus herein will be on Si only. The reasons for studying Si NWs alone are both practical and fundamental.

Si is the second most abundant element in the earth’s crust [13] thus incurring no scarcity costs, though the energy required to isolate and purify elemental Si crystals can increase cost proportionally to the required purity. Si is also considered non-toxic, unlike a number of binary compound semiconductors, such as those based on cadmium [14]. Furthermore, Si is the dominant material for micro- and nanoelectronics. In the past this could be attributed to the high stability and quality of thermally grown SiO_2 that was crucial for gate dielectrics [15]. With the adoption of high permittivity gate dielectrics based on rare-earth oxides (HfO_2 for example), it may be acknowledged that a certain momentum supports the continuing use of Si; the backing of an entire industry inhibits the use of more exotic materials that may involve wholesale adjustment of industry standard technologies, processes, and design rules. The de facto use of Si wafers as substrates for integrated circuits, and the common availability of equipment designed optimally to process Si has promoted its use as the material of choice for micro- and nanoelectromechanical systems (MEMS and NEMS, respectively), and is stimulating research in silicon photonics [16]. In the foreseeable future, the integration of many devices based on NWs into realistic platforms will demand stringent compatibility with Si. Si NWs are the most likely kind to fit this requirement.

Due to its prevalance in nanoelectronics and NEMS, Si is also one of the most thoroughly-investigated materials. As a results, many of its bulk properties are well-known and understood, which is particularly important when transitioning from the study of bulk materials to nanomaterials. High surface-to-volume ratios and confinement effects in NWs can lead to profoundly different characteristics from their bulk counterparts that are often affected by surface morphology, elemental composition distribution, and geometric shape. In many cases, the new characteristics are unexpected and difficult to fully understand. Having a firm grasp on the intrinsic crystal properties of Si, even in bulk form, aids in understanding the ways in which the qualities of its derivative nanostructures are modified by their distinctive morphologies.

1.3 Nanowire Thermal Properties

The thermal conductivity of semiconductor NWs provides an instructive example of a substantially altered property due to both confinement effects and high relative surface areas. Understanding the thermal conductivity in NWs is important for a number of applications. For instance, electron mobility in semiconductors is a strong function of temperature [17], so heat dissipation must be carefully managed in electronic devices based on NWs to ensure steady and reliable operation. Rational thermal conductivity reduction may also be valuable for the development of energy-harvesting technologies, particularly those based on thermoelectric materials. Thermoelectric devices generate an electrical potential difference across a temperature difference based on the thermal diffusion of electronic free carriers, and their efficacy is characterized by the dimensionless figure of merit ZT given by

$$ZT = \frac{\sigma S^2}{k_e + k_p} T \tag{1.4}$$

where T is temperature, σ is the electrical conductivity, S is the Seebeck coefficient or thermopower (the ratio of the potential difference to the temperature difference), k_e is the thermal conductivity for electrons, and k_p is the thermal conductivity for phonons, or quantized lattice vibrations. Keeping all other parameters the same, reducing thermal conductivity will improve ZT. In metals, electons dominate heat conduction, while in semiconductors and insulators heat transport occurs primarily through phonons. The electron thermal conductivity is in most cases directly proportional to the electrical conductivity through the Wiedemann-Franz Law [18] and the high electrical conductivity of metals tends to grant them high electronic thermal conductivities, making them poor thermoelectric materials.

Semiconductors on the other hand may exhibit highly decoupled electrical and thermal conductivities according to the different carriers involved, and thus may be engineered to improve their thermoelectric performance. Since Si is a semiconductor, phonon thermal conductivity is discussed here.

The diffusive transport of phonons may be described by analogy with the kinetic theory of gases, whereby the following simple expression for phonon thermal conductivity may be derived:

$$k_p = \frac{1}{3}Cvl. \tag{1.5}$$

In this equation,C, v and l are the phonon heat capacity, group velocity, and mean free path. The mean free path is limited by scattering from crystal defects, impurities, electrons, crystal boundaries, or other phonons (and possibly other mechanisms). Various expressions are used to estimate limiting mean free paths for scattering by each mechanism, and a composite effective mean free path that goes into (1.5) is determined by applying Matthiessen's rule for multiple scattering, such that

$$\frac{1}{l} = \sum_i \frac{1}{l_i} \tag{1.6}$$

where l_i is the mean free path for the i^{th} scattering mechanism.

Phonon confinement is reflected directly in the reduction in the phonon mean free path due to scattering at the crystal boundaries. A commonly accepted expression for the phonon mean free path due to boundary scattering ($l_{boundary}$) is [19]

$$l_{boundary} = \left(\frac{1+p}{1-p}\right) D. \tag{1.7}$$

In this expression, p is the degree of specularity that reflects the wave nature of phonons. For a value of 1 (pure specular reflection) the incident wave reflects coherently off the boundary as if from a mirror, giving the same angle with the surface normal in the reflected wave as the incident wave. A value of zero implies purely diffuse, or random, scattering at a rough surface. The value of p is usually estimated according to the expression (strictly valid only phonons at normal incidence, but applied generally)

$$p = \exp\left[-\pi\left(\frac{4\pi\eta}{\lambda}\right)^2\right] \tag{1.8}$$

where λ is the appropriate phonon wavelength and η is the characteristic surface roughness. At room temperature, a typical wavelength for a phonon in Si is less than a few nanometers [20], whereas surface roughnesses are at best still greater than a few hundred picometers. The end result is that almost all phonon boundary scattering is effectively diffuse, and $l_{boundary} \approx D$. With fairly minor adjustment, thermal conductivity modeling including this boundary scattering term is able to match experimentally measured values [21] quite well for smooth-surfaced Si NWs diameters larger than ~35 nm and especially near room temperature [22].

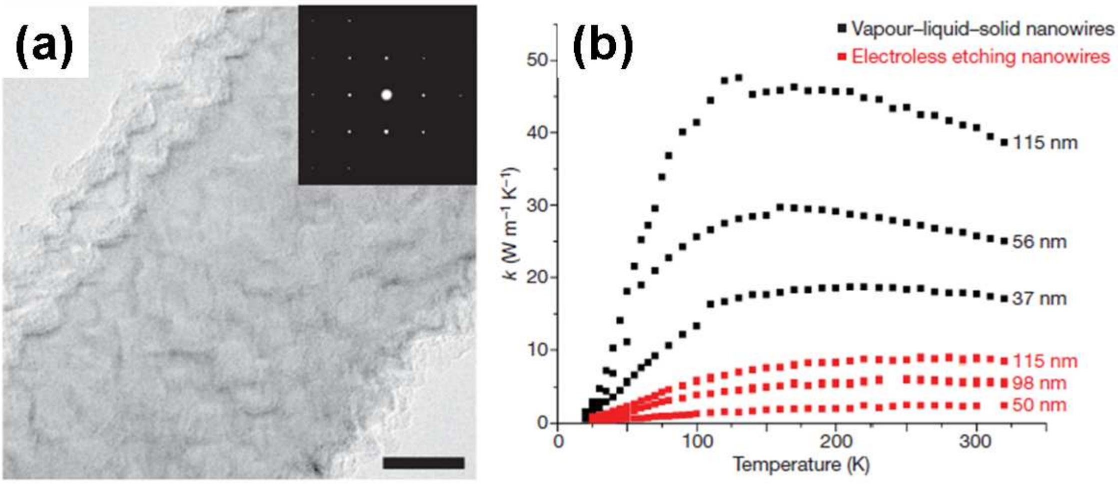

Figure 1.1: (a) Transmission electron microscope image of a single crystal Si NW with rough surfaces (scale bar = 20 nm). (b) Measured thermal conductivity values for individual Si NWs with smooth surfaces ("Vapour-liquid-solid") compared to those with rough surfaces ("Electroless etching"). The thermal conductivity values of rough-surfaced Si NWs are substantially reduced for the same diameter. Adapted by permission from Macmillan Publishers Ltd: Nature (v. 451, p. 163, 2008), copyright (2008) [24].

Significant discrepancies arise for smaller diameter Si NWs at temperatures less than 100 K; for such cases, it has been suggested that a portion of the phonons possess boundary scattering mean free paths that depend on the phonon frequency [23].

According to the basic boundary scattering model given above, no further reduction in the boundary scattering mean free path is expected by increasing surface roughness. Yet, Si NWs with very rough surfaces (~1-5 nm) such as one shown in the TEM image in Fig. 1.1(a) exhibit an astonishingly reduced thermal conductivities in comparison to smooth-surfaced Si NWs possessing approximately the same diameters. Sample measurements of both types ("Vapour-liquid-solid" = smooth, "Electroless etching" = rough) from cryogenic temperatures to above room temperature are depicted in Fig. 1.1(b) [24]. All the rough Si NWs show substantially lower thermal conductivities compared to their smooth counterparts, in some cases showing a reduction of one order of magnitude. Due to this dramatically reduced thermal conductivity, the ZT of a ~50 nm diameter rough Si NW was measured to be as high as ~0.6 at room temperature – almost two orders of magnitude better than bulk Si and approaching current values available for commercially available thermoelectric devices [24]. The role of confinement and surface structuring in controlling the thermal conductivity of these Si NWs demonstrates a prime example how nanostructuring may lead to technologically relevant new materials.

At the time these measurements were presented, no theories were available to adequately explain this precipitous drop in thermal conductivity with high surface roughness, but in the following years a few models have been posited. Martin *et al.* invoked the use of a perturbation approach analogous to previous computations of electron transport in transistor inversion layers with surface roughness, including the full phonon dispersion relation for Si and frequency dependent phonon scattering rates [25]. Kazan et al, on the other hand modelled the system in a computationally intensive adaptation of more traditional phonon thermal conductivity equations utilizing optical phonon decay to acoustic phonons as well as frequency, incident angle, and roughness dependent boundary scattering [26]. Both approaches obtain very good agreement with the (scant) available experimental data from Ref. [24], which leaves some doubt about the essential details of the underlying physics. Donadio and Galli showed through a combination of computational approaches that disordering of Si NW surfaces results in decreased lifetimes of propagating phonon modes via decay to non-propagating modes [27]. Unfortunately, the calculations were only possible for very small scale Si NWs ($<\sim$4 nm in diameter), making the extension of the results to larger diameter NWs tenuous. Nevertheless, the physical implications are fairly clear. Regardless of the computational models used to reproduce the available data, further experiments and the accumulation of larger, more varied data sets should aid in improving our understanding of the physics of thermal transport in nanostructures.

1.4 Challenges to Nanowire Device Integration and Characterization

The fabrication of NWs by top down routes often includes their implicit integration into structures where they may be used optimally in devices. The same is not true for NWs synthesized by bottom up processes. One of the most prominent bottom up routes for the synthesis of NWs and related structures is vapor-liquid-solid (VLS) growth, where NWs are grown via chemical vapor epitaxy mediated by liquid metal or metal-alloy nanodroplets (described in more detail in the following chapter). VLS synthesis enables the growth of high quality single crystal NWs and related heterostructures [2, 3, 4] over an extensive range of semiconducting materials, portending great promise for its use in future technologies. Indeed single VLS-grown NW devices have been demonstrated in numerous application areas including nanoelectronics [28], photonics [29], and sensing [11]. However, the full potential of NW-based devices cannot be realized without the development of large scale, high yield device integration strategies with accurate spatial registry. For NWs synthesized by the VLS method in general, devices are fabricated either on NWs that have been transferred from the growth substrate to a separate device substrate, or from NWs that have been grown epitaxially in the location and geometry desired for the device, as directed by the relation between the orientation of the substrate surface and the NW preferred growth orientation. While post-growth assembly techniques have advanced impressively towards achieving large scale NW device integration [30, 31], this integration problem remains acute for devices composed of epitaxially grown semiconductor NWs.

This severely hinders the development of technology utilizing the unique advantages of epitaxial VLS-grown NWs. For instance, vertical NWs grown epitaxially on a flat substrate with the right crystal orientation may serve as the basis for cellular biomolecular delivery platforms [32], photovoltaics [33], and three-dimensional integrated circuits [34, 35]. In ideal cases, the position and size of each vertical nanowire is determined by the same characteristics in the predeposited metallic nanoparticle (NP) that serves as the growth catalyst. Electron beam lithography may be used to control catalyst particle placement for epitaxial NW growth [36, 37], but its high cost and serial nature make it unsuitable for large scale processing. Colloidal metal NPs offer a possible lower cost solution, and a number of techniques for positioning Au colloids (and hence the resulting NWs) have emerged [38, 39, 40, 41], even to the extent of single NP resolution [40]. However, the range of particle densities per unit area may be limited depending on the technique, and accurate placement of a small number of catalyst NPs (1-3) still requires high resolution nanolithography ($<\sim$200 nm) that will likely drive up costs. Moreover, these patterning stategies may not be easily applied to substrates with varied topography (i.e. not flat). This is critical in case of fabricating epitaxially bridging VLS-grown NWs in microtrenches, where features such as rigid mechanical clamping [42] and ultra-low electrical contact resistances [43] promote their use in potential applications such as rapid microfluidic biosensors [44], directly grown logic gates and photovoltaic devices [45], horizontal wrap-gate transistors [46], and nanomechanical resonant NW mass sensors [47]. Nevertheless, to date the placement of Au colloids on trench sidewalls is still essentially random.

As made apparent in the previous section, the properties of semiconductor NWs may be difficult to predict and are often highly sensitive to their sizes and morphologies. This presents another major roadblock to the development of new technologies based on NWs, where key properties must be well-understood and controlled. Though precise methods have been developed to measure vital properties and characteristics of NW-based devices, there are notable deficiencies in current characterization techniques. In line with the previous section, methods to measure thermal conductivities of axial nanostructures (nanotubes and NWs) serve as illuminative examples of where improvements may be made. One common method used to measure NW thermal properties is the “3ω” technique, in which a sinusoidally varying current in the sample at frequency ω produces Joule heating at a frequency of 2ω. A 3ω component of the arising voltage measured by a lock-in amplifier is inversely proportional to the thermal conductance of the sample [48]. If electrical contact resistances are known, and input current can be minimized to render temperature rises at the contacts negligible the method can be quite precise [49]. Another technique that has experienced increasing application in recent years due to its simplicity is the use of microfabricated heater/thermometers, an example of which is shown in Fig. 1.2. In this case, the axial nanostructure is suspended across microheaters (usually made of Pt) with well-calibrated temperature-resistance behavior. The temperature is set on one side and the measured temperature difference across

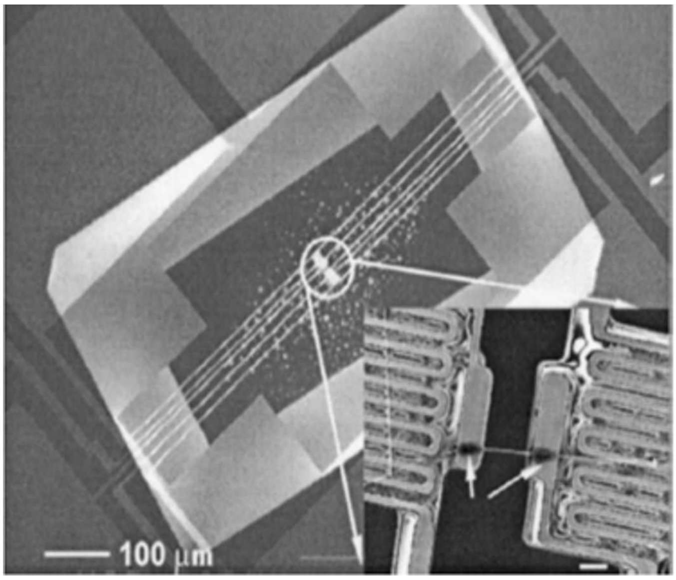

Figure 1.2: SEM image of a suspended Pt microthermometer device. Inset: SEM image of a single bridging Si NW bonded with amorphous carbon deposits that marked by arrows (scale bar = 2 μm). Reprinted with permission from D. Li, Y.Y. Wu, P. Kim, L. Shi, P.D. Yang, and A. Majumdar. Thermal conductivity of individual silicon nanowires. *Appl. Phys. Lett.*, 83(14):2934-2936, 2003. Copyright 2003, American Institute of Physics.

the nanostructure provides its thermal conductance [50]. Both techniques require carefully microfabricated devices, and the NW must be suspended across the device – a process that is often slow, tedious and destructive. Interfacial contact resistances can also result in a potentially significant source of error for these methods, especially for large diameter NWs [50]. As a result, there is scarce data available for many different NWs. To increase the speed and ease of measuring thermal conductivity, and to provide rapid metrology tools for as-fabricated NW-based devices, new characterization methods that are simple, rapid, non-destructive (and possibly non-contact) are highly desirable. These same characteristics are ideal for dealing with a variety of NW properties beyond thermal conductivity.

1.5 Basic Theory of Raman Spectroscopy

This section is reproduced in part with permission from the book chapter "Raman Spectroscopy for Characterization of Semiconducting Nanowires" authored by Gregory S. Doerk, Carlo Carraro, and Roya Maboudian, which will be published as part of the book "Raman Spectroscopy for Nanomaterials Characterization" edited by Challa S.S.R. Kumar.

Optical characterization typically fulfills the desired features of techniques catalogued in the previous section, and in particular Raman spectroscopy is attractive for its submicron resolution and minimal need for sample preparation. As a probe of lattice vibrations, Raman spectroscopy is very sensitive to intrinsic crystal properties and extrinsic stimuli in non-metals. It may be employed to study crystal structure and quality, crystal orientation, optical interactions, chemical composition, phases, dopant concentration, surface and interface chemistry, and local temperature or strain. These features have made it a vital tool for research labs studying semiconductor-based technologies. They also are increasingly important for the study of semiconductor NWs fabricated by both top down and bottom up approaches since many of the common characterization methods used with bulk crystals or thin films cannot be applied to NWs in a direct manner.

In Raman scattering a photon is inelastically scattered by a crystal excitation such that the scattered photon possesses a different energy from the incident photon. Under the semiclassical theory of Raman scattering, the inelastically scattered light is produced by a modulation of the dielectric polarization through an excitation of the crystal with a finite momentum and energy. Raman scattering is witnessed only with the existence of a non-zero derivative of the dielectric susceptibility tensor with respect to the excitation amplitude, which for normal (vibrational) Raman scattering in crystals is provided by the creation (Stokes process) or annihilation (anti-Stokes process) of phonons. In Raman scattering from crystals both energy and momentum must be conserved. For first order Raman scattering this means

$$\omega_s = \omega_i \pm \omega_j \tag{1.9a}$$

$$\boldsymbol{k_s} = \boldsymbol{k_i} \pm \boldsymbol{q_j} \tag{1.9b}$$

where ω refers to angular frequency, $\boldsymbol{k}$ refers to a wave vector $(2\pi/\lambda)$ of light, $\boldsymbol{q}$ is the phonon wave vector, and λ is the wavelength of light. The subscripts i, s and j refer to the incident light, scattered light, and the phonon mode, and the (+) or (-) sign refer to an anti-Stokes or Stokes process (for frequency) respectively. Since the maximum phonon wave vector is achieved in the limit where the scattered wave vector is equal in magnitude and opposite in direction (perfect backscatter) of the incident wave vector, q must be less than $4\pi/\lambda_i$. The Brillouin zone on the other hand is at its maximum value for π/d, where d is the appropriate lattice constant. For visible light ($\lambda >\sim$300 nm) the maximum phonon wave vector is limited to values of approximately 10^{-3} relative to the extent of the first Brillioun zone, or essentially zero for the sake of most calculations, giving rise to what is often referred to as a "selection rule" (not to be confused with polarization selection rules) for first order Raman scattering:

$$q_j \approx 0 \tag{1.10}$$

Given their position at the center of the Brillioun zone and their non-zero frequency at zero (or near zero) momentum, the mode for these phonons is commonly referred to as the zone center optical mode. A sample Stokes spectrum for a single Si NW in the range of -50-570 cm^{-1} highlighting the first order optical phonon peak is given in Fig. 1.3

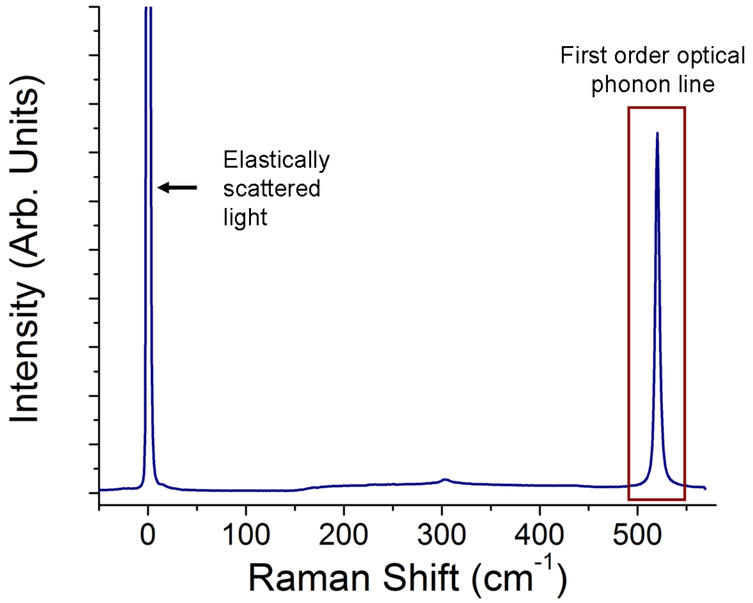

Figure 1.3: Raman spectrum from an individual VLS-grown single crystal Si NW with a diameter >∼150 nm.

For stokes processes involving phonons the intensity I of scattered light is given by [51]:

$$I_s \propto \lambda_s^{-4} |\hat{e}_i \cdot \boldsymbol{\chi_j} \cdot \hat{e}_s|^2 \, (n_j + 1) \, I_i \tag{1.11}$$

The $\hat{e}$ term refers to a unit polarization vector, $\boldsymbol{\chi}$ is the first order derivative of the susceptibility tensor with respect to the phonon amplitude, also known as the Raman tensor, and n_j is the phonon occupation number for the jth mode, given by:

$$n_j = [exp\,(\hbar\omega_j/kT) - 1]^{-1} \tag{1.12}$$

where $\hbar$ is Planck's constant, k is Boltzmann's constant, and T is absolute temperature. The proportionality is essentially the same for anti-Stokes processes except that n_j+1 is replaced by n_j. The terms except I_i are part of the Raman scattering cross section $\sigma_R(\omega, \omega_j)$.

At this point we may take note of the salient features of this relation and their implications for Raman scattering experiments. First, since the frequency of the scattered light is shifted from the incident light frequency by a much smaller phonon frequency, the incident and scattered light frequency are approximately the same value. Their wavelengths are then also approximately the same, and the Raman scattering intensity may be treated as possessing a similar fourth power dependency on the incident light wavelength, which is a characteristic feature for scattering cross sections at frequencies below the main absorption band of the scattering material [51]. The second term involving the Raman tensor reflects the symmetry of the scattering medium. For crystals this is of particular importance as the cross section may be required to disappear for certain polarization unit vector combinations. Careful analysis of intensities for various phonon lines in the Raman spectra may provide valuable information about the crystal symmetry (and hence structure). The phonon occupation number terms introduce an explicit dependence of the scattered intensity on sample temperature. Though the presence of other components to the scattered intensity in equation, (1.11) as well as factors involving the experimental apparatus, will make a firm quantitative link between temperature and intensity precarious, the ratio between Stokes and anti-Stokes intensities is far less ambiguous. We will return to the possibility of measuring local temperature from Raman spectra later.

1.6 Outline of This Work

This dissertation describes a series of investigations centered around a theme of bottom up synthesized Si NWs. Chapter 2 details the chemical processes and experimental methods involved in the synthesis of Si NWs by Au-catalyzed and Pt-catalyzed VLS growth and electroless Ag-assisted etching, as well as the synthesis of branched Si nanowires by VLS growth with branches seeded by Au migration of the primary NW catalyst. Chapter 3 describes strategies developed for the integration of epitaxially grown Si NWs into possible devices. Special attention is paid to epitaxially bridging Si NWs, controlled templating of the catalyst nanoparticles for NW growth using block copolymer micelles, and *ex situ* boron doping of Si NWs. Chapter 4 elucidates efforts toward developing rapid, non-destructive methods to measure the thermal conductivity of single NWs using Raman spectroscopy. Raman spectroscopy of crystalline NWs is briefly introduced, followed by an outline of precise measurements of the thermal dependence of the first order optical phonon peak for individual Si NWs and the description of an experimental technique to measure the thermal conductivity of individual cantilevered NWs using Raman thermal mapping. Finally, this dissertation concludes with suggested directions for future investigations based on the the more promising results presented herein.

Chapter 2

Synthesis of Silicon Nanowires and Nanotrees

An essential requirement for studying nanowires is a firm understanding about how to fabricate or synthesize them. Therefore, this chapter discusses critical features about the synthesis of silicon NWs and nanotrees *via* the vapor-liquid-solid (VLS) process, as well as basic elements of producing Si NWs through the electrochemical etching of Si by the galvanic displacement of Ag.

2.1 Vapor-Liquid-Solid Silicon Nanowire Synthesis

Though filamentary semiconductor materials had been synthesized for at least several years beforehand, the VLS mechanism for nanowire growth was first hypothesized by Wagner and Ellis in 1964 [52] to explain the growth of Si wires by chemical vapor deposition (CVD) in the presence of Au impurities. Since then, the VLS mechanism has been used to explain wire growth for a wide variety of materials using an ever growing array of impurity materials, or “catalysts” [53]. While some fundamental aspects of VLS growth are still not completely understood, its utility is undeniable given the very high crystal quality of the wires, the range of synthetically accessible materials, the capability for diameter control from mm-scale to sub-10 nm scale [54], and the potential for unique and technologically useful heterostructures. The simplified synthesis of nm-scale ($<$ 10 nm - $<$ 1000 nm diameters) wires and related heterostructures has led to the resurgent interest in VLS growth in the past decade, and it is this size scale to which this chapter will be devoted.

2.1.1 Vapor-Liquid-Solid Growth

VLS growth of Si NWs using Au catalyst has been employed successfully by many different research groups and is one of the simplest VLS systems to understand. A schematic of the basic mechanism addressing epitaxial Si NW growth from crystalline Si substrates is accompanied by the Au-Si binary temperature-phase diagram in Fig. 2.1. One starts with a Au catalyst nanoparticle (NP) on the Si surface (1). The sample is heated until at the eutectic temperature the Au NP rapidly alloys with the underlying substrate and generates a liquid Au-Si alloy droplet (2). If a Au thin film was deposited on the surface instead of a NP, at this stage the liquid Au-Si alloy dewets, forming a dense, polydisperse array of Au-Si droplets [55]. The sample may then be heated further to the desired temperature for physical vapor deposition (PVD) or CVD. Since the alloy is in contact with a much larger Si reservoir, the equilibrium droplet composition follows the Si liquidus line. The choice for final growth temperature depends on the growth process or chemistry. At this temperature a physical or chemical vapor phase precursor is introduced into the reactor. The much higher sticking coefficient of the liquid droplet in contrast to the surrounding solid Si results in significantly enhanced adsorption of the Si precursor onto the droplet surface. After surface reaction (if necessary) the adsorbed Si is absorbed into the droplet. Since the droplet is already at its equilibrium Si fraction on the Si surface, this excess absorbed Si supersaturates the droplet. Eventually, crystalline Si precipitates, nucleating the growth of the NW (3). When the rate of Si addition from the vapor phase matches the rate of crystal precipitation, steady state growth is achieved (4) and may be continued for as long as the flow of Si precursor is maintained.

When in contact with a crystalline Si surface, the NW may be grown epitaxially; that is the orientation of the crystal is dictated by the orientation of the underlying (crystalline) substrate. However, the NW growth direction is determined by total energy minimization. For larger diameter wires, the crystal surface that minimizes the energy at the NW/catalyst interface controls the growth orientation, but as the NW diameter decreases the overall surface to volume ratio increases and the size of the catalyst/NW interface decreases. Thus, below a critical diameter surface energy minimization for the NW results in a change in the NW growth orientation [56] (though the catalyst/NW interface may retain the same interface as for larger diameter NWs [54]). For the Au-Si VLS system, the dominant growth direction for NWs larger than 20-30 nm in diameter is <111>; at or below this diameter Si NWs grow in the <110> direction, or occasionally the <112> growth direction [54, 56]. In this dissertation, all Si NWs grown from Au catalyst are above ∼20 nm and grow in <111> directions, so these epitaxial Si NWs may be grown perpendicularly to Si(111) surfaces.

The kinetic processes involved in VLS growth may be summarized in four steps:

1. Gas phase transport of Si to the liquid surface.
2. Adsorption, surface reaction, and absorption into the droplet.
3. Diffusion through or around the liquid droplet.
4. Incorporation into the Si lattice

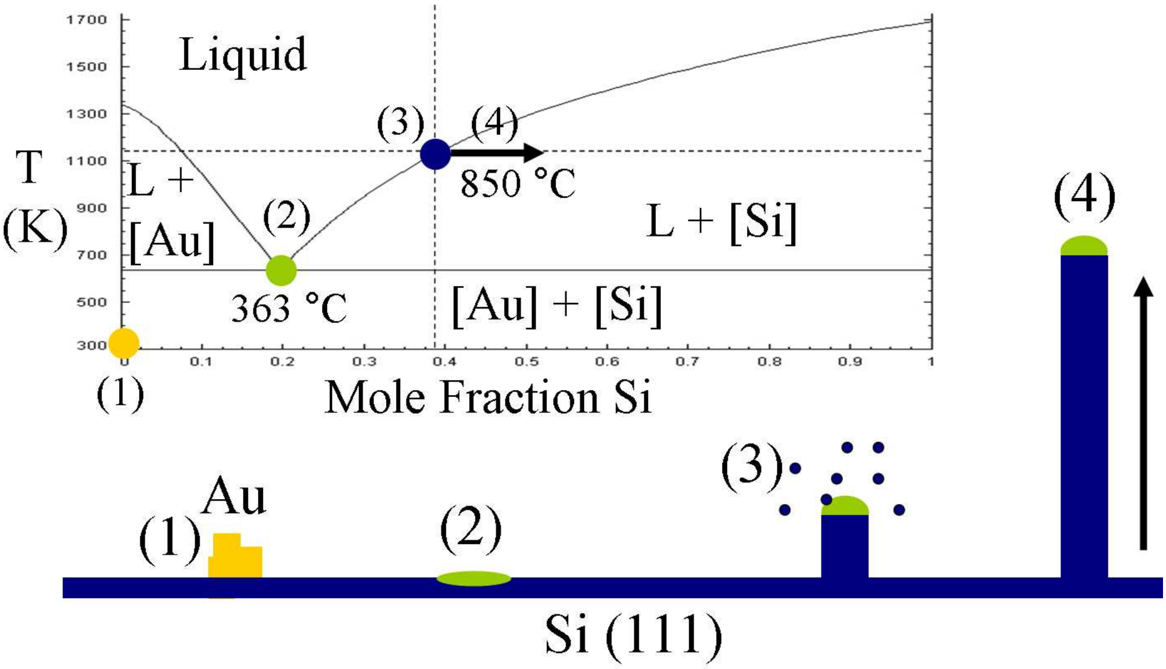

Figure 2.1: Schematic of the VLS growth process for epitaxial Si NWs using Au catalyst. The inset is the binary temperature-phase diagram for the Au-Si system. The steps in the VLS process are: (1) Initial placement of Au on the Si surface, (2) Au alloying with the substate at and above the eutectic temperature, (3) nucleation of NW growth upon introduction of Si vapor phase precursor into the reactor, and (4) steady-state NW growth.

Any step may be rate determining, though the complexities of VLS growth kinetics recommend the rejection general NW growth kinetic models that rely on a single rate determining step [57]. The term "catalyst" used to refer to the seed particle or material for NW growth may also seem imprecise or even incorrect since chemical reaction is not a necessary component to VLS growth. However, the path-independence of the chemical potential difference between the vapor phase precursor and the as-deposited crystal means that the alloy droplet must provide a path that acts to kinetically enhance the crystal growth process locally, and so may be considered a catalyst for crystal growth.

As the vapor phase silicon precursor, silicon tetrachloride ($SiCl_4$) was used, which can deposit Si by hydrogen reduction according to the following reaction:

$$SiCl_4(g) + H_2(g) \rightleftharpoons Si(s) + HCl(g) \tag{2.1}$$

A schematic of the reactor setup is given in Fig. 2.2. Samples are placed on a larger Si shard in the center of a 1 inch diameter quartz tube inside a tube furnace. The reaction proceeds at atmospheric pressure and reaction temperatures typically exceed 800 °C. In principle VLS growth may take place at any temperature above the Au-Si eutectic (363 °C), but the greater stability of $SiCl_4$ over silane demands much higher growth temperatures. Its use is motivated primarily by the simplicity of the reactor system and by the facts that $SiCl_4$ is both much safer and less expensive than silane. It also routinely achieves high quality Si homoepitaxy, which has been attributed to the capability of the HCl product to etch SiO_2 [38], though this explanation has not been confirmed. HCl is known to etch Si at high temperatures, and this chemistry has been shown to transition from Si deposition to Si etching depending on the ratio of Si to H_2 [58, 59, 60]. Thus, it is important to be able to control both the concentration and flow of $SiCl_4$ into the reactor. To do this, the carrier gas (10% H_2 in Ar) flows through two lines. One goes directly to the reactor while the other passes through a bubbler containing liquid $SiCl_4$ at 0 °C so that its vapor pressure may be estimated precisely. The flow rates through each line are controlled by separate mass flow controllers. Ar is used as a purge gas when the reactor is not being used for reactions.

2.1.2 Galvanic Displacement for Catalyst Deposition

As noted previously, Si NWs may be grown from individual Au nanoparticles or Au thin films that form an array of droplets with a large diameter distribution upon dewetting above the Au-Si eutectic temperature. These thin films may be deposited by a number of methods, and PVD techniques like evaporation or sputtering are commonly used. In this dissertation, the method used to deposit Au thin films is based upon a class of electroless metal deposition reactions called galvanic displacement. In galvanic displacement, metal ions dissolved in (usually aqueous) solutions are spontaneously reduced to elemental form by electrons provided through oxidation of the underlying substrate. Typically metals with redox potentials above hydrogen may be deposited, while substrates must be able to oxidize

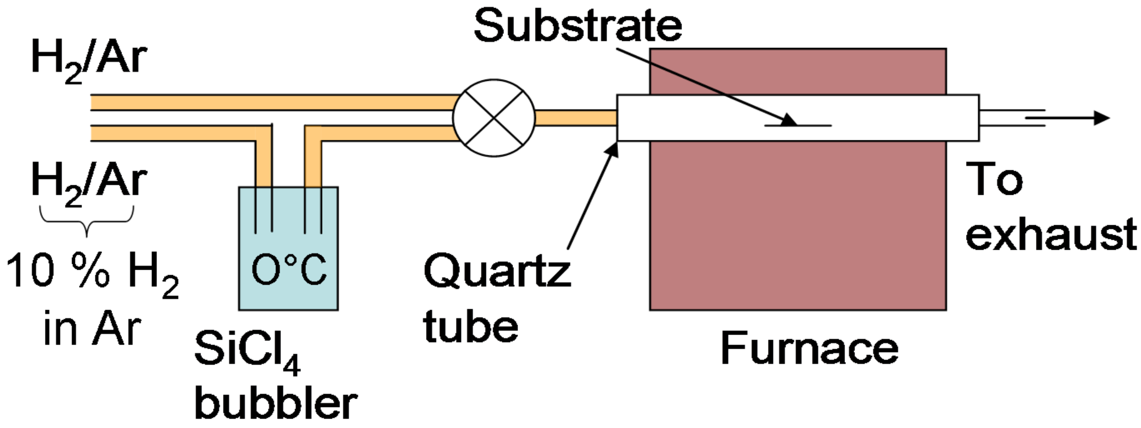

Figure 2.2: Schematic of the reactor setup for VLS Si NW growth.

readily; these criteria still leave available a wide variety of important metals and semiconductor substrates [61]. The requirement for substrate oxidation makes the deposition inherently selective, permitting the use of common masking materials such as SiO_2, SiN_x, or some polymers. Furthermore, deposition is conformal and thickness may be controlled by immersion time and metal ion concentration. No seed layers are necessary, though in most cases an additional solute like hydrofluoric acid (HF) must be added to remove the oxidized substrate as it develops. Since Au has a very high redox potential and silicon oxidizes readily, displacement of Au onto Si is quite easy. In this dissertation, the plating solution for Au galvanic displacement consists of 0.1-10 mM potassium tetrachloroaurate ($KAuCl_4$) in deionized (DI) water, with HF added in concentrations 20 - 300 times in excess of the Au salt concentration. Prior to Au deposition, samples were cleaned by sequential sonication in acetone, isopropyl alcohol (IPA), and DI water for 5-10 min. each, followed by treatment with a UV ozone cleaner for 5-10 min. (Jelight UVO-Cleaner Model No. 42) and removal of the native oxide by immersion in 48-50% HF for 1 min.

Figure 2.3 is a scanning electron microscope (SEM) image of Si NWs grown on Si(111) from an approximately ∼2 nm Au film (1 mM, 10 min.; thickness estimate based on a previous Au deposition rate measurement [62]). The growth temperature was 850 °C and 50 sccm of carrier gas passed through the bubbler, while 200 sccm went directly to the reactor. Many of the Si NWs grew vertically from the substrate, indicative of epitaxial growth. The inset images show high resolution transmission electron microscope (HRTEM) images of a representative Si NW at different magnifications from this sample. Si NWs grown in the <111> direction from Au catalyst nanoparticles are known to exhibit a hexagonal cross section with {112} sidewalls [52, 37]. These images are taken from a <110> direction orthogonal to the wire axis and therefore the NWs are viewed edge-on. By inspection, the

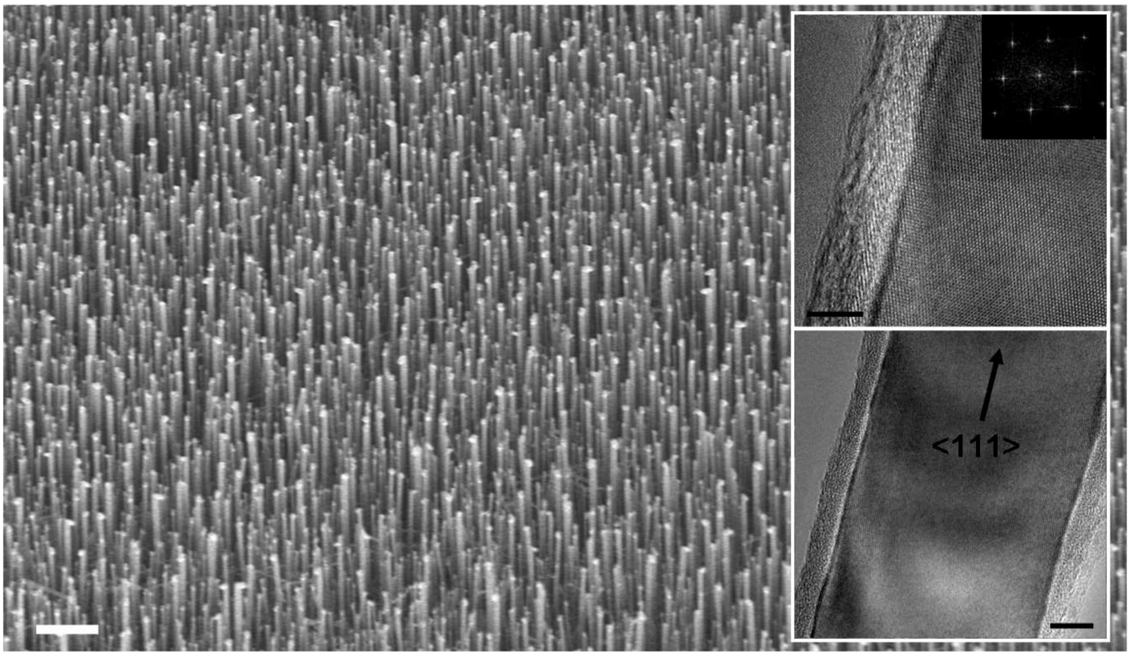

Figure 2.3: SEM image of Si NWs grown from a ∼2 nm Au film (scale bar = 2 μm). Insets: TEM images of a single Si NW from the same sample at two different magnifications. The fourier transform of the lattice image in the upper inset indicates that the wire in a single-crystal. Indexing would indicate that it also is aligned along a <111> direction. The inset scale bars are 5 nm (upper) and 10 nm (lower).

NW sidewalls are very smooth and the edge-profile sidewall roughnesses are typically less than 0.3 nm. The Fourier transform of the lattice image (upper inset) indicates that the NW is indeed single-crystal and grows in a <111> direction.

One peculiar but commonly observed aspect of Si NW growth using $SiCl_4$ is a strong dependence on the growth rate on NW diameter (or droplet diameter, as they are proportional). This is clear in SEM images of Si NWs grown from a galvanically displaced Au film at 850 °C (Fig. 2.4(a) and (b)). For ease of viewing this phenomenon the images are taken from a region of the sample that exhibited lower density growth, but the diameter dependence is apparent in all Si NWs grown from $SiCl_4$ using Au regardless of their areal densities. The most commonly accepted explanation, first posited by Givargizov [63] invokes the Gibbs-Thomson effect in which the Si vapor pressure around the liquid eutectic droplet increases, and hence the supersaturation of the droplet decreases, with decreasing diameter. Since the growth rate may be considered proportional to the droplet supersaturation according to the VLS model, smaller diameter NWs should grow more slowly than larger diameter NWs [63]. A mathematical description of this phenomenon depends on the

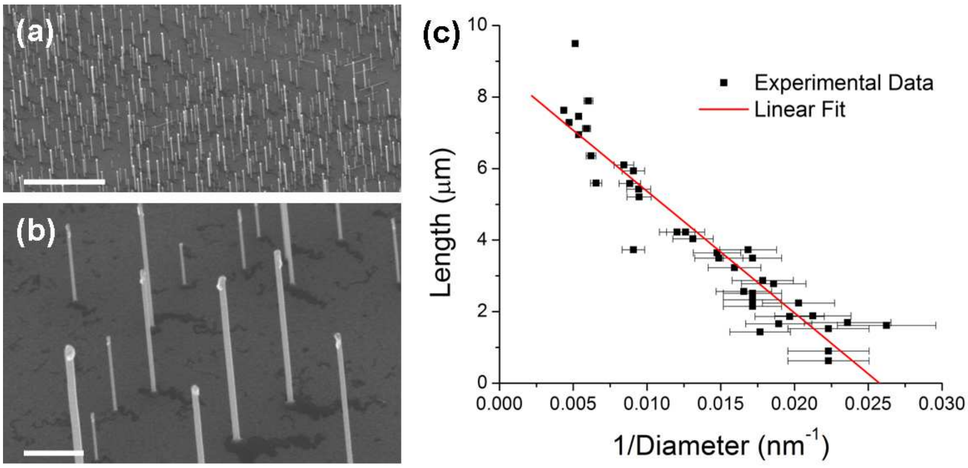

Figure 2.4: Diameter dependence of VLS Si NW growth using $SiCl_4$. (a) SEM image of Si NWs grown from galvanically displaced Au nanoparticles, or a very thin film, with low areal density (scale bar = 10 μm). (b) Higher magnification SEM image from the same region showing more closely the scaling of length with NW diameter (scale bar = 1 μm). (c) Measured NW lengths *vs.* the reciprocal of their diameters in line with the model proposed in [63]. The red line is a linear fit to the data.

particular definition for supersaturation that is used. Givargizov chose to describe it as the difference in the chemical potential of the droplet from the equilibrium chemical potential ($\Delta\mu$), normalized by the system thermal energy, kT. Including the Gibbs-Thomson effect adds a term accounting for the energy linked to droplet curvature such that

$$\frac{\Delta\mu}{kT} = \frac{\Delta\mu_o}{kT} - \frac{4\Omega\sigma}{kTD} \tag{2.2}$$

where $\Delta\mu_o$ is the supersaturation for an infinite flat surface, Ω is the atomic volume of Si, σ is the Au-Si liquid surface energy, and D is the NW diameter. Direct proportionality implies a negative linear dependence on $1/D$, which is fit reasonably well by linear regression, as seen in Fig. 2.4(c). The coefficient of determination (R^2) is above 0.88.

The fit implies a minimum diameter that may be grown of approximately $\sim$40 nm. However, in the same reactor and with nearly the same conditions, Si NWs with diameters as small as $\sim$10 nm have been grown from galvanically displaced Au on different samples. This suggests that there is no strict minimum diameter that is possible with VLS growth (using $SiCl_4$ or other Si precursors). It also implies that a linear model cannot cover the whole diameter range appropriately. A more nuanced model may be developed by assuming the NW growth rate is proportional to the supersaturation defined instead as the difference between the chemical activity of Si in the droplet to the equilibrium chemical activity. This may be controlled by the net flux of Si precursor to the droplet, proportional in turn to the difference between the Si precursor pressure and the equilibrium Si vapor pressure above the droplet, $P_{eq,D}$. This equilibrium vapor pressure is increased by the Gibbs-Thomson effect arising from surface curvature according to the following relationship [64]:

$$P_{eq,D} = P_{eq,o}\text{exp}\left(\frac{4\Omega\sigma}{kTD}\right) \tag{2.3}$$

where $P_{eq,o}$ is the equilibrium vapor pressure over the infinite liquid surface. Under this treatment, the diameter dependence derived from the Gibbs-Thomson effect exists in an exponential term. However, if the exponential is linearized (by Maclaurin expansion including only linear terms; i.e. $e^x \approx 1 + x$) then an expression completely analogous to the previous derivation of Givargizov is obtained. At present, a set of samples covering the range of NW diameters from $\sim$10 to $>>$100s of nanometers has not been obtained to best test this hypothesis.

It is important to note that a strongly diameter dependent growth rate is not typically observed in NW growth using other common Si chemical precursors like silane or disilane. Indeed, *in situ* TEM observation during Si NW growth by Kodambaka *et al* confirmed a diameter independence when using disilane [65]. They posited that diameter dependent growth by Gibbs-Thomson effects is only possible when the growth is near equilibrium (small supersaturations), or some process can drive desorption. In chlorosilane systems, desorption may be driven by competitive Si removal as discussed in the next section.

2.1.3 Silicon Nanowire Growth from Au colloids

The use of a Au film as catalyst results in high density growth of Si NWs with a wide diameter range but otherwise ideal characteristics such as excellent crystal quality, very smooth surfaces, and minimal taper from the NW base to tip. Using Au nanoparticles (NPs) permits control over the diameter of Si NWs grown from them, but the product tends to be far more sensitive to synthesis conditions than in the case of growth from thin films. In this section, results of growth studies from Au colloidal NPs are presented.

Collidal Au NPs with predetermined mean diameters were purchased from Ted Pella Inc. The as-received Au colloids are stabilized by citrate molecules that with a net negative surface charge [66]. Since SiO_2 has a negative surface charge, and Si has a negative surface charge for a pH $\geq$ 2 [67], the repulsive interaction with the colloids makes it difficult to deposit them onto Si surfaces. This hurdle to Au colloid deposition was overcome by two different ways. In the first, a thin layer of poly-L-lysine that presents a positive charge was applied to the Si (or SiO_2) surfaces by immersing cleaned samples in a 0.1 wt.% poly-L-lysine solution purchased from Ted Pella Inc. for 1 min. After rinsing with DI water and dying under a N_2 stream, the samples were immersed in colloidal suspensions diluted with DI water for variable times.

The second method follows the work of Woodruff *et al* [68]. HF (48-50 % w/w) is added to Au colloidal suspensions diluted with with DI water in a volume ratio of 0.004-0.025 to

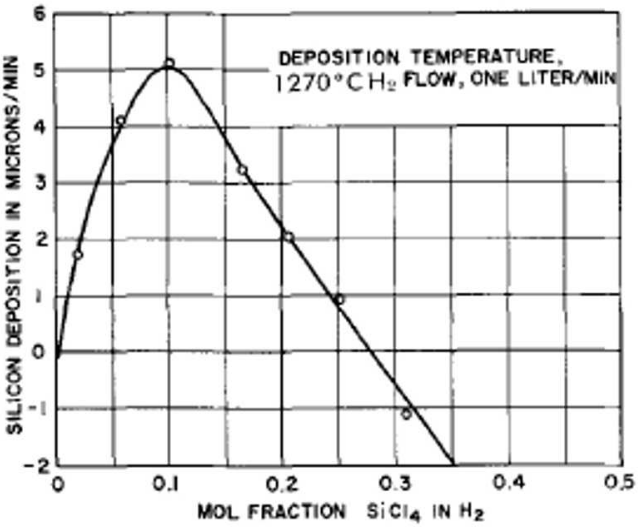

Figure 2.5: Si film deposition using $SiCl_4$ precursor as a function of the $SiCl_4/H_2$ ratio at 1270 °C. Reprinted with permission from J. Electrochem. Soc., 108, 649-653 (1961). Copyright 1961, The Electrochemical Society. [58].

1 (HF to diluted suspension) to achieve a pH < 2. Cleaned samples were immersed in this suspension for variable lengths of time, followed by rinsing with DI water and drying under a N_2 stream. Besides making the Si surface charge neutral, the acid is believed to destabilize the citrate molecular coating on the Au colloids [68]. This method also has the advantage of removing some native oxide and providing some selectivity for Au colloid deposition on Si over SiO_2. However, the selectivity is not perfect, and in both methods Au colloid deposition is positionally random.

The second method was used primarily to study the growth of NWs from Au colloids at low density (< 0.1 μm^{-2}). To avoid any diameter dependent effects on NW growth rates, 50 nm Au colloids were used. As noted before, there is an equilibrium between Si etching and deposition for our growth chemistry that complicates the dependence of growth rate on $SiCl_4$ concentration. However, assuming the VLS catalyst does not substantially alter the reaction chemistry then kinetic behavior analogous to what has been seen previously in the epitaxial deposition of Si using $SiCl_4$ may be expected. Figure 2.5 is an example of the concentration-dependent deposition/etching behavior observed in Si epitaxy using $SiCl_4$ at a temperature of 1270 °C [58]. A maximum deposition rate is observed at a molar ratio of $SiCl_4$ to H_2 of ∼0.1. Above this ratio the deposition rate decreases with an increasing ratio in a linear fashion, and above a ratio of ∼0.27 Si etching occurs. At lower temperatures, the particular shape of the curve will change but the behavior is qualitatively similar.

Figure 2.6(a) shows the growth rate of Si NWs at 810 and 850 °C as a function of the relative ratio of the volumetric bubbler flow rate to the direct flow rate. The bubbler flow rate was set at a constant rate of 50 sccm, and the direct flow rate was adjusted to achieve the correct ratio. Total growth time was 10 min. for each data point. Assuming gas phase ideality, the molar ratio of $SiCl_4$ to H_2 (X_{SiCl_4}) may be estimated in relation to the bubbler/direct lines volumetric flow ratio (R_v) by

$$X_{SiCl_4} = \frac{P_{SiCl_4}}{0.1\left(P_o - P_{SiCl_4}\right)} \frac{R_v}{R_v + 1} \tag{2.4}$$

where P_{SiCl_4} is the vapor pressure of silicon tetrachloride in the bubbler and P_o is the background pressure (atmospheric). In the range of flow rates studied here R_v is always less than 1. In Fig. 2.6(a), the growth rate decreases with increasing R_v, indicating we are past the maximum growth rate. Other than growth rate, the tapering of VLS-grown Si NWs is very important as well-regulated and uniform dimensions are necessary for their eventual device integration. We define taper as the ratio of the difference of the NW diameter at the base (D_{base}) to the tip (D_{tip}) to its length (L), or

$$Taper = \frac{D_{base} - D_{tip}}{L}. \tag{2.5}$$

Taper as a function of R_v for the same temperatures is given in Fig. 2.6(b). For both temperatures a minimum taper value occurs near a R_v value of ∼0.35-0.40. If one assumes that taper is proportional to the ratio of sidewall deposition, also known as “vapor-solid” or VS growth, to VLS growth, this indicates that the VLS growth and VS growth do not have the same dependency on X_{SiCl_4}. A SEM image of a highly tapered Si NW is given in Fig. 2.6(c)

It is also notable that for all values of R_v the growth rate is lower and the taper is higher at 850 °C than at 810 °C. Indeed, strong growth rate and taper dependencies on temperature are apparent at a fixed value of R_v. Figure 2.6(d) shows an SEM image of a much less tapered wire grown at 800 °C with a R_v value of ∼0.37 and Fig. 2.6(e) depicts the average growth rate and taper values *versus* temperature for a R_v value of ∼0.37. The inverse relation between taper and growth rate is expected under the assumption given above that tapering is proportional to the ratio of VS growth to VLS growth. On the other hand, the decrease in NW growth rate with increasing temperature is not a common feature in CVD systems, even under mass transport control. Since the $SiCl_4$ and H_2 concentrations are constant, this behavior suggests a negative apparent activation energy.

This may be the consequence of shifting equilibrium with temperature. Another possibility is that the NW growth is strongly affected by adsorption, desorption, and reaction kinetics on the droplet surface. Earlier in this chapter it was argued that Si NW growth rate may be proportional to silicon supersaturation in the form of pressure above the droplet, but the proportionality was not made explicit. A simple way to incorporate adsorption kinetics is to include a reactive sticking coefficient, S such that the VLS growth rate (R_{VLS}) obeys

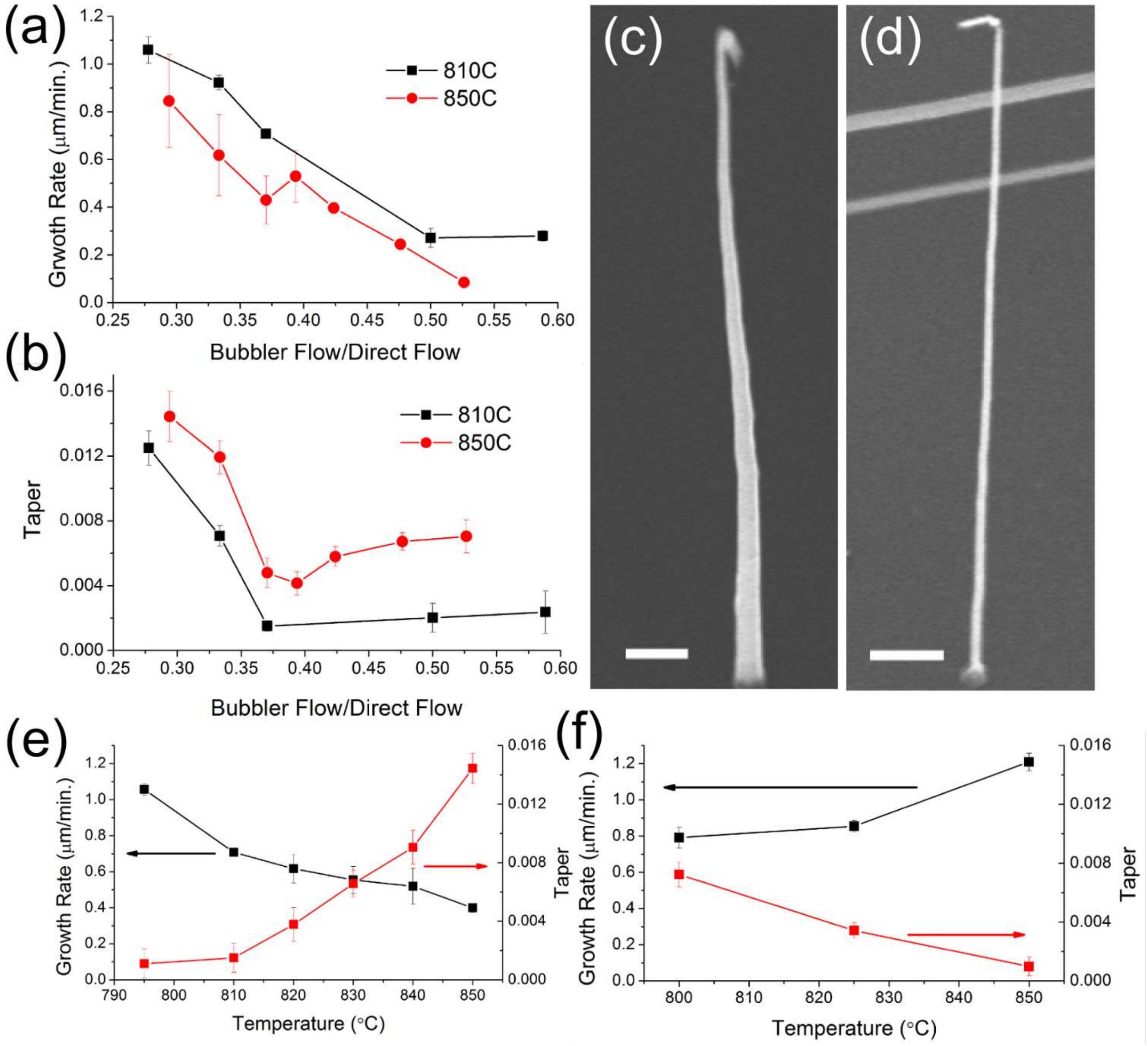

Figure 2.6: Growth Rate and Taper of VLS-grown Si NWs using 50 nm Au colloids. (a) Growth rate *versus* the ratio of bubbler to direct flow at 810 and 850 °C. (b) Taper *versus* the ratio of bubbler to direct flow at 810 and 850 °C. (c) SEM image of a Si NW grown at 850 °C at a flow ratio of ∼0.28 (scale bar = 500 nm). (d) SEM image of Si NW grown at 800 °C at a flow ratio of ∼0.37 (scale bar = 500 nm). (e) Growth rate and taper versus temperature at a flow ratio of ∼0.37. (f) Growth rate and taper versus temperature at a flow ratio of ∼0.37 for NWs at a higher density (wire density = $0.4 \pm 0.3\ \mu\text{m}^{-2}$).

the following proportionality:

$$R_{VLS} \propto S\left(P_{Si} - P_{eq,D}\right) \tag{2.6}$$

where P_{Si} is the gas phase equilibrium Si vapor pressure (in the form of various chlorosilanes) away from the droplet. S may be considered a composite of the adsorption, desorption, and surface reaction rate constants (k_a, k_d and k_r respectively). In cases where each process is activated and the rate of forward surface reaction is comparable to or lower than the rate of precursor desorption, a condition that may be possible with large Si removal rates, then the apparent activation energy (E_{app}) may be approximately described by

$$E_{app} \approx E_a + E_r - E_d \tag{2.7}$$

where E_a, E_r and E_d are the activation energies for adsorption, surface reaction and desorption respectively. If $E_d > E_a + E_r$ then $E_{app} < 0$. A decrease in the reactive sticking coefficient with increasing temperature has been witnessed before in Si CVD chemistry, such as in the adsorption kinetics of disilane and trisilane [69] as well as dichlorosilane [70]. However, systematic calculations and experiments are necessary to discern the likelihood of one hypothesis over the other, or other explanations not presented here.

Whether or not adsorption kinetics result in the negative apparent activation energy for Si NW growth observed in this system, its general importance in the VLS process may help explain other interesting phenomena in NW growth. One instance is the case of different kinetic behavior in the growth of Si NWs from $SiCl_4$ at higher NW densities. Figure 2.6(f) shows NW growth rate and taper *vs.* temperature at $R_v = \sim 0.37$ at a "high density" (0.4 ± 0.3 μm^{-2}, Au colloids deposited by the first method). The growth rates appear to increase while the taper values decrease with increasing temperature, in contrast to what was witnessed for lower density growth. Under lower density growth, the Si precursor that desorbs from the droplet before it contributes to VLS growth may redeposit on NW sidewalls by VS growth, leading to enhanced taper. However, as NWs are grown closer to each other, the Si precursor desorbed from the droplet on top of one NW is more likely to readsorb onto another NW droplet, a phenomenon that has been termed "synergetic" NW growth [71]. This makes the NW growth less sensitive to temperature and may account for the observed reduction in taper at higher temperatures. However, it fails to explain the higher taper compared to the lower density case at a lower temperature, which is most likely due to the fact that high density and low density growth experiments were conducted over a year apart from each other, reflecting the changes that occur in reactor growth conditions over time.

This underscores the great care that must be taken when conducting kinetic studies on the growth of SiNWs using chlorosilane chemistry for several reasons. First, the atmospheric pressure of the reactor can make mass transport effects more predominant. Second, hot wall reactors such as the one employed here exhibit very noticeable history effects due to factors such as the $SiCl_4$ liquid level in the bubbler, Si deposition on the quartz tube sidewalls, or the emergence of minor air leaks in o-rings or even metal tubing over time due to the caustic nature of the HCl byproduct. Finally, the simultaneity of density dependent growth, diameter dependent growth, and deposition/etching equilibrium complicates assessments about each individual dependence.

Most recently, common NW growth conditions employ a flow rate of only 10 sccm through the bubbler that is matched with a direct flow rate of 100 sccm (same temperature range). At this substantially lower R_v value, high quality, low taper NW growth from non-film Au catalyst is more commonly attained, and the total consumption of $SiCl_4$ is reduced, giving more time before the bubbler must be refilled. However, growth rate assessments cannot be made with the current amount of data available for growth at this concentration.

2.1.4 Pt-catalyzed Si Nanowire Growth

Thi section is reproduced in part with permission from: M. Cerruti, G. Doerk, G. Hernandez, C. Carraro, and R. Maboudian. Galvanic deposition of Pt clusters on silicon: Effect of HF Concentration and application as catalyst for silicon nanowire growth. *Langmuir*, 26(1):432-437, 2010. Copyright 2010 American Chemical Society.

While Au is typically used as the catalyst in VLS growth of Si NWs, Au incorporated into the Si lattice can introduce deep-level traps in the band gap that typically poison any optical or electronic devices [72, 73]. Pt on the other hand does not adversely affect silicon electronics as much as Au does [74]. In addition, Pt and PtSi are used as contacts for Si devices and are considered more CMOS compatible [75]. Pt is thus considered an attractive alternative catalyst to Au for Si nanowire growth. Despite the advantages of simplicity, conformality and substrate selectivity in galvanic displacement, there have been no previous studies of silicon nanowire growth from galvanically displaced Pt. Earlier reports have demonstrated Si NWs grown from evaporated Pt [76], PtSi [75], and chemically synthesized Pt colloids [77]. This section explores the effectiveness of Pt and PtSi films deposited by galvanic displacement at different [HF]/[Pt] ratios and for different times as catalysts for Si NW growth.

The Pt used for NW growth was deposited onto Si(100) (4-10 mm on a side, resistivity = 10-30 Ω-cm) using galvanic displacement. Platinum solutions were prepared by dissolving 5.7 mg of platinum(II) chloride (analytical grade $PtCl_2$,Aldrich) in 6.0 mL of water and 80 μL of ammonium hydroxide (reagent grade NH_4OH, Fischer) resulting in a 3.5 mM concentration of $PtCl_2$. The mixture is then sonicated for one to two hours and/or stirred with a stir bar overnight until a homogeneous solution is obtained. Next, the solution is transferred to a Teflon beaker, and 20 mL of water and varying amounts of HF were added, producing the desired ratio of HF to Pt precursor concentrations ([HF]/[Pt]). In the final solutions, the concentration of Pt was varied between ∼0.65 and 0.8 mM. The HF concentration was varied from 0.021 to 5.2 M, yielding [HF]/[Pt] ratios varying from 26 to 7917. Samples were immersed in this solution for a time duration ranging from 30 s to 1 h. The solution was not stirred during the deposition and the beaker was covered with parafilm. Following immersion, the Si samples were rinsed with DI water and dried under a N_2 stream. Si NW growth was carried out at 970 °C (near the bulk Pt-Si eutectic temperature [77]) under 6 sccm of bubbler flow and 270 sccm of direct flow for 10 minutes.

Dense Si NW arrays were obtained at any [HF]/[Pt] ratio including a ratio as low as 26, which was shown above to produce PtSi films rather than Pt clusters [78]. Since using low quantities of HF is desirable in many device-related applications where etching is a concern, attention has been focused on the growth obtained at low [HF]/[Pt] ratios. Parts (A) and (B) of Fig. 2.7 show SEM images of Si NW arrays grown on Si(100) from PtSi films formed after immersion in plating solutions containing [HF]/[Pt] = 26 for 5 min. The dense array of Si NWs grown from the PtSi film are typically composed of NWs with diameters larger than 100 nm. The inset in Fig. 2.7(A) is a close-up image of one NW with a catalyst particle at the tip consistent with the VLS growth mechanism.

Si NWs grew much farther apart from the PtSi formed after only 1 s of immersion in same plating solution, and generally possessed diameters of approximately ∼20-40 nm, as shown in Fig. 2.7(C). Although finer control of Si NWs diameter has been achieved using galvanically displaced Au from reverse microemulsions [79], such a low density of NWs grown from galvanically displaced catalyst has not been reported previously. The large diameter wires in Fig. 2.7 parts (A) and (B), are long compared to the smaller diameter wires in Fig. 2.7(C); this is indicative of diameter-dependent growth similar to that seen for Au catalyzed VLS Si NWs, described previously.

The NWs in Fig. 2.7(C) appear rotated approximately 45° from the larger NWs in Fig. 2.7(B). In both cases, the samples are oriented such that the {111} planes are aligned with the sides of the image. This way, the <111> directions outline a cross pattern in a plan view of a Si(100) substrate; <110> orientations are rotated 45° from <111> orientations proceeding from Si(100) plane, and thus outline a 'X' pattern as noted in Fig. 2.7(D). Therefore, we infer that the Si NWs grown in this study are epitaxial, but that the smaller diameter NWs (Fig. 2.7(c)) grow in predominantly <110> directions while the larger diameter NWs (Fig. 2.7(b)) grow along <111> directions. As noted earlier in this chapter, the growth direction of Si NWs grown by VLS from Au catalyst particles is known to crossover from <111> to <110> as NW diameter decreases down to approximately 20 nm due to the interplay between liquid-solid interfacial energy and silicon surface energies. It has been suggested that an equivalent crossover may exist for Pt catalyzed VLS-grown Si NWs [77], but that the critical diameter would be at least larger than 30 nm. On the basis of the growth directions and diameters observed in this study, we estimate that a crossover diameter for Pt likely occurs between 100 and 200 nm. These results demonstrate that galvanic displacement facilitates control of nanowire density, diameter, and orientation in the growth of epitaxial Pt-catalyzed Si nanowire arrays.

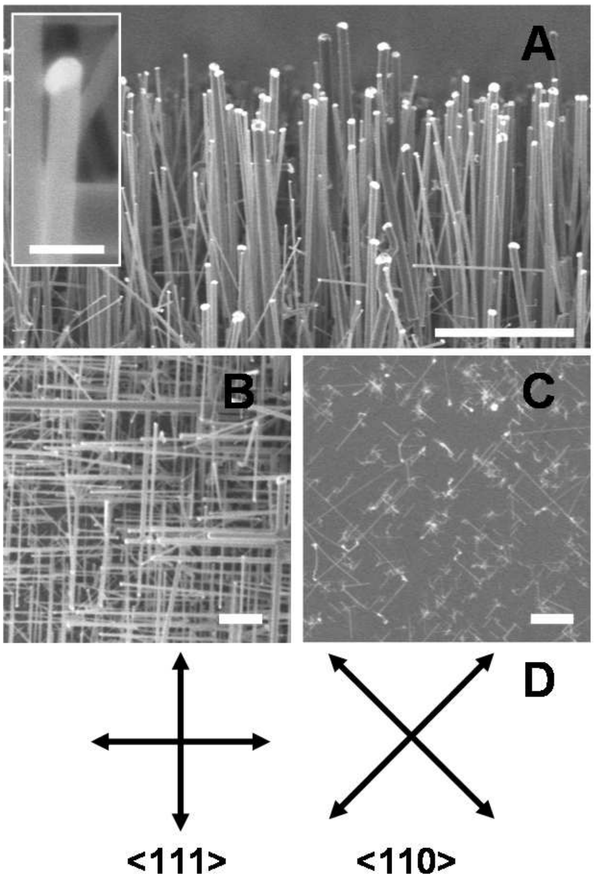

Figure 2.7: SEM images of Si NWs grown for 10 min at 970 °C from galvanically displaced PtSi, using [HF]/[Pt]=26 in the plating solution. (A) Wires grown off the substrate edge after 5 min. of immersion time (scale bar = 10 μm). Inset shows a close-up image of the catalyst at the NW tip (scale bar = 500 nm). (B-C) Plan view images of silicon nanowires grown after immersion in plating solution for (B) 5 min. and (C) 1s. Scale bars measure 2 μm on both images. (D) Schematic of the apparent directions of <111> and <110> oriented wires grown epitaxially on Si(100) from a plan view.

2.2 Branched Silicon Nanowire (Nanotree) Synthesis *via* Au Migration

This section is adapted from a publication that appeared in the *Journal of Materials Chemistry*: G.S. Doerk, N. Ferralis, C. Carraro, and R. Maboudian. Growth of branching Si nanowires seeded by Au-Si surface migration. *J. Mater. Chem.*, 18(44):5376-5381, 2008 - Reproduced by permission of the Royal Society of Chemistry

Nanowire architectures of increased complexity, such as branched NWs, are expected to result in new materials and devices with unique properties or enhanced functionality [80]. The synthesis of homo- and hetero-branched and multibranched NW structures [4, 80] by various methods has been demonstrated, introducing the possibility of fabricating hierarchical nanostructures of increased complexity and functionality. Recent progress has furthered these aims, demonstrating interconnected InAs NW networks [81], and the facile integration of GaAs NWs with Si NWs [82]. Many branching NW heterostructures grown from metal catalysts require a second seeding step to place catalyst particles on the primary NW "trunk", generally involving a removal from the growth reactor. However, this introduces a greater possibility of unwanted contamination or oxidation, and increases process complexity. In this section an alternative multi-step approach is presented where branching NW growth is seeded by liquid AuSi alloy surface migration during an intermediate hydrogen anneal. The result is the synthesis of high quality, unkinked branched Si NWs with a high degree of control over primary and secondary NW growth and the region of branching without the need for *ex situ* seeding. Though this study is focused on branched Si NW growth alone, branches may be introduced by the rational synthesis approach presented here for a wide array of materials available in NWs grown by the VLS approach. This may potentially expand the suite of materials from which branched nanowires can be grown and permits sequential introduction of other material precursors in-process to fabricate complex branched heterostructures with new and different properties.

A schematic of the branching NW growth process is depicted in Fig. 2.8. Si NWs were grown from a 1-2 nm galvanically displaced Au film as described previously in this chapter. After primary NW growth, with the SiCl4 precursor removed, the eutectic alloy spreads from the tip down the NW sidewalls. Then, $SiCl_4$ is reintroduced into the reactor at the same rate, under the same conditions as for primary NW growth, resulting in continued growth of the primary NW (if catalyst is still present at the tip) and secondary branching growth from the alloy that spreads during the inter-growth anneal (IGA).

SEM images in Fig. 2.9 show primary NWs grown from Au film and branching NWs after various IGAs. The catalyst may not completely migrate from the primary NW tip during short IGAs, resulting in both branch growth and continued growth of the primary NW at a reduced diameter during the secondary growth period as shown in Fig. 2.9(b); longer IGAs, however, completely exhaust the catalyst from the primary NW tip, giving rise to only branch growth during the secondary growth period as shown in Fig. 2.9(c). Branches generally

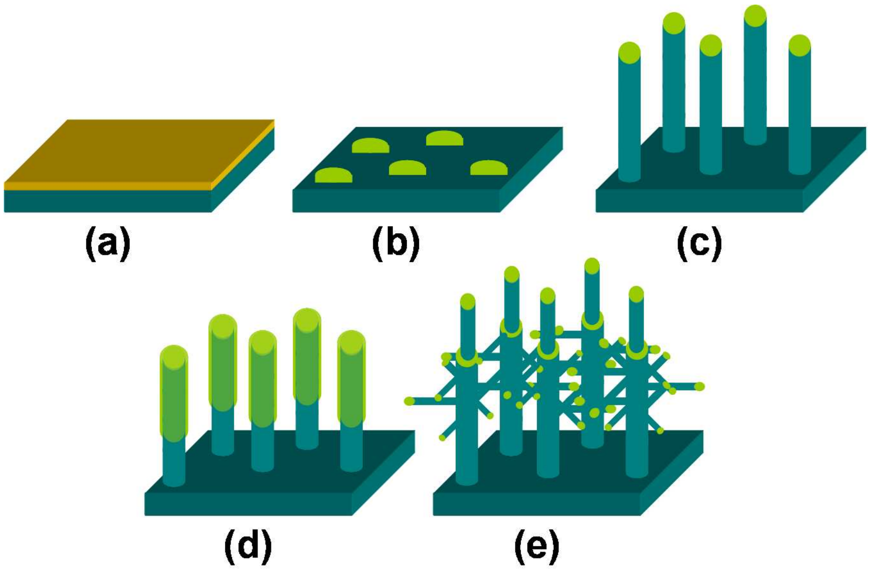

Figure 2.8: Schematic of branched NW growth process. (a) Deposition of a 1-2 nm Au film by galvanic displacement. (b) Alloying Au with Si substrate and dewetting of liquid AuSi above the eutectic temperature. (c) Growth of primary NWs. (d) Migration of AuSi from the tip during an inter-growth anneal. (e) Subsequent growth of both branching NWs seeded by the migrated AuSi and continued growth of the primary nanowire from remaining catalyst at the tip.

range in diameter from 25–60 nm for the growth conditions described above, although larger diameter branches do occur. As indicated in Fig. 2.9(d), the hexagonal facets of the primary nanowire act as basal planes for the growth of the branches. Arrows point to examples of branches grown from each facet. The 30° tilt angle of the SEM images makes the branches appear perpendicular to the primary wire while they are oriented at an angle of 70° with the primary wire. Many branches do not have a visible catalyst tip that is usually indicative of VLS growth; SEM images suggest that the catalyst for branching is depleted in the early stages of cooling the reactor to room temperature, in which Au-Si surface migration may still occur. Figure 2.9(e) shows a branched nanowire where the catalyst for the branches is still visible but has clearly begun to migrate away from the tip along the length of the branch. While the synthesis of branched Si NWs from gold catalyst with disilane precursor has been reported in a single growth step based on AuSi surface migration from the primary NW tip under controlled growth pressure, the branches it produced were highly kinked and defective [83]. On the other hand, in the work presented here, the SEM image in Fig. 2.9(f) shows the interface between a primary wire and its straight, unkinked branches, demonstrating the excellent crystallographic alignment that is possible by a multistep yet *in situ* approach using $SiCl_4$ as the growth precursor.

Given that the primary NW growth, branch seeding by AuSi migration, and branch growth occur sequentially, the process is essentially modular, allowing independent control of branch and primary NW length which is not possible in a single growth step [83]. Specifically the time of the secondary growth period dictates the length of the branches, shown qualitatively in Fig. 2.10(a) and (b). In both cases the catalyst is exhausted from the primary NW tip so that it does not grow further, while much longer branches are apparent for the five minute secondary growth period (b) than for the 30 s secondary growth period (a). Branch length is longer for 5 min. than for 30 s across the range of branch diameters, as shown in Fig. 2.10(c). The solid lines represent a linear fit of branch lengths to the inverse of branch diameters in accordance to the model proposed in Ref. [63] based on the Gibbs-Thomson effect, and exhibit good agreement with the experimental data.

Surface migration of Au-Si liquid alloy has been observed during VLS growth of Si NWs from disilane at low NW growth rates [84], but is found to be arrested at higher growth rates ($\geq 0.7\ \mu$m min^{-1}) [83]. In this study, primary NW growth rates exceed 1 μm min^{-1} and there is no apparent tapering that might indicate severe loss of catalyst from the tip during growth. However, the migration of Au-Si during IGAs is quite rapid ($> 2\ \mu$m min^{-1}), which is qualitatively supported by measurements of Au surface diffusion on Si(111)-(7 x 7) in ultrahigh vacuum at $\sim$700 °C [85]. On the other hand, surface crystallization of a Si-rich layer has been observed in bulk liquid Au-Si alloys near the eutectic temperature [86]. Furthermore, strong evidence has recently been uncovered for surface crystallization of a Si-rich layer around liquid Au-Si micro-droplets resulting from Si expulsion necessary to maintain the equilibrium liquid alloy composition during slow cooling [55]. We hypothesize that during NW growth, large fluxes of Si vapor to the Au-Si droplet (and hence fast NW growth rates) result in Si-rich layering at the droplet surface, severely inhibiting Au migra-

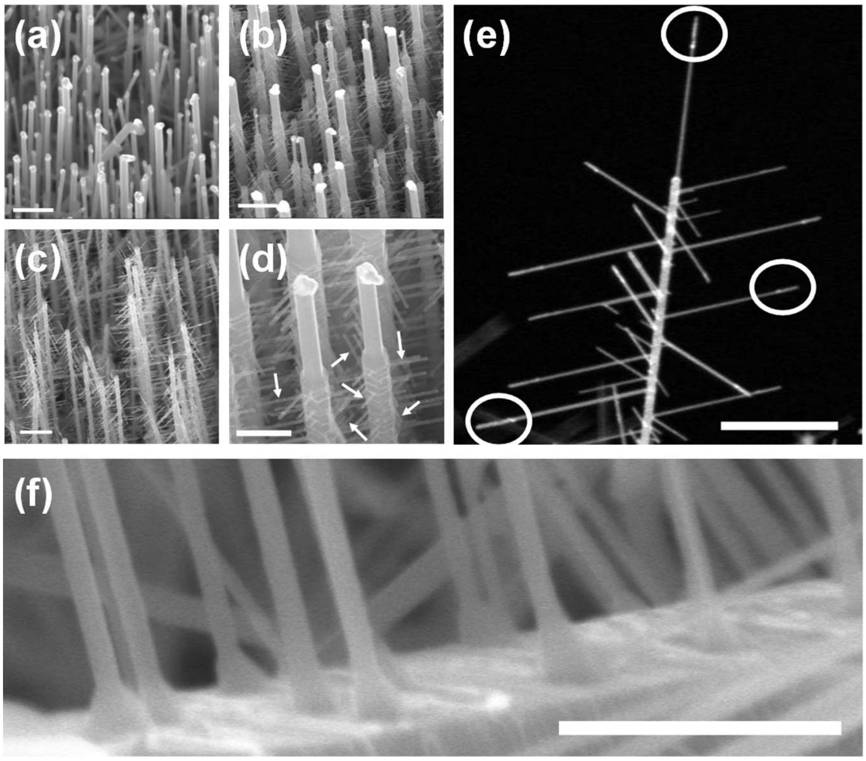

Figure 2.9: (a-d) Scanning electron micrographs of NW structures at a 30° tilt angle from the normal. (a) NWs grown from Au film for 10 min. and cooled to room temperature after growth (scale bar = 1 μm). (b) Branched NWs grown with a 2 min. inter-growth anneal followed by 1 min. secondary growth. The primary NWs continue to grow with a reduced diameter during the secondary growth period (scale bar = 1 μm). (c) Branched NWs grown with a 5 min. IGA followed by a 30 s secondary growth (scale bar = 1 μm). The gold is entirely consumed from the tip of the primary wires during the IGA, and hence no further growth is observed. (d) Branched NWs from the same sample as (b). Arrows point to wires growing out of the hexagonal facets of the primary NW (scale bar = 500 nm). (e) Cross sectional SEM of branching NWs grown with a 5 min. IGA followed by 5 min. secondary growth (scale bar = 2 μm). Contrast has been enhanced to emphasize the catalyst for branches that has begun to migrate away from the tip. Three examples are circled. (f) Close up image of branches growing off a large primary NW with a 5 min. IGA followed by a 5 min. secondary growth (30° tilt angle, scale bar = 500 nm).

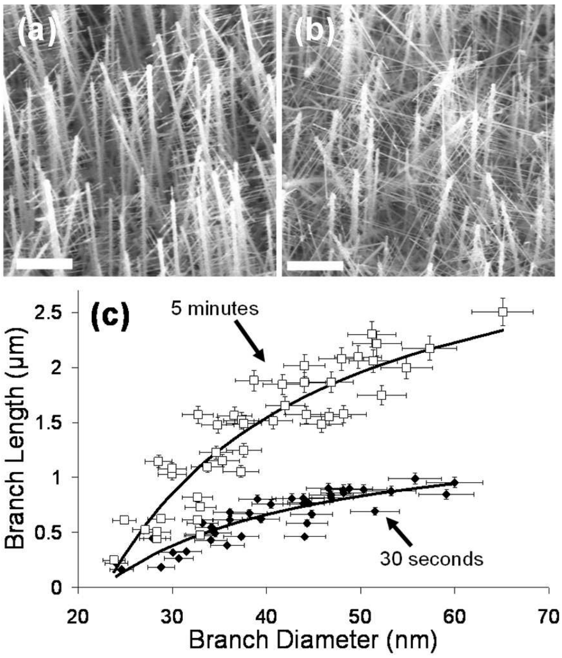

Figure 2.10: (a, b) SEM images of branching NWs grown with a 5 min. IGA followed by two different times of secondary growth (30° tilt, scale bar = 2 μm). (a) 30 s secondary growth. Most branches are less than 1 μm long. (b) 5 min. secondary growth. Many branches are greater than 2 μm long. (c) Lengths of branches as a function of branch diameters. The linear fit to inverse branch diameter is shown (solid lines), following Ref. [63].

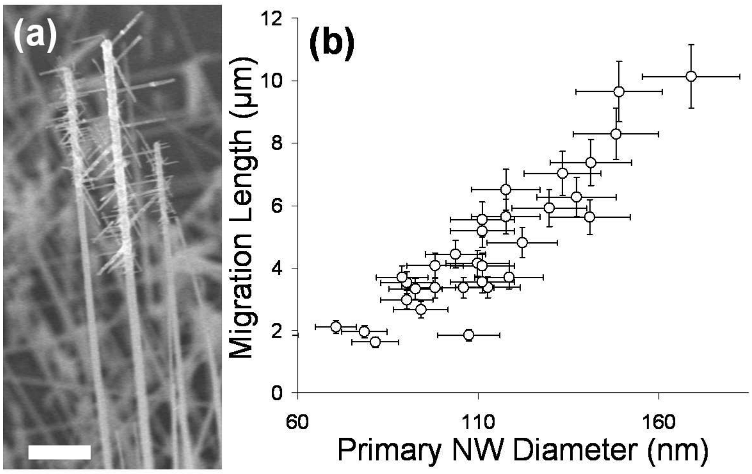

Figure 2.11: Total migration length dependence on primary NW diameter. Data are from wires that underwent a 5 min. IGA, followed by 30 s secondary growth. (a) SEM image of wires with the alloy completely consumed at the tip, resulting in no continued growth of the primary NW (30° tilt, scale bar = 1 μm). Total migration length is taken to be the distance from the top to the point at which branching ends and the sides of the primary NW are smooth. (b) Total migration length as a function of NW diameter, due to the limited Au-Si alloy material available on the tip before the IGA step.

tion. This layering may even prevent the formation of an approximately 1 monolayer gold silicide equilibrium wetting layer on the NW sidewalls, upon which excess Au (or Au-Si liquid alloy) is known to be highly mobile at elevated temperature ($\geq$ 600 °C) [84, 87]. Severe reduction or complete elimination of the vapor Si flux during the IGA removes this kinetic barrier to Au-Si wetting equilibrium; consequently the liquid alloy rapidly diffuses along the wire surface. Ultimately, the maximum possible migration length is limited by the amount of alloy available in the droplet, and it increases with increasing NW diameter, as shown in Fig. 2.11.

The presence of H_2 during the IGA is crucial for achieving branching NW growth. This was verified by performing 5 min IGAs in both H_2-Ar and pure Ar. SEM images (Fig. 2.12(a)) show that in the case of annealing in H_2-Ar, NW branching occurs (30 s secondary growth), while it does not when annealing is done in pure Ar. In the latter case, splitting and/or continued growth from the primary NW tip is observed. The key difference may be attributed to the presence of small amounts of oxygen in the reactor. It has been shown that adding a small amount of oxygen (as low as ~1 ppm) from either an atmospheric or a surface source during growth inhibited eutectic alloy migration away from the NW tip, dramatically reducing NW tapering [88]. Thus, a small amount of residual oxygen unavoidably present in our growth reactor would be sufficient to inhibit the eutectic alloy migration during the annealing process, yielding the results shown in Fig. 2.12(b). Another possibility is the inhibition of Au migration by Si surface chlorination from residual HCl [89]. For either case, we postulate that the presence of hydrogen during the annealing process may prevent oxidation or remove surface chlorination, leaving the NW sidewalls pristine. The result is that for annealing in H_2, the eutectic alloy is able to spread homogeneously, leading to the branching observed in Fig. 2.12(a). The chemical nature of this process (instead of a physical process, such as a change in pressure or temperature) affecting Au-Si migration suggests that careful control of the annealing gas composition may provide fine control over the Au-Si migration length, and hence the region of branching, which could be exploited in future technological applications.

The crystallinity of the branching NWs was studied with scanning confocal Raman spectroscopy. Branched NWs were dispersed from suspension in ethanol onto a glass slide. Figure 2.13(a) shows a scanning confocal Raman map of a branched NW on glass, along with an optical image of the same NW (inset). In general, the Si Stokes peak of the structure ranges from 520 to 522 cm^{-1}, whereas the Stokes peak for bulk single crystal silicon is 521 cm^{-1}; polycrystalline Si has a peak of variable position at lower wavenumber and is asymmetrically broadened towards lower wavenumber while amorphous Si exhibits a broad peak in the region of 420-540 cm^{-1}. Individual spectra from several points on the structure further indicate its crystallinity as shown in Fig. 2.13(b). The spectrum from point A (primary wire) exhibits a Stokes redshift of about 2 cm^{-1}, which is likely explained by local heating. Indeed, it should be noted that its intensity is about 8 times higher than on the other points, meaning that the primary wire fell within the focal point of the laser, leading to a higher signal but also more intense local heating, which in turn redshifts the Stokes peak.

The structure of the primary NWs and branches was characterized in detail by TEM. Figure 2.14 shows a TEM image of a representative branched NW. Selective area electron diffraction of the primary NW (A), a branch in the same image plane as the primary NW (B), and the junction between the primary NW and the branch (C) shows identical diffraction patterns which are all consistent with that of single-crystal silicon along the $[\bar{1}10]$ zone axis. This confirms that the structure of both the primary NW and the branch is single-crystalline throughout. The angle between the branch and the primary NW is $70.7 \pm 0.5°$, which is also consistent with branch growth along a $[\bar{1}11]$ direction. (The same angle was measured for several other branches on multiple wires, resulting in an average angle of $70.9 \pm 0.2°$ or $54.8 \pm 0.3°$; the latter corresponds to the two-dimensional projection of the $[\bar{1}11]$-to-$[111]$angle for a branch growing 60° out of the image plane.) Since these TEM images are taken with the primary NW and the branches aligned along the $[\bar{1}10]$ zone axis, and as noted previously the branches grow out of hexagonal facets, we infer that the branches show a strong preference for growth in $[\bar{1}11]$ directions from $(\bar{1}\bar{1}2)$ facets of primary NWs. Therefore, the growth of branches by this process exhibits high quality epitaxy that is directed by the crystallinity of the primary NWs, a fact that may be important for potential applications of these structures.

In summary, a new method of synthesizing branched silicon NWs with control over region of branching has been demonstrated. By relying on the unimpeded migration of Au-Si

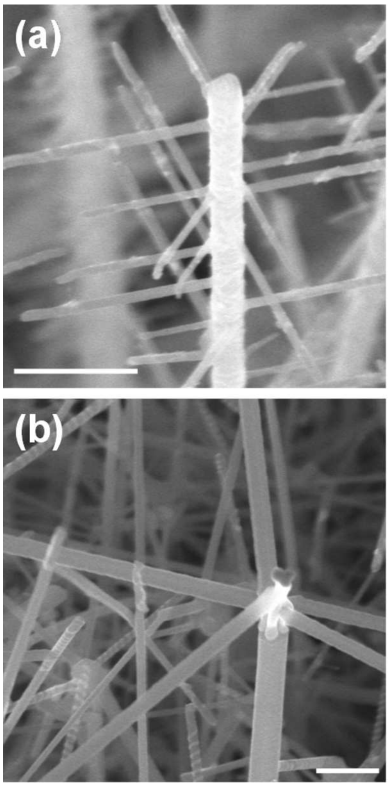

Figure 2.12: SEM images showing the effect hydrogen during the IGA for branching growth. Tilt angle is 30° and scale bars are 500 nm. (a) Five minute IGA in 10% H2 in Ar, followed by a 30 s secondary growth. At a 30° tilt, the branches appear to be perpendicular to the primary wire, while they are actually at a 70° angle, as determined by TEM analysis. (b) Five minute IGA in Ar only, followed by 5 min. secondary growth. While multiple nanowires grow from the primary nanowire tips, there are no signs of regular branching as seen in the H_2 case.

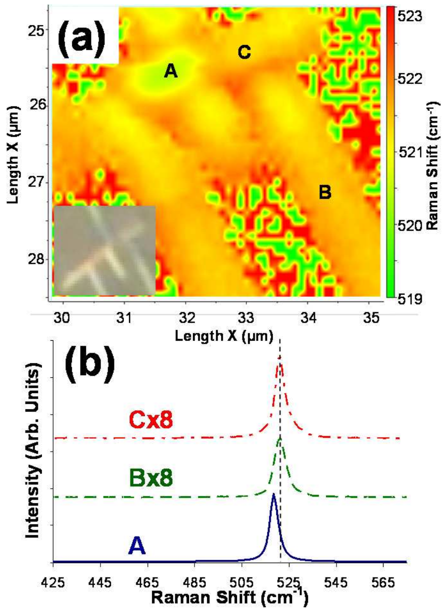

Figure 2.13: Scanning confocal Raman map of a branched NW. (a) Map of peak position. Inset shows an optical image of the mapped NW. Intensity ranges from 519 to 523 cm^{-1} and step size is 100 nm for a 632 nm wavelength laser. Most of the structure has a peak position around 521.3 cm^{-1}, which is near the appropriate Stokes peak for single crystal Si (521 cm^{-1}). The bright mottled green and red background corresponds to the glass slide, which has no Stokes peak. In the map the NW appears larger than it actually is due to the diffraction limit of visible light. (b) Raman spectra for points A, B, and C. The dashed line is through 521.3 cm^{-1}.

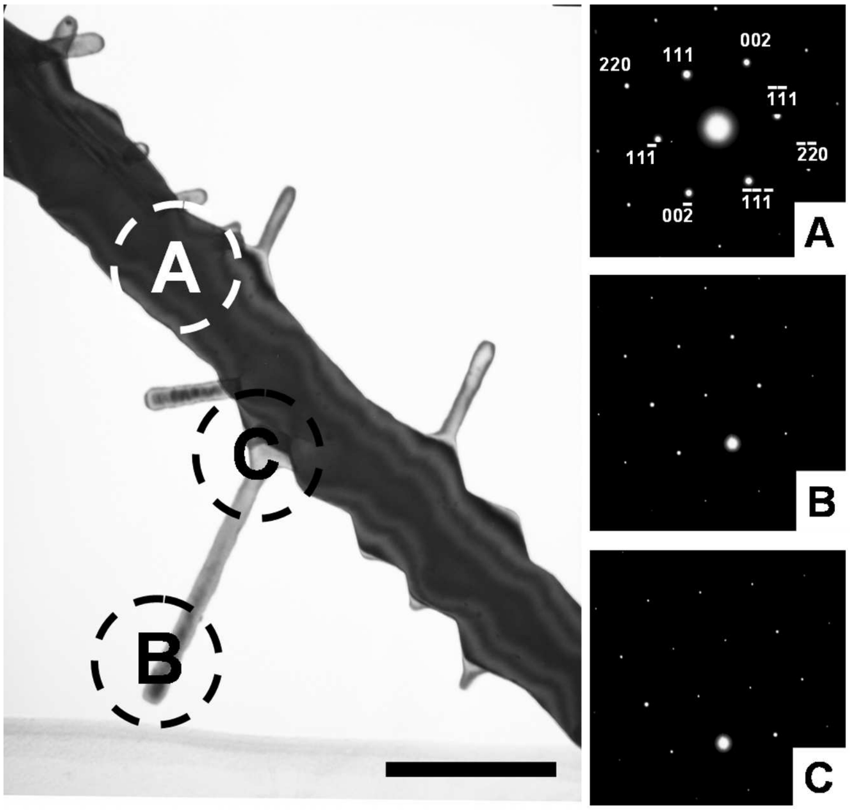

Figure 2.14: TEM image of a branched NW. Scale bar is 200 nm. Selective area electron diffraction patterns centered on A, B, and C with the primary NW and the branch aligned along the [$\bar{1}$10] zone axis. Diffraction pattern A is indexed for convenience. The angle between the branch and the primary NW is 70.7 ±0.5°. These measurements indicate that the branch grows along the [$\bar{1}$11] direction and forms a continuous single-crystal silicon structure with the primary NW.

eutectic alloy during an anneal in hydrogen to seed the branched growth, no additional seeding step is required, reducing process complexity and eliminating the need to expose the sample to atmosphere. Using $SiCl_4$ as the precursor gas, the branches are straight, unkinked, and naturally aligned in $[\bar{1}11]$ growth directions on the $(\bar{1}\bar{1}2)$ hexagonal facets of the primary NWs. Annealing in the presence of H_2 is shown to be important for branching, most likely by preventing the surface oxidation or chlorination that impedes Au-Si migration, indicating how chemistry may be used to control Au-Si migration in NW growth processes. Raman microscopy and TEM confirm the high quality, epitaxial, single-crystal nature of the branches. Overall, this work highlights a facile route for the rational synthesis of high quality, complex structures such as branched NWs; the primary NW growth, region of branching, and secondary growth may be controlled independently, rendering the process essentially modular. Thus, while this process has been confined to silicon in this study, the primary NW and branches can be made in principle from different materials such as differently doped Si (to make pn junctions at the branch points), Ge, or even GaAs, opening a wealth of possible new applications for these complex nanostructures.

2.3 Faceting of Si Nanowires and Nanotrees

This section is reproduced in part with permission from: G.S. Doerk, V. Radmilovic, and R. Maboudian. Branching induced faceting of Si nanotrees, *Appl. Phys. Lett.*, 96(12):123117, 2010. Copyright 2010 American Institute of Physics.

Surface morphology is distinctly important with regard to nanowire properties [24, 72], and thus for the optimal implementation of NWs and nanotrees in emerging technology, it is crucial to understand the effects that synthetic processes have on surface morphology. Silicon NWs grown according to the VLS process larger than approximately 20 nm in diameter that generally grow in the <111> direction exhibit hexagonal cross-sections composed of {112}-type sidewalls [52, 37]. In most cases, these sidewalls are apparently smooth but several groups have recently reported cases of sawtooth faceting [90, 91, 92, 93]. In this section we report sawtooth-type faceting on primary nanowire trunks induced by the nucleation of secondary NW branches. The major crystal planes on which faceting occurs are identified, and the results are differentiated from facets that arise from Au surface migration or diffusion alone.

Scanning electron microscope (SEM) images were taken of the nanotrees as-grown using a FEI Strata 235 field emission SEM. For transmission electron microscopy (TEM) characterization, nanotrees were drop cast from suspension in ethanol onto holey-carbon coated TEM grids. Low resolution TEM images and selected area diffraction patterns were acquired at 200 kV using a Jeol200CX, while high resolution TEM (HRTEM) images were acquired at 200 kV using a FEI Tecnai TEM.

Figure 2.15(a) shows a SEM images of as-grown nanotree after an IGA of only 1 min. The catalyst was not completely exhausted from the trunk NW, allowing for continued trunk

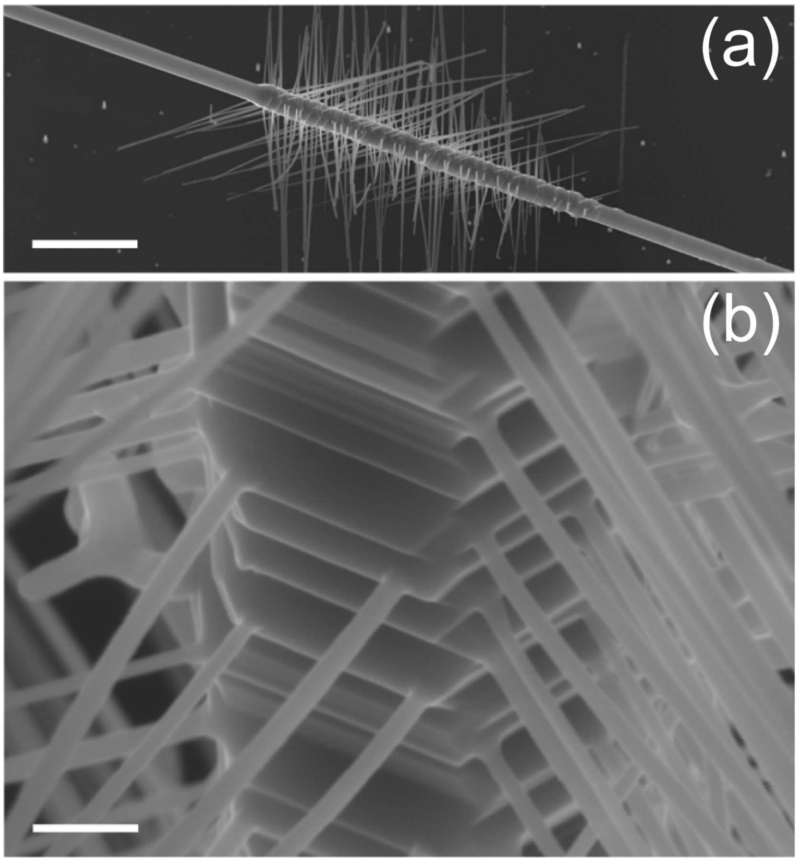

Figure 2.15: SEM images of as-grown nanotrees. (a) Nanotree with a branching region confined by the extent of Au migration. The trunk is thicker and faceted in the branching region (scale bar = 2 μm). (b) Close-up of a branched region on another nanotree exhibiting a sawtooth-faceted trunk (scale bar = 200 nm, 30° tilt).

growth during the branching stage. Furthermore, the Au could not travel completely down the trunk during the IGA leaving the lower section of the trunk without branches and smooth. The trunk in the branching region is notably thicker and rougher. A close-up of a branching region on another Si nanotree (Fig. 2.15(b)) reveals a periodic sawtoothlike subfaceting on the {112} sidewalls. These images reveal the presence of sawtooth subfaceting confined to the region of branching only.

This sawtooth faceting could arise during either the IGA or the subsequent branch growth period. Gold has been shown to induce faceting on Si surfaces previously [94]; thus to better elucidate the role of Au in the faceting, Si NWs were investigated by electron microscopy at various stages in the nanotree synthesis process. Figure 2.16(a) is a TEM image of a Si NW cooled immediately after growth, while Fig. 2.16(b) is a TEM image of an Si NW after a 5 min. IGA, where Au has been exhausted from the NW tip and has migrated along the sidewalls. Both images are viewed along a <110> direction that permits examination of the {112} sidewalls edge-on. A corrugation along the NW sidewalls visible in Fig. 2.16(b) is not present in the image of the NW in Fig. 2.16(a). Figure 2.16(c) is a low magnification HRTEM image of a Si NW from the same sample as the NW in Fig. 2.16(b), and Fig. 2.16(d) is a high magnification image of the particular facet indicated by an arrow in 2.16(c). A Fourier transform (Fig. 2.16(e)) of Fig. 2.16(d) permits precise indexing of these facets as {113} and {111}. Other researchers have reported sawtooth facets on the {112} sidewalls of as-grown Si NWs composed of long {113} facets and short {111} facets [91, 95]. In-situ spot-profile-analyzing low energy electron diffraction during controlled Au evaporation on Si(112) has suggested that these facets are Au-induced with preferential segregation of Au to the {111} facets [91]. The results here demonstrate that these facets can be formed through restructuring the Si surface by Au migration independently of NW growth.

The faceting of nanotrees was studied in detail using HRTEM. Figure 2.17(a) is a low magnification TEM image of a nanotree taken from a <110> direction, with the <111> growth direction noted. A fraction of branches are in the image plane of the trunk and the sidewall subfaceting is readily apparent. Figure 2.17(b) is a HRTEM image of the faceted edge region demarcated by a box in Fig. 2.17(a). A Fourier transform of this image (Fig. 2.17(c)) indicates that the facets are single-crystal and are bound by {111} and {100} crystal faces. Figure 2.17(d) shows a schematic diagram of a faceted Si nanotree viewed from the <110> direction, with the {112} sidewalls bound by {111} facets and {100} facets. For clarity, only branches growing in the image plane are depicted.

An important feature of the schematic model in Fig. 2.17(d) is that branches are found only at the edge of the {111} facets, which is consistent with the low magnification image in Fig. 2.17(a). Expansion at the base of Si NWs grown epitaxially on Si substrates has been identified and attributed to the transition in contact angle of the recessed Au-Si eutectic liquid droplet at equilibrium with a Si substrate [55] to one that sits atop a flat growth front [96, 97]. If anisotropic surface energies are present, this basal pedestal formed during nanowire nucleation will be faceted [97]. In light of the fact that that the equilibrium shape of Si is dominated by {111} and {100} surfaces [98, 99], these basal structures are most likely to exhibit {111} and {100} facets. Thus, the sawtooth-type nanotree trunk facets in the region of branching may be understood as basal pedestals formed during branch nucleation, and each branch is found at the edge of a {111} facet because the nucleation of that branch formed the corresponding facet.

Recent reports of sawtooth facets on <111> growth direction Si NWs closely match those discussed here, with {111} facets and {100} facets observed in the case of *in situ* boron doping [93], as well as for growth after a change in the growth orientation from <112> to <111> [92]. The former case may be explained by the enhanced vapor-solid growth that is often seen during *in situ* boron doping with facets nucleated by boron impurities [93], while in the latter case VLS growth in the <111> direction was much slower than growth in the <112> direction [92]. This may allow for a higher degree of both vapor-solid growth and

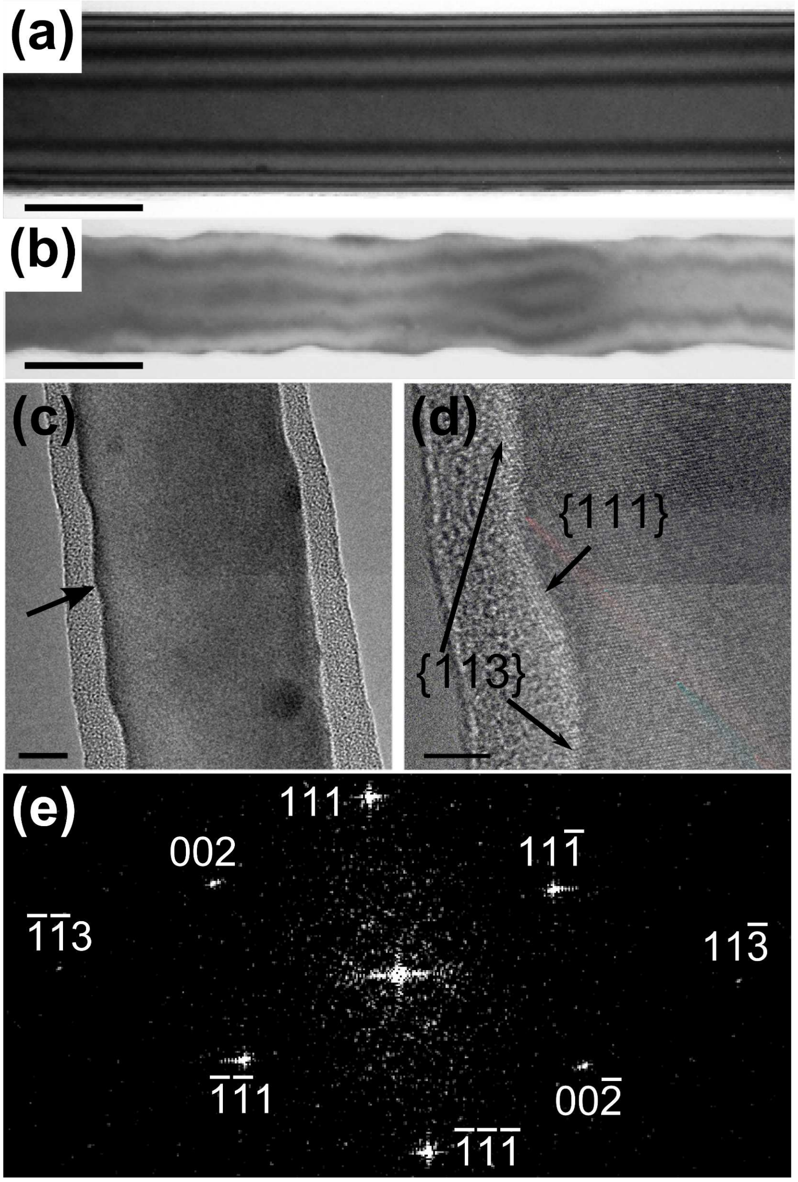

Figure 2.16: TEM images before and after Au migration. All images are viewed from a <110> direction. (a) TEM image of a Si NW cooled to room temperature immediately after growth (scale bar = 100 nm). (b) TEM image of a Si NW after a 5 min. IGA (scale bar = 100 nm). (c) Low magnification HRTEM image of a Si NW from the same sample as the wire in (b) (scale bar = 10 nm). (d) Higher magnification HRTEM image of the facet marked by an arrow in (c) (Scale bar = 5 nm). (e) Indexed Fourier transform of the image in (d).

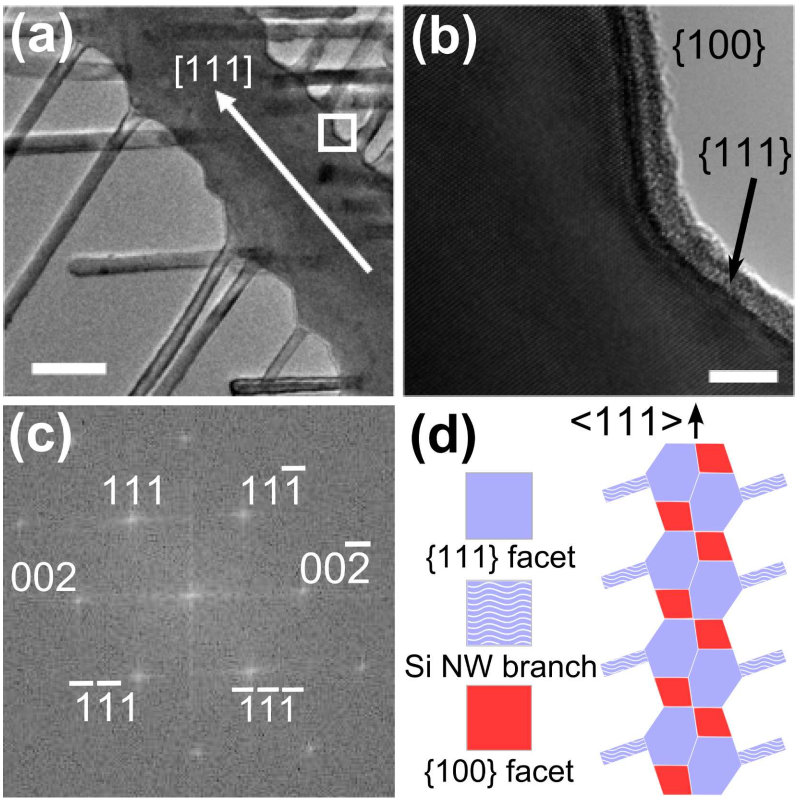

Figure 2.17: (Color online) (a) Low magnification HRTEM image of a nanotree viewed from a <110> direction (scale bar = 100 nm). (b) HRTEM image of a facet demarcated by a box in (a) (scale bar = 5 nm). (c) Indexed Fourier transform of the image in (b). (d) Schematic of a nanotree viewed from a <110> direction.

Au migration [84] in the <111> growth direction regions of the wire. Indeed, simultaneous branch growth was sometimes witnessed in these regions [92]. These examples suggest that the {111}/{100} sawtooth facets on the {112} nanotree sidewalls reflect a more general pattern of epitaxial overgrowth.

2.4 Silicon Nanowire Synthesis by Ag-Based Electrochemical Etching

The previous sections have addressed synthesis of Si nanostructures based on the VLS mechanism. NWs produced by VLS-based processes typically possess excellent crystal quality and very smooth surfaces. This along with the capability for synthesis of diverse NW-based heterostructures, and the possibility for controlled growth at nanoscopic dimensions from single NWs to large and dense arrays entice their use in a number of devices. On the other hand, complications in NW growth kinetics, reactor limitations to high-throughput production, and the cost of high temperature CVD may hamper their viability for some envisioned applications. These cases would benefit instead from NW synthesis methods that are simple, inexpensive, highly uniform, and robust.

One group of techniques that meets a number of these requirements for Si NWs is metal-catalyzed or metal-assisted electrochemical etching. While there are significant disadvantages to these techniques, their facility has resulted in widespread adoption by a number of research groups. The group may be divided into two categories. In the first, a metal film is deposited by any method and the sample is immersed in an isotropic Si etchant that consists of an oxidizing agent and HF. The metal enhances electrochemical oxidation locally, giving rise to anisotropic etching. The major advantage of this technique is that the metal film may be patterned to achieve very tightly controlled vertical nanostructures with excellent pattern registry. Unfortunately, under uniform etch conditions the etch rate is often slow, and in some cases unwanted nanoporosity may develop in the silicon [100]. The second category is based on the galvanic displacement of Ag from $AgNO_3$ at high HF concentrations. The Ag oxidizes the Si rapidly, but the slower diffusion of Ag ions to the Si surface combined with the high electrical conductivity of Ag gives rise to dendritic Ag growth instead of a uniform Ag film. The non-homogeneous substrate coverage thus leads to deep channeling into the Si and the production of NW arrays [101]. The NW arrays are very dense, and etch rate uniformity across the substrates is typically quite good, making this a process that may be applied on the wafer scale. NW diameter is not tightly controlled and the NW surfaces are usually much rougher than the surfaces of VLS-grown NWs. Indeed these are the NWs with the drastically reduced thermal conductivities discussed in the Introduction. Since only Si NWs synthesized by the second route are featured in later sections of this dissertation, the following paragraph describes their synthesis in more detail.

Electrochemically etched (EE) Si NWs were synthesized following the general procedure

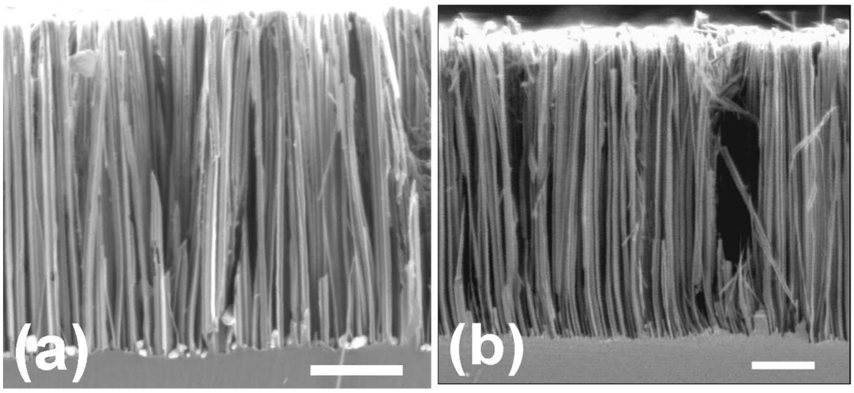

Figure 2.18: (Si NWs synthesized by Ag-catalyzed electrochemical etching of (a) Si(100) and (b) Si(111) wafers. Scale bars = 2 μm for both images.

of Peng *et al* [101]. Starting Si dice were either single crystal Si(100), p-type (ρ = 10-30 Ω-cm) or on-axis single-crystal Si(111), n-type (ρ = 1-5 Ω-cm). Samples were sonicated in acetone and IPA, rinsed with DI H_2O, and dried in N_2. The sample dice were then immersed in a solution of 20-40 mM $AgNO_3$ and 5 M HF for 2 hours or less, at an etch rate of approximately 5 μm/hr. After etching, the samples were rinsed with deionized (DI) H_2O to remove Ag dendrites that grow during the etching process, and immersed into concentrated nitric acid for at least one hour to remove any remaining Ag. Finally, the samples were immersed in concentrated HF for 1 minute to remove any SiO_2. Figure 2.18(a) and (b) show SEM images of as-synthesized EE Si NWs produced from Si(100) and Si(111) chips, respectively.

Intriguingly applying this technique to highly boron-doped Si(100) samples results in the formation of mesoporous single crystalline Si NWs, as reported previously by Hochbaum *et al* [102]. In this case boron doped Si(100) ($\rho = 5 - 10$ mΩ-cm) diced were immersed in a 0.02 M $AgNO_3$ solution with 4 parts DI water to 1 part 48-50 % HF by volume for 2 hours or less for temperatures from 20-50 °C. An SEM image of an porous EE Si NWs synthesized at 50 °C for 45 min. is given in Fig. 2.19(a). The height of this very dense Si NW array is just over 30 μm, but arrays approximately ~60 μm tall have been fabricated. A TEM image of a single Si NW synthesized in this manner is shown in Fig. 2.19(b), where the mottled contrast is most likely attributable to porosity (note that no silicon oxide has been removed from the NW external or internal surfaces). The spot pattern found by selective area diffraction from this NW (inset) indicates that it is indeed single-crystal, but the significant arcing of the spots may indicate angular distortion of the crystal and possibly some crystal fragmentation that occurs during the drying process [103].

Hochbaum *et al* measured a mean surface area for these porous Si NWs of 342 m^2g^{-1} based on the Brunauer-Emmett-Teller (BET) nitrogen adsorption method, and found that

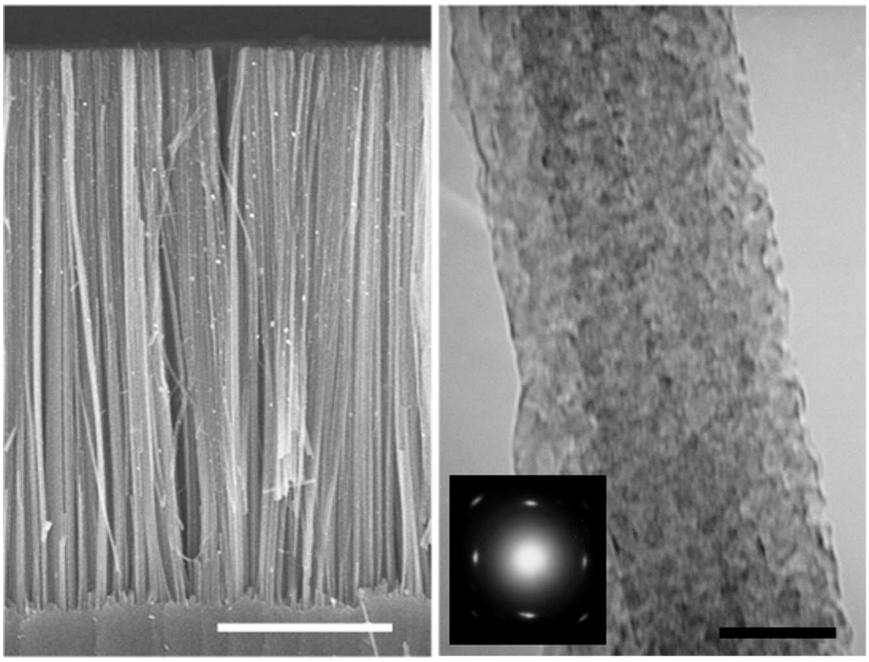

Figure 2.19: (Porous Si NWs synthesized by Ag-catalyzed electrochemical etching of boron doped wafers with resistivity < 10 m$\Omega - cm$. (a) SEM image of as-made Si NWs after an etch duration of 45 min (scale bar = 10 μm). (b) TEM image of a single porous Si NW (Scale bar = 50 nm). The inset shows a selected area diffraction pattern from this wire. Arcing of the individual diffraction spots may arise due to crystal angular distortion or fragmentation.

the NWs exhibited the expected photoluminescence of porous Si [102]. Combined with the high density and pseudo-monolithic nature of the as-fabricated porous Si NW arrays, this simple approach may be employed in a variety of photonic, catalytic, or electrochemical applications.

Chapter 3

Device Integration and Doping of Silicon Nanowires

This chapter presents strategies for epitaxial NW integration in arbitrary geometries. Particular attention is paid to epitaxial bridging Si NWs, which present an excellent platform for in-plane NW-based devices. This is followed by a discussion of block copolymer micelle templated galvanic displacement to controllably seed the growth of small numbers of VLS-grown Si NW-based epitaxial devices. Finally, controlled *ex situ* boron doping of Si NWs based on the hydrogen reduction of BBr_3 is discussed.

3.1 Epitaxially Bridging Si Nanowires

In order to fabricate VLS NW-based devices in a scalable manner, the NW pattern registry must be carefully defined by controlling the position and number of NWs in devices. For epitaxial growth, this implies precise control over catalyst nanoparticle seed size and placement. Special substrates were fabricated using standard lithographic and CMOS fabrication processes that exploit preferential catalyst deposition made possible through chemical means such as galvanic displacement. A schematic of the substrate fabrication process is presented in Fig. 3.1, and further details may be found elsewhere [104]. Beginning with a (110) silicon-on-insulator (SOI) wafer, the device layer (doped with 10^{18} cm^{-3} boron atoms by ion implantation) is thermally oxidized to produce a top SiO_2 layer. Main structural features such as electrodes and large cantilever beams are defined by optical lithography and reactive ion etching of the top SiO_2 and Si layers. Due to the preference for growth in the <111> crystallographic direction, the faces are coincident with the {111} planes whenever possible. A silicon oxide film is then deposited by CVD and a second mask is used to lithographically define regions in which the oxide will be etched. These exposed silicon regions, or “oxide windows” are where the metal seed particles (i.e. Au) are to be selectively deposited. After wire growth the top oxide layer is removed with HF vapor to make electrical contacts. In

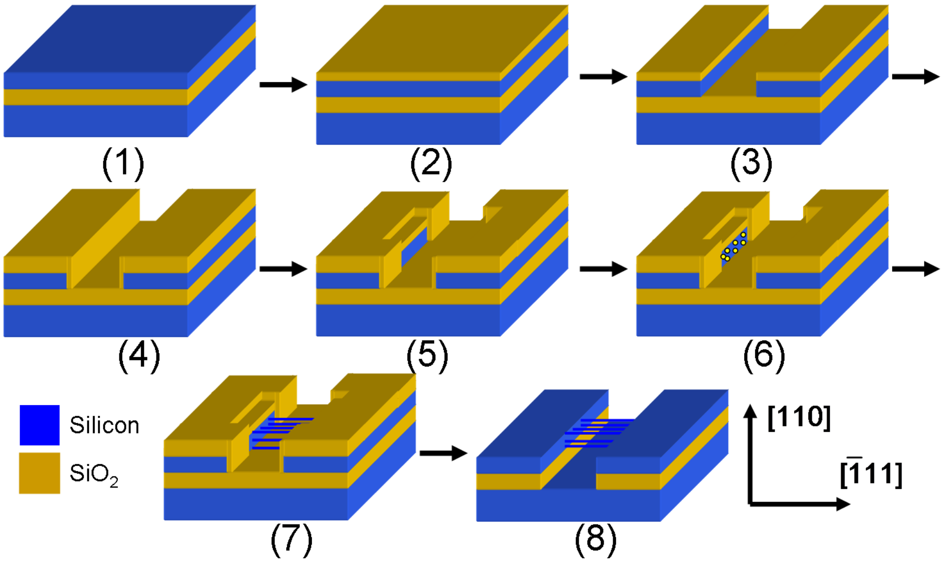

Figure 3.1: Schematic of the process flow for epitaxial Si NW device fabrication: (1) Starting silicon-on-insulator wafer with highly boron doped device layer; (2) Thermal oxidation; (3) Lithography and etching for trench fabrication; (4) Oxide deposition by CVD; (5) Second pattern and etch steps to create oxide “windows”; (6) Selective Au nanoparticle deposition in windows; (7) Epitaxial Si NW growth; (8) Removal of oxide hard mask.

the early stages of research two methods were used to deposit Au nanoparticle (NP) seeds: Galvanic displacement in reverse microemulsions and Au colloid deposition from acidified colloidal suspensions.

3.1.1 Gold Nanoparticle Deposition via Galvanic Displacement in Reverse Microemulsions

Gao *et al* employed galvanic displacement in water-in-oil microemulsions with micelles containing an aqueous solution of a Au salt and hydrofluoric acid to deposit Au NPs selectively onto Si microtrench sidewalls and flat Si substrates with controlled nanoscale diameters to seed the subsequent growth of epitaxial Si NWs [79]. This approach was pursued in earnest given its obvious utility in the above strategy for epitaxial NW device integration. Dioctyl sulfosuccinate, sodium salt (AOT) was used as the surfactant and n-heptane as the organic phase, and the size of the deposited Au clusters was controlled by the ratio R = [water]/[AOT]. To obtain microemulsions, solutions of AOT in n-heptane are prepared with concentrations varying from 5 - 330 mM, to which the galvanic displacement solution consisting of of 10 mM $KAuCl_4$ and 0.2 M HF in DI water was added *via* micropipette to obtain the desired R value. The mixture was sonicated in a water bath for 1 hour and filtered.

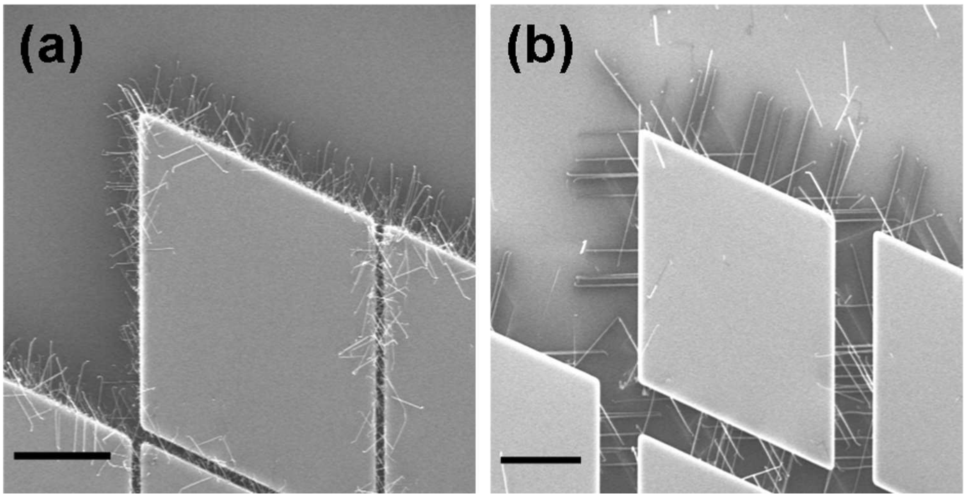

Figure 3.2: Si NWs grown on device substrates from catalyst seeds deposited by two different methods, (a) galvanic displacement from a reverse microemulsion and (b) acidified Au colloidal suspension. NW growth was conducted for 10 min. under the same conditions for both cases. The scale bars are 10 μm for both images.

After this, clean dice were immersed in the mixture for 1 - 30 s.

The top-view SEM image in Fig. 3.2(a) demonstrates the results of Au deposition by galvanic displacement from reverse microemulsions. Only the sidewalls of the Si electrodes present exposed Si on which Au may be deposited (on top is a SiO_2 film and underneath is the buried oxide layer), and thus Si NWs only grow from here. Unfortunately the NW density is quite high and many of them exhibit kinking that most likely arises due to crystal defects. Reducing micelle concentration and immersion time should reduce the density. However, the density did not decrease significantly with reduced AOT concentration, and immersion times had to be reduced to $\sim$1 s to achieve the desired NW density for single- or few-NW devices. The high density may be a product of the dipping technique itself, as a significant portion of AOT likely accumulates at the air/liquid interface. Though the reason for the poor quality of the resulting NWs is not completely understood, this fact has motivated the exploration of other Au deposition techniques.

3.1.2 Semi-selective Au deposition on Si from Acidified Colloidal Suspensions

As mentioned in the previous chapter, the acidified Au colloidal deposition method employed by Woodruff *et al* [68] exhibits a degree of selectivity for Si over SiO_2 – making it ideal for the integration strategy presented here. Therefore, we used the same deposition process described in the previous chapter on the patterned SOI samples for times ranging from 2-10 min. Figure 3.2(b) shows an SEM image of Si NWs grown from 50 nm Au colloids deposited by this method. The diameter is fairly well controlled (though it is affected by some tapering during growth) and the Si NWs grow longer and with less kinks, most likely indicating better crystal quality. Most importantly, the NW density is much lower and more well controlled. Using this technique, in some cases single Si NWs could be grown between $\sim$1-2 μm^2 SiO_2 windows that epitaxially bridge Si electrodes for potential device fabrication.

Unfortunately, the selectivity for Si was imperfect, and some Au colloids were deposited on the oxide. In most cases there were not any serious problems, but in some cases Au colloids were deposited everywhere, resulting in NW growth on Si and silicon oxide alike. In general, the Au colloid deposition was quite sensitive to the post-deposition DI water rinsing conditions. Misplaced Au colloids were present even after HF etching (liquid or vapor phase). Quitoriano and Kamins developed a clever solution to this problem for in-plane epitaxial growth of Si NWs on SOI substrates [105]. After depositing 40 nm Au colloids from an HF acidified suspension, they annealed the sample at 400 °C (above the Au-Si eutectic temperature) in an H_2 ambient. This immobilized the Au alloyed with Si, but permitted removal of any Au on oxide surface by subsequent HF etching. While this seems somewhat in contradiction to the results presented here (where Au remained after HF etching), the difference may be attributable to the particularities of their etching and subsequent cleaning steps. Nonetheless, the deposition of Au colloids from an HF acidified suspension is currently a random process, which makes it unsuitable for a scalable integration strategy for epitaxial Si NW devices based on VLS growth.

3.1.3 Mechanical Resonance Testing

Epitaxial NW growth in microtrenches has proven particularly useful in the fabrication and testing of NW-based nanomechanical resonators [12, 47]. Therefore, single epitaxially bridging Si NWs were tested for resonance behavior. A number of techniques have been devised to actuate and detect nanomechanical resonators [106]. However, capacitive actuation is particularly simple and accessible, and electronic detection is the most likely to be realized in real devices, especially for NWs with a double-clamped geometry. Capacitive actuation is achieved by applying a potential V (possessing both a DC and an AC component) with respect to the NW to a "drive electrode" separated from the NW by a gap g_o. The resultant force (F) on the NW of projected area A is given by

$$F = \frac{1}{2}V^2\left(\frac{dC}{dx}\right) \approx -\frac{1}{2}V^2\left(\frac{\varepsilon_o A}{g_o^2}\right) \tag{3.1}$$

where C is the capacitance between the drive electrode and the NW at g_o, ε_o is the permittivity of free space, and x is the displacement of the NW towards the drive electrode. The approximate expression in the right part of 3.1 is valid for $x \ll g_o$.

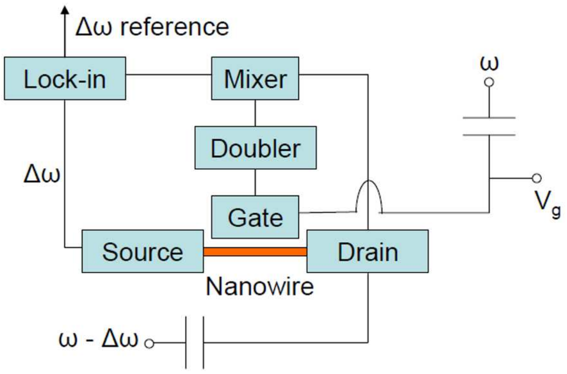

Figure 3.3: Schematic of the frequency mixing setup for measuring NW mechanical resonance by the 1ω method.

Under capacitive actuation, the resonant frequency is typically measured by monitoring the displacement current I_d between the resonator and the drive electrode, given by

$$I_d = C\left(\frac{dV}{dt}\right) + V\left(\frac{dC}{dx}\frac{dx}{dt}\right) \tag{3.2}$$

At resonance, the displacement current will spike due to the dx/dt term. However, any other nearby current-carrying structures will form a capacitor with the drive electrode and generate extraneous displacement currents according to the first term in 3.2. In fact, the much larger projected areas for these parasitic capacitances results in displacement currents that may completely mask the signal from the nanomechanical resonator. One method that has been used to circumvent this problem for capacitively driven NW or nanotube based resonators is frequency mixing [107].

In a frequency mixing-based detection scheme the drive electrode applies a DC component and an AC component at a frequency ω, the same as before. An additional AC current is applied across the NW ("source to drain") at a frequency $\omega - \Delta\omega_{mix}$, where $\Delta\omega_{mix} \ll \omega$. Though nonlinearities in the source-drain signal in response to the drive signal provide a number of signals that may be detected, in simple terms the displacement current is mixed with the source-drain current. One component is at $\Delta\omega_{mix}$ only, where it is not obscured by parasitic displacement currents (that are proportional to ω). Monitoring this signal with a lock-in amplifier enables detection of small-signal resonant behavior [107]. Frequency mixing experiments were performed in collaboration with Haibing Peng, who was a postdoctoral scholar in the lab of Prof. Alex Zettl at that time. The value of $\Delta\omega_{mix}$ used was 7 kHz. A schematic of the measurement setup is given in Fig. 3.3.

Primarily using the acidified colloidal suspension method for Au deposition, single epitaxial bridging Si NW devices were fabricated. An example is shown in the inset of Fig. 3.4. The DC current-voltage measurement for this NW in Fig. 3.4 relates several key features

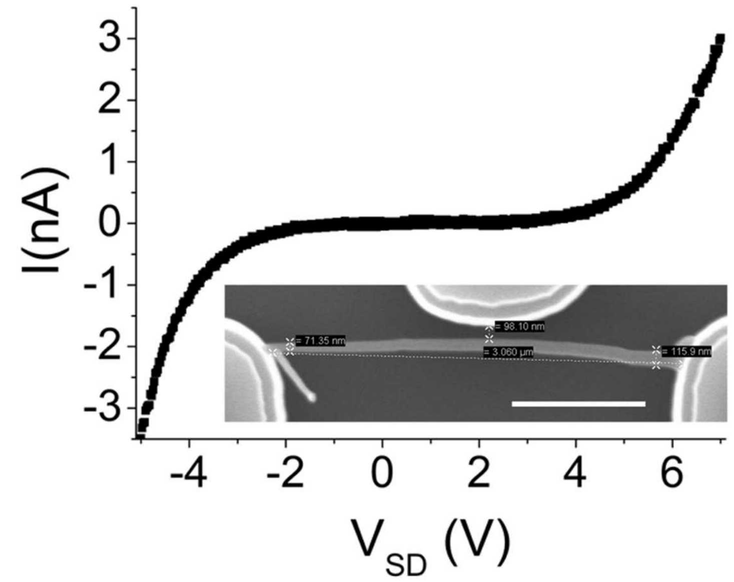

Figure 3.4: Current-voltage response for a single undoped epitaxial bridging Si NW, shown in the inset SEM image (scale bar = 1 μm).

about the as-grown epitaxially bridging Si NWs. The NW is not intentionally doped, and thus the resistance is very high. Fitting the linear region yields a resistance of about 500 MΩ, resulting in a resistivity of approximately 140 Ω-cm. Assuming bulk electron mobility [108], this implies a free carrier concentration of $\sim$1 x 10^{14} cm^{-3}. Furthermore, the NW shows very strong rectifying behavior due to the potential barrier imposed by the difference between the near-intrinsic Fermi level in the NW and the Fermi level of the highly boron doped contact pads.

The resistance of the as-grown Si NWs is too high for electrically-based mechanical resonance detection. Since neither *in situ* nor *ex situ* boron doping was available at the time the mixing measurements were performed, a $\sim$15 nm Au film was evaporated on a sample with a number of single bridging Si NWs available for resonance measurements. Figure 3.5 shows the amplitude and phase response near 100 MHz for a single Au-metallized nanowire (90 nm diameter, 2.6 μm long) with a resistance of 10 kΩ and a leakage resistance of 200 MΩ due to the presence of some Au surface coverage from the drive electrode to source or drain electrodes. The pressure was above 10^{-5} Torr to eliminate the effect of viscous damping. The sharp valley in the amplitude response is a result of destructive interference with the mixing signal, while the large phase shift is characteristic of resonance behavior. The resonant frequency obtained by Lorentzian fitting is 107.2 ± 0.1 MHz. A COMSOL simulation of the the expected in-plane mode for the NW structure yields an eigenfrequency

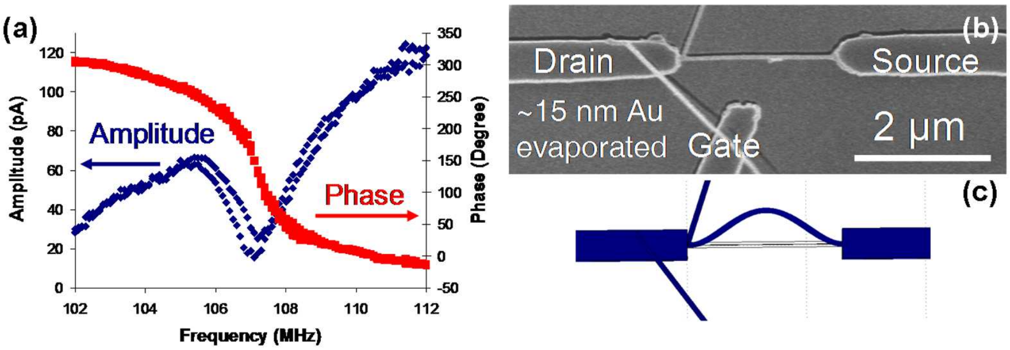

Figure 3.5: Mixing measurement response near 100 MHz for a single Au-metallized epitaxially bridging Si NW. (a) Measured current and phase that indicate possible resonant behavior. (b) SEM image of the Si NW under test. (c) COMSOL simulation mode shape for the first in-plane eigenmode using a close approximation of the actual test geometry.

of 107 ± 9 MHz, in excellent agreement with the measured value (The effect of the Au film on the elastic modulus is neglected in the simulation, but added into the error estimate). It is also notable that the quality factor is only 67, an exceedingly small value, especially in comparison with recent measurements of mechanical resonance in other epitaxially bridging Si NWs [12, 109]. However, enhanced thermoelastic damping arising from the evaporated Au film can significantly degrade the quality factor of nanomechanical resonators at ambient temperatures [110]. A number of electrical resonances were also detected for these SOI samples, and it is difficult to confirm that this resonance peak is mechanical rather than electrical in nature. Localized Pt deposition as part of further measurements eliminated the apparent resonance signal altogether.

3.2 Block Copolymer Templating of Catalyst Nanoparticles

An ideal approach to epitaxial NW device integration by controlled deposition of the NW growth catalyst seeds would achieve the substrate selectivity and particle size control demonstrated previously by Gao *et al* while maintaining lower, well-regulated particle areal densities. At around the same time that Gao *et al* demonstrated Au NP seeding for Si NW growth by galvanic displacement from water-in-oil microemulsions, Aizawa and Buriak showed that diblock copolymer micelles may be used to template galvanic displacement for the deposition of various size-controlled noble metal NPs on Si, Ge, InP and GaAs [111, 112]. The high areal densities of these metal NPs may only be viable for the growth of dense NW arrays. However, an intriguing aspect to surface patterning with block copolymer micellar templates is the fact that the micelles are often trapped in a non-equilibrium state; they are then amenable to density modulation by the addition of inert micelles [113], empty micelles, or homopolymers [114].

In this section a general strategy for the epitaxial integration of semiconductor NWs based on the controlled deposition of catalyst NPs via galvanic displacement through micellar diblock copolymer templates is demonstrated. The chemically rate-controlled Au deposition affords direct control over catalyst NP size, while the addition of polystyrene homopolymer enables rational reduction of NP areal densities. The mean diameters of epitaxial Si nanowires follow the mean sizes of the as-deposited NPs from which they are grown well. Using dip coating, this templating route may be applied to both planar and microtrench substrates patterned with SiO_2 windows where Au NPs can be deposited selectively. Single Si NWs with diameters of approximately $\sim$50 nm may be grown in windows $>$ 600 nm in diameter, indicative of a one order of magnitude reduction in feature size. Low density Si NW growth across trenches on SOI substrates is achieved, enabling electrical measurements of single or few-numbered epitaxially bridging Si NWs (the electrical measurements are described in the next section).

A schematic for the micellar templating strategy is presented in Fig. 3.6. The block copolymer used was polystyrene-block-poly(2-vinylpyridine) (PS-P2VP; M_n = 46 kg/mol, M_w/M_n = 1.18). In bulk form, the P2VP volume fraction (ϕ_{P2VP}) should be composed of cylindrical P2VP domains in a PS matrix; when dissolved in toluene (5 mg/mL) and heated to 70 °C ($>$ 10 min.) the more preferential interactions between toluene and polystyrene result in the formation of spherical micelles with P2VP cores and PS coronas (Fig. 3.6(a)) that are preserved when the solution is cooled to room temperature. This micellar suspension is then mixed with a solution of PS homopolymer (M_n = 6 kg/mol, M_w/M_n = 1.5) in toluene at the same mass concentration to obtain a new mixture with a mass ratio of PS homopolymer to block copolymer that is equivalent to the volume ratio of the two mixtures (Fig. 3.6(b)). Both polymers were obtained from Megan Lane Hoarfrost, a graduate student in Prof. Rachel Segalman's laboratory, with permission from Prof. Segalman. All mixtures were stored under refrigeration, but allowed to warm to room temperature before use, and could be reused repeatedly over the course of months.

Micellar template films are applied to cleaned substrates by either spin- or dip-coating. Before use the liquid mixture was stirred using a magnetic stir-bar for at least 30 min. No HF pre-treatment was performed prior to block copolymer templating or galvanic displacement. For spin coating, 15 μL of a polymer mixture was placed on a sample, which was then spin-coated in air at 4000 rpm. Dip-coating was accomplished by pulling the sample out of the polymer mixture at a rate of 80 - 90 mm/min. After the sample is visibly dry, templated samples are immersed for variable times in a Au plating solution made by adding 100 μL of a 10 mM aqueous solution of potassium tetrachloroaurate ($KAuCl_4$) along with 10 μL of 48-50% (w/w) hydrofluoric acid (HF) to 10 mL of DI water. During this step Au is deposited via galvanic displacement only through the P2VP cores that give aqueous solutions access to the underlying Si surface, as depicted in Fig. 3.6(c). The PS homopolymer acts as

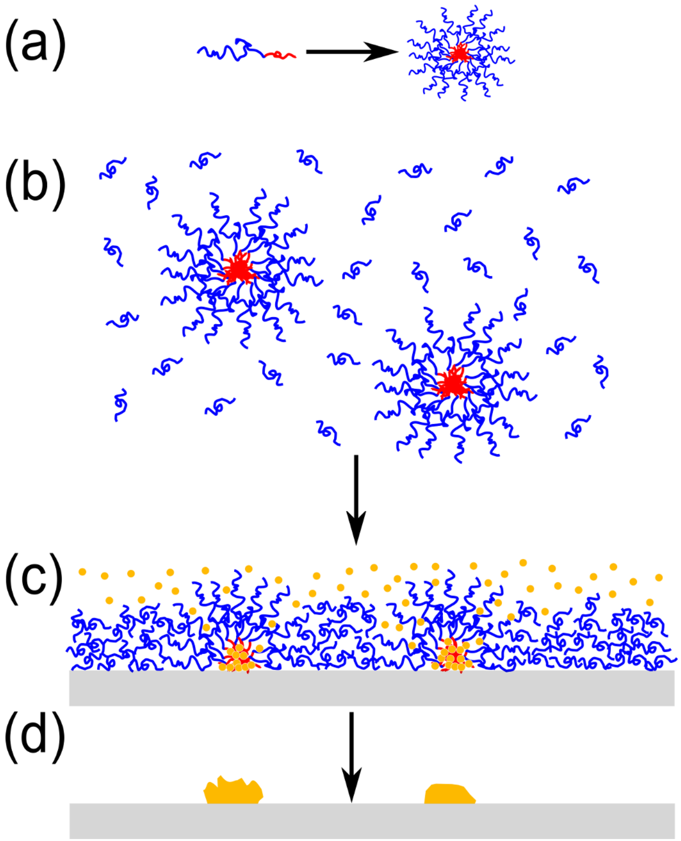

Figure 3.6: Block copolymer templating scheme. (a) Micellization of PS-P2VP occurs in toluene above room temperature, with P2VP cores (red) and PS coronas (blue). (b) After being cooled to room temperature, the micelle suspension is mixed with a solution of PS in toluene having the same mass concentration in the desired mass proportion. (c) The micelle template is applied to a semiconductor surface by spin- or dip-coating, where the PS serves as a spacer between micelles. The sample is then exposed to the aqueous galvanic displacement bath, where the P2VP micelle cores allow selective access to the surface for metal deposition. (d) The polymer template is removed, leaving an array of metal NPs.

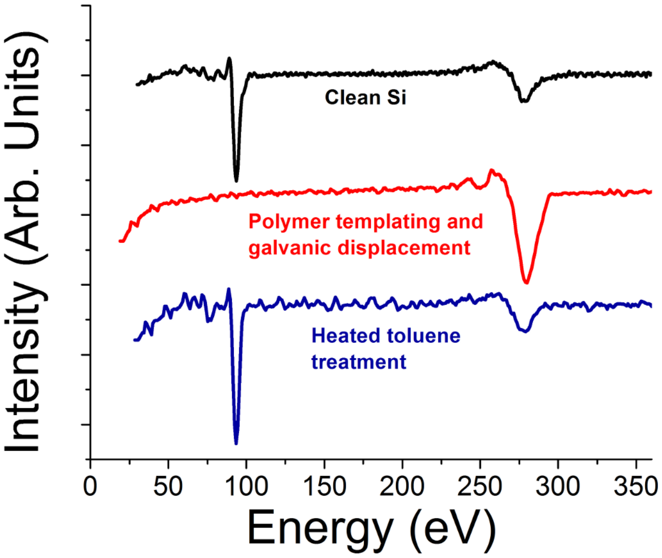

Figure 3.7: Auger electron spectra collected from samples at various stages in the NP deposition process. The block copolymer template had no added PS and the galvanic displacement was for 10 min. Heated toluene treatment involves temperatures $>$ 70 °C for more than 10 min. followed by sonication for more than 10 min.

a spacer on the surface, decreasing the surface areal density of the micelles. Finally, the polymer is removed through immersion in heated neat toluene ($>$ 70°C) for at least 10 min. Unpatterned samples were then sonicated in the same solution for 10 minutes. In patterned samples sonication sometimes resulted in a significant loss in the number of Au nanoparticles (NPs) and so it was not always done. Auger electron spectra confirm the removal of most of the polymer film with sonication in heated toluene, as shown in Fig. 3.7. Si NWs were grown from Au seed NPs at 835 °C for 5-10 min. (bubbler flow/direct flow = 10/100).

The results of this templating approach (by spin coating) with no PS homopolymer added are displayed in Fig. 3.8. Figure 3.8(a) shows a scanning electron microscope (SEM) image of the initial polymer template, while Fig. 3.8(b) and (c) show SEM images after 10 minutes of galvanic displacement and subsequent polymer removal, respectively. There are fewer particles ($\sim$40 – 50 μm^{-2}) after galvanic displacement than there are apparent micelles ($>$ 60 μm^{-2}), though the final number of particles after polymer removal is approximately the same after galvanic displacement. The imperfect formation of particles from the micellar template may be attributed to the presence of a PS homopolymer layer directly above (or underneath) particular micelles that prevent direct access of the aqueous solution from the substrate. The Au region of a X-ray photoelectron spectrum (Fig. 3.8(d)) taken from the sample shown in Fig. 3.8(c) indicates that the deposited material is indeed elemental Au.

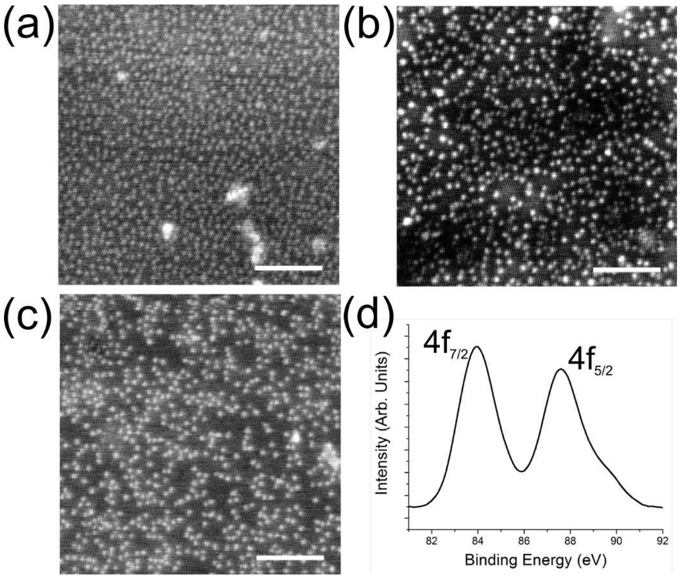

Figure 3.8: Results of the templating process with no added PS. SEM images of (a) the initial micellar template, (b) after 10 min. Au galvanic displacement, and (c) after polymer removal. Scale bar = 1 μm for all images. (d) Au region of the XPS spectrum from the sample shown in (c).

The small hump at ∼90 eV is from the Si substrate itself.

A primary reason for using block-copolymer micellar templating is the capability to tune the particle areal density over a wide range. Here this is accomplished by adding PS homopolymer, the results of which are summarized by the plot of particle areal density *versus* homopolymer/block-copolymer mass ratio in the mixture given in Fig. 3.9. Undiluted block copolymer results in particle areal densities of ∼46 μm^{-2} and ∼42 μm^{-2} for templates applied by spin- and dip-coating, respectively. On the other hand, particle areal densities less than 2 μm^{-2} are readily obtained for mass ratios greater than 20 to 1. Since the areal density (ρ_a) is proportional to L^{-2}, where L is the domain size, areal density reduction is possible by simply using higher molecular weight block copolymers. In the case of PS-P2VP which may be considered amphiphilic, or at least strongly segregated (at the molecular weight used in this report or above), L may be expected to scale with the degree of polymerization N as $L \propto N^{2/3-1}$ [115]. As a result, polymers used to achieve this reduction in ρ_a must possess molecular weights at least ∼5-10 times larger and the scaling of micelle center-to-center distance with degree of polymerization for metallic NPs deposited through PS-P2VP micellar templates in the previous work by Aizawa and Buriak corresponds more closely to the strongly segregated limit (i.e. requiring molecular weights at least 10 times larger) [112]. On the other hand, as demonstrated here extensive areal density tuning may be achieved in a

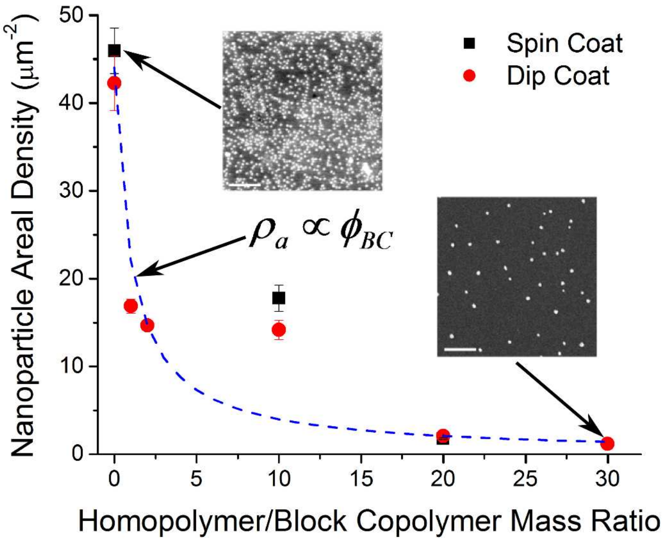

Figure 3.9: NP areal density as a function of the homopolymer/block copolymer mass ratio (PS:PS-P2VP) for both spin- and dip-coating. Upper left inset: SEM image of a spin-coated sample with no added PS after 10 min. galvanic displacement and polymer removal (scale bar = 1 μm). Lower right inset: SEM image of a dip-coated sample with a 30:1 PS:PS-P2VP ratio after 1 min. galvanic displacement and polymer removal (scale bar = 1 μm).

rational way through the mixture of only a single block copolymer and a single homopolymer. If one assumes that the volume fractions of block copolymer and homopolymer in the thin film micellar template are approximately identical with their volume fractions in the toluene mixture, then the areal density of NPs may be considered directly proportional to the block copolymer volume fraction, ϕ_{BC}. This proportionality is represented by a dashed blue line in Fig. 3.9. This simple model provides a fair guide for expected NP areal densities, though there is a noticeable discrepancy at a mass ratio of 10. This may be a consequence of the polymer deposition method (by spin- or dip-coating) since no further steps that are commonly used in block copolymer template processing like thermal or solvent annealing have been applied. It may also be due to higher NP deposition in the micellar template (i.e. less substrate blocking by added PS).

Various proposed applications for epitaxially VLS-grown semiconductor NWs demand that their diameters be precisely controlled. Since VLS-grown NW diameters are determined primarily by the size of the metal NP used as a catalyst, this is the most critical parameter to control. In the method proposed here, catalyst NP size is regulated by the galvanic deposition rate (encompassing chemical kinetic and mass transport factors) and the time of deposition. In order to link NP size with NW diameter, both were measured from the same sample before and after growth, and in order to minimize particle agglomeration due to the high mobility of Au on Si at the elevated temperatures of our growth reactor (> 800 °C) [84, 116, 87] that would strongly affect the nanowire diameter distribution, we used samples with low areal densities ($< 2\ \mu\text{m}^{-2}$). Atomic force microscopy (AFM) measurements were performed in air with a Digital Instruments Nanoscope IIIa system in tapping mode. Mean NP volumes were determined by flooding analysis using WSxM Scanning Probe Microscopy Software [117], and the error bars represent the standard error in the mean NP volume over several images. For aesthetic presentation, Gwyddion scanning probe microscopy software was used to create topographic images. Figure 3.10(a) and (b) show AFM topography images of Au NPs on Si deposited through the method described in this report for immersion times of 1 min. and 10 min., respectively, and Fig. 3.10 (c) and (d) show SEM images of the resulting Si NWs grown from the samples in (a) and (b), demonstrating the clear increase in mean diameter for NWs grown from the larger particles. If one assumes that the Au droplet on top of the NW is approximately hemispherical and the NW radius is nearly equivalent to the droplet radius, then the NW diameter is expected to be proportional to the cube root of the Au NP volume from which it is grown. The exact proportionality is determined by the eutectic droplet contact angle on Si and the equilibrium Si mole fraction in the droplet at the growth temperature, as well as the Si supersaturation during growth and the ellipticity of the droplet. The portion of the Au NPs recessed in the Si substrate is not considered, though this is offset to some extent by the convolution of tip size with the NP size measurement. Therefore, focus is placed upon the proportional scaling between NW diameter with Au NP size as determined by immersion time. Figure 3.10(e) shows the cube root of the mean Au NP volume as well as the mean NW diameter *versus* immersion time. Both increase monotonically with increasing immersion time, with a much faster growth rate characterizing the initial NP nucleation stage ($< \sim$1 min.). For times above one minute the mean NW diameters scale directly with the NP size, as expected. A larger difference between the mean NW diameter and the cube root of the NP volume is seen for the 30 s sample. In this case, NWs grow much more slowly or not at all from smaller Au clusters, a fact that is commonly attributed to the Gibbs-Thomson effect [63]. The overall NW density is then reduced and the mean NW diameter is skewed to a higher value than expected based on the geometric argument given above. Similar Au NP growth behavior is observed for higher areal density micellar templates, though the overall NP growth rate is reduced as shown in Fig. 3.11, which may be attributed to increased competition for reactant.

A significant advantage to galvanic displacement is its substrate selectivity, which permits highly controlled conformal metal deposition in patterns without additional lift off steps. Therefore, block-copolymer micelle templates (PS:PS-P2VP ratio = 10:1) were applied to Si(111) substrates with a ∼ 400 nm thick patterned silicon oxide hard mask (obtained from collaborators Marta Fernandez and Alvaro San Paulo) by dip coating, and Au NPs were deposited *via* galvanic displacement for 1 min. The selective deposition of Au NPs means that Si NWs can only be grown in the wells exposing the Si substrate, as shown in Fig. 3.12(a) and (b). Critically, in Fig. 3.12(b) it is demonstrated that individual NWs less than ∼50 nm in diameter may be grown in wells larger than 600 nm in diameter, achieving a

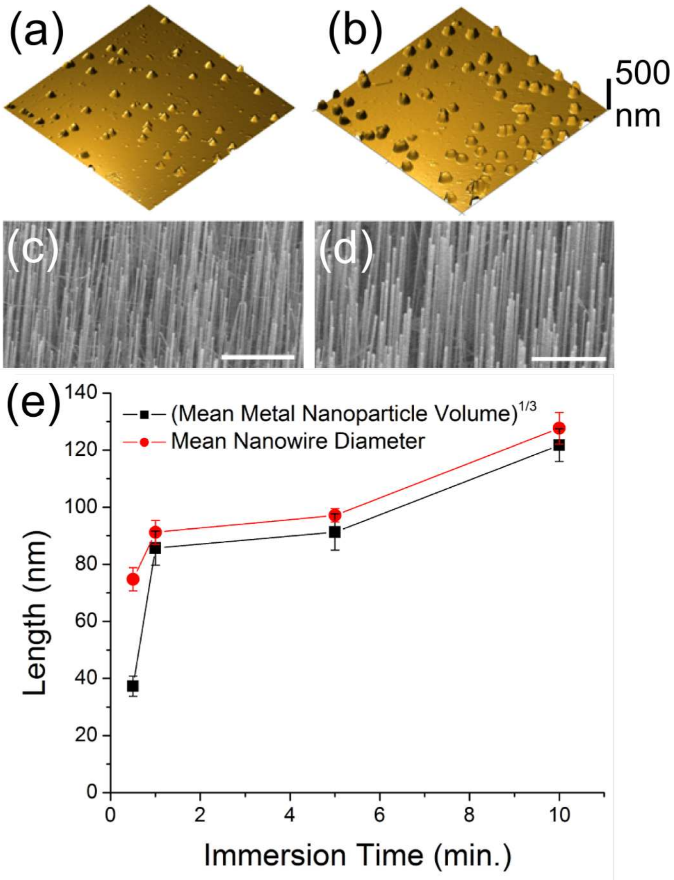

Figure 3.10: Control over NP size by immersion time. (a-b) AFM topography images of Au NPs deposited on Si(111) by galvanic displacement through ∼2 μm^{-2} micellar templates for (a) 1 min. and (b) 10 min. The squares are both 5 μm x 5 μm and the vertical scale is the same for both images. (c-d) Si NWs epitaxially grown from the Au NPs shown in (a) and (b), respectively. The scale bars are 5 μm in both images. (e) Cubic root of the mean NP volume and mean diameters of Si NWs grown from these particles *versus* immersion time in the aqueous galvanic displacement solution. For 1 min. and above the NW diameters and NP volume cube roots scale with each other, while for less than 1 min. NW nucleation barriers skew the measured mean NW diameter to a higher value. Connecting Lines are guides to the eye.

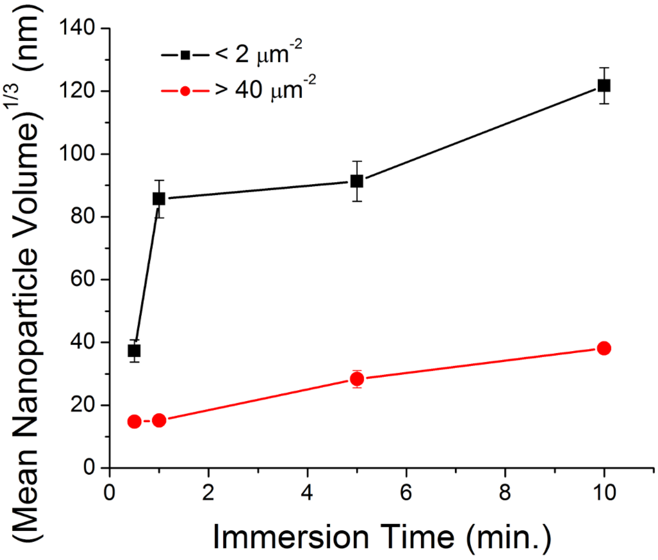

Figure 3.11: Au NP cube root versus immersion time in the galvanic displacement Au plating solution at micelle surface areal densities $> 40\ \mu\text{m}^{-2}$ (red) and $< 2\ \mu\text{m}^{-2}$ (black).

reduction in feature size greater than an order of magnitude with the same approximate pattern registry. For uniform coverage of the micellar template, the number of NPs in a well will be proportional to the well area, which is consistent with experimental data shown in Fig. 3.12(c).

The conformality of galvanic displacement suggests that this templating technique may also be applied to appropriately patterned substrates with trenches having the correct orientation of sidewalls (Si(111) for the Au/Si NW growth system studied here) for the fabrication of devices based on in-plane epitaxial NWs. Primary focus is placed on NWs grown from the 30:1 template ($\rho_a < 2\ \mu\text{m}^{-2}$) since this is the most likely template to enable the fabrication of devices based on single or few NWs using only micron-scale lithography. Au NPs were deposited using a 1 min. immersion time in the Au deposition bath. Figure 3.13(a) shows Si NWs grown in a $\sim 2\ \mu\text{m}^{-2}$ wide trench to epitaxially bridge two electrically isolated single-crystal Si electrodes on a buried silicon oxide layer. The top of the electrodes were also covered with silicon oxide, preventing Au cluster deposition on the top surface as well. More selective growth of Si NWs is achieved if the trench sidewalls are also covered with an oxide mask and a second lithography step is used to define micron-scale windows of exposed Si, as for example in Fig. 3.13(b). In this case a single Si NW epitaxially bridges the two highly-doped single-crystal Si electrodes near a third electrode that may be used for further device fabrication if desired (the capacitive coupling with the NW is too small to yield any gate dependent response in the current configuration). Two-point current-voltage measure-

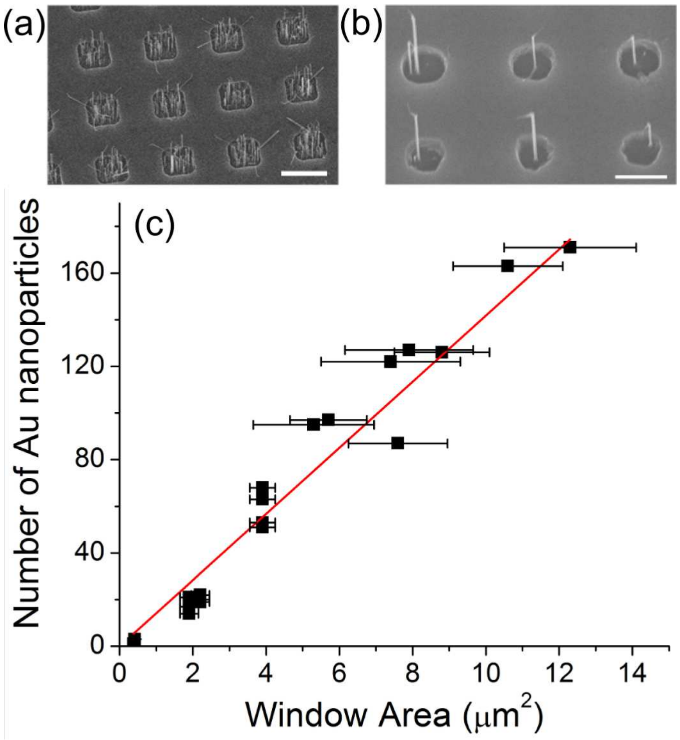

Figure 3.12: Block copolymer templating and Si NW growth on Si(111) samples with patterned wells in a SiO_2 hard mask. The PS:PS-P2VP mass ratio is 10:1. (a) Si NWs grown in $\sim 12\ \mu m^{-2}$ wells (scale bar = 5 μm). (b) Si NWs grown in circular wells 600-700 nm in diameter (scale bar = 1 μm). (c) Number of Au NPs per well area. The solid lines represents expected values based on measurements of areal densities on unpatterned samples.

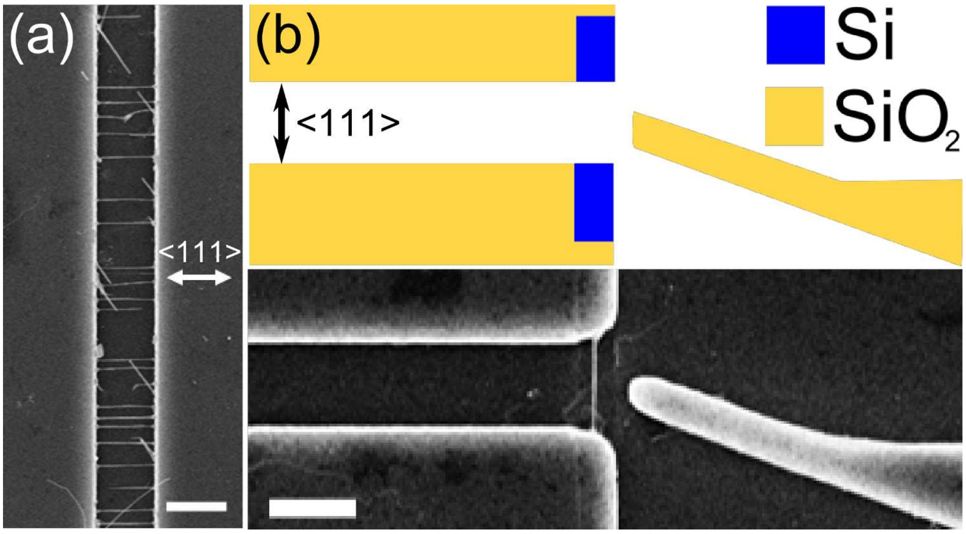

Figure 3.13: Epitaxial Si NW growth from templated Au NP seeds ($\rho_a < 2\ \mu\mathrm{m}^{-2}$) on silicon-on-insulator trench sidewalls. (a) SEM image of Si NWs grown in a 2 μm wide trench (scale bar = 2 μm) (b) SEM image (bottom) of a single Si NW grown in a photolithographically defined Si window depicted in the top schematic diagram (scale bar = 2 μm).

ments on various single-NW or few-numbered Si NW device structures produced through this templating methods after *ex situ* boron doping are presented in the next section.

Since the micellar template is disordered, the registry for particle deposition with the larger photolithographic pattern is statistical and thus imperfect; hexagonal ordering might significantly improve upon this. Using polymers with more uniform chain lengths would likely enhance the hexagonal packing to a small degree. Thermal annealing was avoided since the micellar template is a trapped morphology that is not favored in thin film or bulk phases and would likely transfer to an in-plane cylindrical morphology (for the given P2VP volume fraction in the PS-P2VP) if thermally annealed [118]. On the other hand, solvent annealing typically induces non-equilibrium morphologies and has been shown to improve hexagonal ordering of spherical micelles [119, 120]. It may be possible to apply solvent annealing to block-copolymer micelle/homopolymer systems like the one described here, though I am not aware of any preceding work on solvent annealing of block copolymer micelles with low areal densities or homopolymer molecular spacers. Besides micelles, equilibrated block copolymer thin films may exhibit excellent ordering and uniformity with the help of chemical epitaxy [121] or graphoepitaxy [122], though significant effort has been focused on pattern density multiplication [121, 122], opposing the effort of this work. Nevertheless, Stuen *et al* have recently shown that the domain spacing of polystyrene-block-poly(methyl methacrylate) (PS-PMMA) block copolymer templates consisting of perpendicular cylindrical minority domains (PMMA) may be adjusted by nearly a factor of 3 by PS homopolymer addition, though a substantial reduction in domain size uniformity was observed and the pattern areal densities were still well above 100 μm^{-2} (assuming hexagonal packing) [123]. Papalia *et al* have also recently demonstrated areal density tuning of spherical minority polyisoprene domains in polystyrene-block-polyisoprene (PS-PI) over a very broad range by the addition of PS homopolymer and controlled film thickness, though hexagonal ordering was not apparent and the minimal areal density reported was $> \sim 20$ μm^{-2} [124]. In any case, the evolving developments in ordering block copolymer thin film or micellar templates may potentially be leveraged with galvanic displacement for the epitaxial integration of NW devices via precise substrate and pattern registry in various geometries.

3.3 *Ex Situ* Doping of Silicon Nanowires Using Boron Tribromide

This section is primarily adapted from a publication that appeared in *Nanoscale*: G.S. Doerk, G. Lestari, F. Liu, C. Carraro, and R. Maboudian. *Ex situ* vapor phase boron doping of silicon nanowires using BBr$_3$. *Nanoscale*, 2(7):1165-1170, 2010 - Reproduced by permission of the Royal Society of Chemistry.

Well-controlled doping is crucial to development of promising silicon nanowire-based electronic [28], thermoelectric [24], photovoltaic [33], and nanoelectromechanical [109] devices. *In situ* doping has been the primary means of introducing electrically active impurities into VLS-grown nanowires [125, 126, 127, 128], but is subject to notable limitations. For instance the dopants are often confined to a surface layer, resulting in non-uniform radial and axial dopant distributions [129, 130, 131, 132, 133]. Furthermore, the enhancement in vapor-solid growth that is typical during *in situ* boron doping can lead to tapering [77], sawtooth faceting [93], or even substantial amorphous shell growth [134]. It would also be highly advantageous to develop doping strategies usable with NWs in a variety of geometries, including epitaxial device configurations where the proper integration of NW growth with device fabrication requires extremely well-controlled growth that may not be possible with *in situ* B doping.

This motivates efforts to dope NWs *ex situ*, particularly for the case of boron doping. Ion implantation has been successfully used to dope Si NWs [135, 136] but is an expensive, low-throughput method that may be limited to the geometries in which nanowires are accessible to doping (due to shadowing by other materials). Spin-on-dopants can achieve high active dopant concentrations in horizontal Si NWs [137], but can damage or even remove NWs that are oriented vertically or are bridging two electrodes across a trench. Recently, Ingole *et al* demonstrated an *ex situ* proximity diffusion doping method based on the vapor phase transport of B_2O_3 from a spin-on-dopant film source, followed by its reduction to elemental B (with concomitant Si oxidation) on the Si surface [138]. Boron concentrations in the Si NWs ranged from 10^{18}-10^{20} cm^{-3}, but the necessary Si oxidation limits the minimum diameter of Si NWs that can be doped by this method.

In this section an *ex situ* vapor phase doping method based on the hydrogen reduction of boron tribromide is demonstrated. Axially homogeneous active boron concentrations from 10^{18}-10^{20} cm^{-3} are achieved with minimal effects on the NW morphologies or crystal quality. In addition, the technique can be readily extended to bridging Si NWs at temperatures as low as 700 °C for use in a variety of nanoelectronic or nanoelectromechanical devices, as shown by current-voltage measurements.

Si NWs used in doping experiments were synthesized from galvanically displaced Au films or particles, 50 nm Au colloids, or galvanically displaced Pt as described in the preceding chapter. Before doping, Au-catalyzed Si NWs were immersed in an iodine/potassium iodide (KI) solution (4:1:40 KI:I2:H_2O) for at least 30 min. to selectively etch and remove as much Au as possible. Otherwise Au migrates rapidly along the full length of the NWs at the doping temperatures, with dramatic effects on their surface morphologies and potentially on their electrical properties. After Au etching, the samples were cleaned in a UV ozone cleaner for 15-30 min. In some cases they were then immersed in 10:1 HF for one min., rinsed with DI water, and dried under an N_2 stream. Pt-catalyzed NWs did not undergo iodide etching.

Doping was conducted in the same reactor as for NW growth but with a different quartz tube to prevent the possibility of B contamination during NW growth. The doping process consists of two-stages. In the first "prediffusion" stage, 6 sccm carrier gas was bubbled through liquid BBr_3 held at 0 °C while 270 sccm of carrier gas passed directly to the reactor, at a set temperature between 600 to 800 °C for 1–5 min. The sample could then be removed from the reactor (after cooling down) or left in for the second "drive-in" stage. Drive-in occurred at a controlled temperature between 700 to 850 °C for times ranging from 10 to 60 minutes in Ar gas only.

For Raman spectrometry Si NWs were sonicated off their growth substrates into ethanol and drop cast from suspension onto Si dice covered with an evaporated Au or Ag film, upon which they generally laid flat. Raman spectrometry measurements were performed in backscattering configuration with an excitation line provided by a HeNe laser (632.8 nm wavelength) through an Olympus BX41 100X confocal microscope (numerical aperture = 0.8). The power at the sample was ∼1–2.5 mW as controlled by a density filter for a spot size less than 1 μm. NWs were examined individually to avoid convoluted effects from overlapping spectra of different NWs and were aligned along the laser polarization direction to maximize the intensity of the Raman spectra due to the large polarization anisotropy arising from the NW/air dielectric mismatch (discussed in the next chapter). Raman maps were obtained using a high-resolution piezoelectric stage.

For electrical measurements, NWs were drop cast from suspension in ethanol onto Si chips covered with 510 nm of chemical vapor deposited silicon oxide and 110 nm silicon nitride with metal electrodes patterned by photolithography on top. Contacts to individual NWs were defined by electron beam lithography on a JEOL 6400 SEM and Nanometer Pattern Generation System (NPGS). The pattern was written in poly(methyl methacrylate) (PMMA) and developed in a solution of 3:1 isopropanol:methyl isobutyl ketone (MIBK). Native oxide was then removed from the NW surfaces by immersing the samples in 10:1 HF for more than

10 s. Immediately afterwards the samples were loaded into a high-vacuum Thermionics VE 100 electron beam evaporator and Ti/Au (100 nm/100 nm) was deposited. No annealing step was performed after pattern lift-off. Electrical measurements were performed in air using either a probe station with a HP4145B Semiconductor Parameter Analyzer or a Signatone S-1160 probe station with a Keithley 2400 Sourcemeter controlled by Keithley Labtracer 2.0 software.

The fabrication of trenched SOI device substrates for epitaxial bridging Si NW growth was described earlier in this chapter. Before electrical testing (but after doping) the samples were immersed in 10:1 HF for 10 min., rinsed with DI H_2O and dried under a N_2 stream to remove the silicon oxide hard mask. Alternatively, other samples were exposed to vapor HF treatment at a temperature of 45 °C for 5 min.

For doping Si, boron is frequently deposited on Si surfaces in the form of B_2O_3. This is reduced on the Si surface by the oxidation of the Si, resulting in a B rich SiO_x layer. The elemental boron is then diffused into the Si and activated (incorporated into a substitutional site) during a high temperature drive-in anneal. For nanoscale Si structures, this may have limited use due to need to oxidize (and consume) part of the silicon. On the other hand, B may be deposited directly in elemental form by reduction in H_2 according to the following net reaction [139]:

$$\mathrm{BBr_3} + 3/2\ \mathrm{H_2} \longrightarrow \mathrm{B} + 3\mathrm{HBr} \tag{3.3}$$

However, care must be taken since HBr, much like HCl, can etch Si at elevated temperatures [140].

To determine the general efficacy of this doping method four-point probe measurements were performed using a Signatone four-point probe apparatus on flat Si(100) samples with initially high sheet resistance after 1 min. prediffusions at various temperatures (Fig. 3.14) . A steady drop by nearly two orders of magnitude is found in sheet resistance from 180 ± 91 kΩ/□ for the undoped sample to 2.6 ± 0.3 kΩ/□ for the sample prediffused at 800 °C. In this stage a large dose is introduced into the Si in a thin layer but most of it remains inactive. To drive-in the boron, each sample was covered with 50 nm evaporated SiO_x (to prevent contamination or the introduction of more boron) and annealed in Ar at 850 °C for 30 min. After this the sheet resistance was substantially reduced. The sheet resistance difference among the samples was also reduced, with a range of only 2.0 ± 0.2 kΩ/□ for the sample prediffused at 600 °C to 0.66 ± 0.15 kΩ/□ for the sample prediffused at 800 °C.

Given that the junction depth is likely dominated by the drive-in step, this indicates the active boron concentration only varies by approximately a factor of 3 or less across the prediffusion temperature range, suggesting that the process is generally insensitive to prediffusion temperature. Nonetheless, the low doping temperatures used in this process are valuable for minimizing thermal budget in device fabrication. No change in sheet resistance from the undoped samples was measured for prediffusion temperatures below 600 °C for the conditions used in this study. Conditions are expected to be very different for NWs which have high surface to volume ratios and cylindrical geometries with diameters smaller

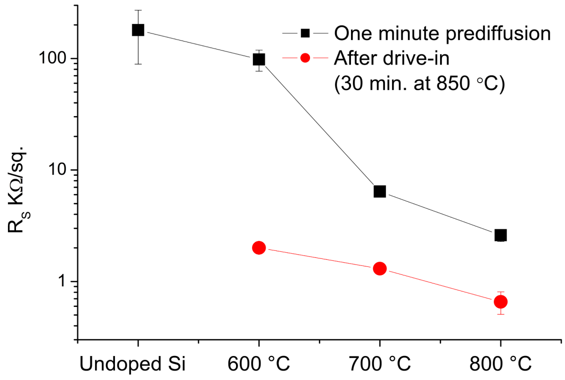

Figure 3.14: Sheet resistance measurements for flat bulk Si samples after one minute prediffusions for various temperatures, followed by 30 minute drive-ins at 850 °C. The samples were covered with ~50nm evaporated SiO_x before drive-in.

than expected junction depths. Furthermore, when translated to doping NWs, the efficiency of this process is expected to be strongly impacted by their areal density due to reactant depletion effects.

Raman spectrometry provides a rapid, quantitative and non-destructive method to measure the active B concentrations in Si with sub-micron resolution [129, 141]. It was therefore employed to probe the capability to dope Si NWs by this process. Interference between discrete phonon Raman scattering and continuous electronic Raman scattering from intravalence band hole transitions gives rise to a Fano resonance in the Raman spectra for Si around the characteristic optical phonon frequency [142]. Quantitative doping information can be extracted by fitting the spectra with Fano line shapes:

$$I(\omega) = A\frac{(q+\varepsilon)^2}{(1+\varepsilon^2)} \tag{3.4}$$

where

$$\varepsilon \equiv \frac{(\omega-\omega_o)}{\Gamma} \tag{3.5}$$

In this equation A is a fitting constant, ω_o is the phonon frequency, Γ is the line width, and q is commonly called the assymetry parameter. Both ω_o and Γ are independent of the excitation line wavelength but are affected by other factors such as sample temperature and stress [143].

The reciprocal of the assymetry parameter, $1/q$, is proportional to the ratio of the Raman tensor for electronic scattering to the Raman tensor for phonon scattering [142] and as a result is also approximately proportional to the free carrier concentration for active boron concentrations in the range of 10^{19} cm^{-3} [144]. The q parameter is also a function of the excitation line wavelength and thus must be calibrated for the laser. However, both ω_o and Γ are functions of the free carrier concentration but not the wavelength. Using the data available in [142], their relationship to active boron concentration was determined and then approximate reference points for the relationship between $1/q$ and the active boron concentration in our doped Si NWs were obtained. A $1/q$ value of 0.09 corresponds to an active B concentration of $\sim$2 x 10^{19} cm^{-3} and a $1/q$ value of 0.5 corresponds to $\sim$1 x 10^{20} cm^{-3}. These values nearly match those of Imamura *et al* who estimated a $1/q$ values of 0.1 and 0.5 for concentrations of $\sim$2 x 10^{19} cm^{-3} and $\sim$1 x 10^{20} cm^{-3} respectively for the same laser wavelength [129, 141].

Figure 3.15(a) shows the Raman spectra for typical Si NWs subjected to different doping conditions. The spectra have been shifted vertically for ease of viewing, and all spectra except that for the undoped Si NW are shown with a corresponding Fano line shape, which clearly fit the data well. For a prediffusion (1 min.) and drive-in (10 min.) temperature as low as 750 °C, the $1/q$ value is 0.079 ± 0.002, indicating that the average active boron concentration in the wire is approximately 1-2 x 10^{19} cm^{-3}. As expected increasing the prediffusion temperature to 800 °C and the drive-in temperature and time to 850 °C and 30 min. respectively can increase the active boron concentration to $\sim$5 x 10^{19} cm^{-3}. The same conditions applied to Si NWs grown from $\sim$50 nm Au colloids (and therefore more spaced apart from those grown from an Au film) gives rise to NWs with Raman spectra characterized by very high $1/q$ values. For example, the top-most spectra is typical for such NWs and exhibits a $1/q$ value of $0.78 \pm .01$, indicating that active boron concentrations greater than 1 x 10^{20} cm^{-3} –approaching, or possibly exceeding the equilibrium solid solubility limit [145, 146] –are attainable. This demonstrates the range of achievable active dopant concentrations and the importance of accounting for areal density in controlling dopant dosing.

A common issue with *in situ* doping is the lack of both axial and radial doping uniformity [129, 131, 132], but it may be possible to control this with ex-situ techniques. Figure 3.15(b) shows $1/q$ values measured for spectra taken 1 μm apart along the axes of three Si NWs with different average $1/q$ values (and hence different average active boron concentrations). The active boron concentration does not deviate much from the average values, marked by red lines that correspond to approximately 7.3 x 10^{19} cm^{-3}, 4.1 x 10^{19} cm^{-3}, and 1.6 x 10^{19} cm^{-3} from highest to lowest. This shows the excellent axial doping uniformity achievable through this *ex situ* doping technique. On the other hand, Raman mapping alone does not provide information about the radial doping profile; however, boron diffusivity may be enhanced by several orders of magnitude when the boron concentration exceeds the intrinsic free carrier concentration [147] – an important effect at low temperatures. Combined with the high surface-to-volume ratio and cylindrical geometry of NWs, along with the fact that *ex situ* methods decouple dopant incorporation from diffusion, we expect that a higher degree of radial uniformity may be achievable through *ex situ* rather than *in situ* doping.

Electron microscopy enables one to examine the structural properties of the NWs doped using BBr_3. Figure 3.16(a) shows a SEM image of undoped Si NWs grown from galvanically displaced Au film, and Fig. 3.16(b) shows Si NWs grown in the same manner after a 5 min.

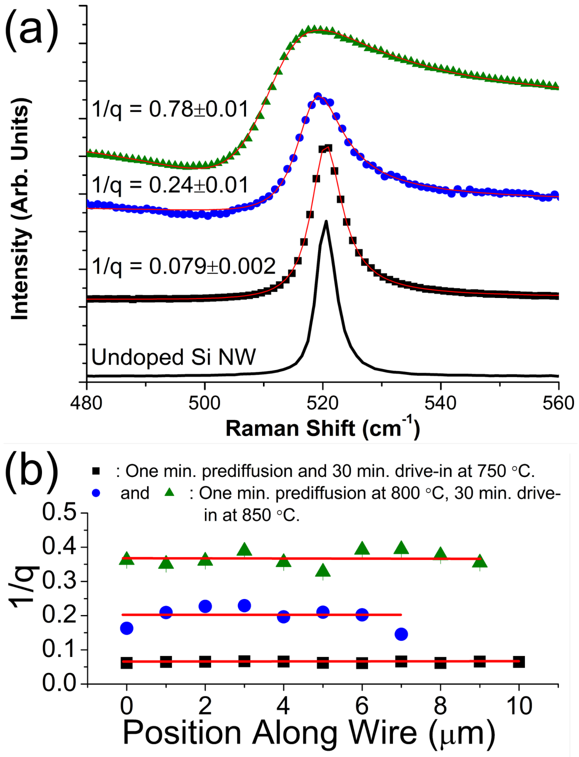

Figure 3.15: (a) Raman spectra for Si NWs subjected to different doping conditions, shifted vertically from each other for ease of viewing. All spectra except the top one (green triangles) correspond to Si NWs grown from galvanically displaced Au films. The doping conditions for each curve are (from bottom to top): Undoped Si NW (black line); One min. prediffusion at 750°C, 10 min. drive-in at 750°C (black squares); One min. prediffusion at 800°C, 30 min. drive-in at 850°C (blue circles); One min. prediffusion at 800°C, 30 min. drive-in at 850°C, NWs grown from 50 nm Au colloids (green triangles). Solid red lines are the fits to a Fano line shape (eqn. 3.4). (b) Fano fit asymmetry ($1/q$) as a function of position along the axes of doped NWs grown from Au films. Doping conditions are included in the figure. The red lines represent approximate mean values for $1/q$, corresponding to active B concentrations of (top to bottom) ~7.3 x 10^{19} cm^{-3}, ~4.1 x 10^{19} cm^{-3}, and ~1.6 x 10^{19} cm^{-3}. The error bars are comparable to symbol size.

prediffusion and 1 hr. drive-in, both at 775 °C. The estimated active boron concentration for these wires is greater than 2 x 10^{19} cm^{-3}. Though there has been some attenuation in the number of NWs (primarily from the iodine pretreatment), these SEM images demonstrate that there is no disernable change in morphology for the majority of doped NWs.

More detailed structural information was obtained through TEM. Figure 3.16(c) shows a representative TEM of an undoped wire viewed along a <110> direction that permits viewing of the {112} NW sidewals edge-on. The NW sidewalls are smooth though occasionally NWs exhibit facets indicative of some Au coverage (we find these facets are much more common in NWs grown from Au colloids), and they are covered with less than ∼5 nm of native oxide. Figure 3.16(d) shows a TEM image of a NW from a sample with NWs doped to approximately ∼5 x 10^{19} cm^{-3}, also viewed along a <110> direction. The surface oxide layer is slightly thicker (typically 5 to 10 nm) on these NWs, possibly due to a small amount of oxidation that occurs during the drive-in stage. Higher magnification TEM images (Fig. 3.16(e) and (f)) of sidewall segments from the above undoped and doped Si NWs, respectively, show that while there are no dramatic morphological changes in the NWs as a result of doping (e.g. tapering or faceting), the process does induce a degree of surface roughening. Analyses of Fig. 3.16(e) and (f) indicate that the doping process induces a root mean squared (RMS) NW sidewall profile roughness of ∼0.4 nm, compared with a RMS roughness value of ∼0.2 nm for the undoped Si NW. Analyses of similar high magnification images of other doped and undoped Si NWs yield similar results. Such roughening may have important implications for decreasing NW thermal conductivities [24] and/or electrical mobility (especially at diameters <∼10 nm) [148]. This may benefit the employment of Si NWs in thermoelectric devices but may hinder the aggressive scaling of Si NW-based electronics. Fourier transforms of Fig. 3.16(e) and (f) shown in the inset of each image demonstrate that the wires retain the excellent quality needed for a variety of device applications.

Two-point electrical measurements were performed to confirm the conductivity enhancement afforded by this doping process. Figure 3.17 shows characteristic current-voltage curves for an undoped Pt-catalyzed Si NW and a Pt-catalyzed Si NW from a sample that underwent a 5 min. prediffusion followed by a 30 min. drive-in, both at 750 °C. The undoped wire (diameter ≈ 120 nm) exhibits rectifying contacts and a resistivity of 120 Ω–cm (measured from 4.5 - 5.0 V). Assuming bulk Si hole mobility [108], its free carrier concentration is estimated at ∼1 x 10^{14} cm^{-3}. On the other hand, the doped wire (diameter ≈ 50 nm) exhibits ohmic contacts and an apparent resistivity of 0.046 Ω–cm (resistance = 1 MΩ), which provides an estimated active B concentration of ∼8 x 10^{17} cm^{-3}, again assuming bulk Si hole mobility [108]. Fano fitting of other NWs from the same sample imply an average estimated active boron concentration between ∼6 x 10^{18} cm^{-3} and ∼1 x 10^{19} cm^{-3}, though this is at the lower detection limit for this technique. This range of concentrations suggests that the NW resistivity should be approximately one order of magnitude lower. However, factors such as surface oxide thickness (unmeasured by SEM imaging), size dependent mobilities, surface interface states [9], catalyst contamination [72], dopant deactivation [10] and contact resistances can substantially increase resistivity in silicon nanowires beyond that expected

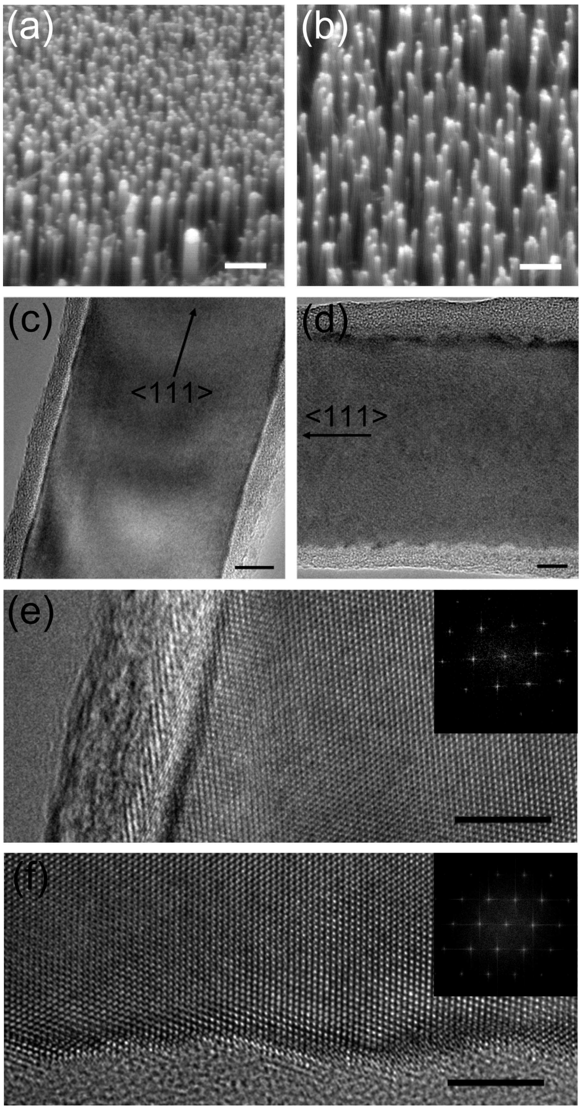

Figure 3.16: Electron microscope images of doped and undoped Si NWs. (a) SEM image of undoped Si NWs (scale bar = 2μm). (b) SEM image of Si NWs doped through a 1 min. prediffusion and a 1 hr. drive-in, both at 775 °C (scale bar = 2 μm). (c) TEM image of an undoped Si NW (Scale bar = 10 nm).(d) TEM image of a Si NW doped through a 1 min. prediffusion at 800 °C and a 30 min. drive-in at 850 °C, with an expected active boron concentration of ~5 x 10^{19} cm^{-3} (scale bar = 10 nm). (e-f) High magnification TEM images of sidewall segments for the undoped NW in (c) and the doped NW in (d), respectively. The scale bar is 5 nm for both images. The inset Fourier transforms in (e) and (f) indicate that each of these wires possesses a <111> growth direction, and that a high quality single crystal is retained through the doping process.

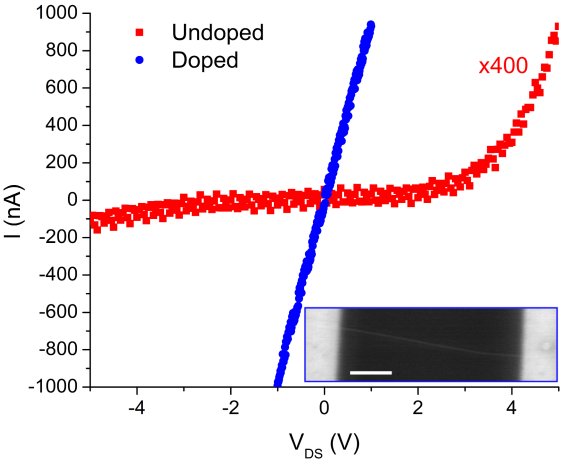

Figure 3.17: Current-voltage curves for an undoped Pt-catalyzed Si NW (red) and a Pt-catalyzed Si NW doped through a 5 min. prediffusion followed by a 30 min. drive-in at 750 °C (blue). Inset: SEM image of the doped Si NW whose data is shown (scale bar = 1 μm).

from the intentional impurity concentration alone. Indeed, higher-than-expected four point resistivities have been measured for Si NWs B-doped *in situ* [126] or *ex situ* [138], attributed in part to the reasons highlighted above (except contact resistance).

This *ex situ* doping method was also used on the SOI sample with epitaxially bridging Si NWs shown in Fig. 3.13 to obtain an active dopant concentration above 10^{19} cm^{-3} using a 1 min. prediffusion and a 60 min. drive-in, both at 700 °C (no HF treatment was performed after iodide Au etching). Two-point current voltage measurements were then performed on various single-NW or few-numbered NW device structures. Since a number of electrodes are interconnected by epitaxially bridging Si NWs, and these in turn occasionally bridge to a third "gate" electrode nearby, a small degree of leakage current was observed in some measurements. We corrected for this by measuring not just the resistance across the NWs under test ("source to drain", R$_{SD}$) but also through the other connected conduction paths ("source to gate", R$_{SG}$, and "gate to drain", R$_{GD}$). The actual NW resistance (R$_{NWs}$) is obtained by the following equation:

$$R_{NWs} = \frac{R_{SD}\left(R_{SG} + R_{GD}\right)}{R_{SG} + R_{GD} - R_{SD}} \qquad (3.6)$$

The measurements of R$_{SG}$ and R$_{GD}$ most likely underestimate their true values due to the parallel conduction path through the wire; therefore this measurement may overestimate the NW resistance. The maximum negative error is included in Figure 3.18(b); however, a large potential barrier to electrical conduction by the leakage paths makes this negative error small in most cases for the voltage range over which resistance is measured (-1 V to 1

V).

Figure 3.18(a) depicts the measured current-voltage curve for the single Si NW in Fig. 3.13(b) evidencing an ohmic response that was typical of these device structures. The two-point current-voltage responses for 11 such structures on the same die were measured. The high doping level minimizes the surface carrier depletion width so that it may be assumed that the full NW diameters are involved in electronic conduction. For a given two point measurement, the NWs which conduct current may possess different diameters (D_i), but are all approximately the same length (L). In addition, if it is assumed that the electrode and probe tip resistances are negligible, and that the doping is uniform across the substrate, the resistance of N NWs (R_{NWs}; $N = 1 - 5$) is given by:

$$R_{NWs} = 2R_C + \rho \left(\frac{4L}{\pi \sum_i^N D_i^2} \right) \tag{3.7}$$

where R_C is the contact resistance and ρ is the resistivity of the NWs. Plotting measured resistance *versus* the size parameter contained in parentheses in equation (3.7) (Fig. 3.18(b)), a resistivity value of 10 ± 5 mΩ-cm and an average contact resistance of 7 ± 3 kΩ are derived. Based on the average cross sectional area of bridging NW device structures, the estimated specific contact resistance is (1.0 ± 0.5) x 10^{-6} Ω-cm^2. This value is superior to specific contact resistances reported for Si NWs using deposited metal films [149, 150], and is comparable or lower than previous values for epitaxial NW contacts [43, 151], though NiSi contacts to Si NWs have been shown to exhibit lower values [152]. These results demonstrate the promise of combining block copolymer micelle templated galvanic displacement for the seeding of VLS-grown NWs with *ex situ* boron doping for epitaxial NW device integration.

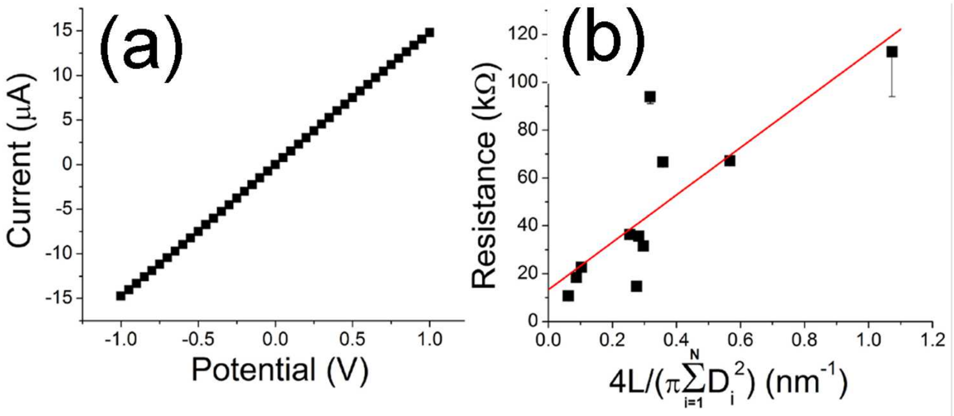

Figure 3.18: (a) Current-voltage response for the Si NW shown in Fig. 3.13(b) after *ex situ* boron doping. (b) Resistance *versus* the physical scaling parameter inside parentheses in eqn. (3.7) for 11 single Si NW or few-NW epitaxially bridging device structures on the same sample. The red line is a linear fit to the data.

Chapter 4

Thermal Measurements of Individual Nanowires Using Raman Spectrometry

This chapter begins with a discussion of the details of Raman spectroscopy germane to NW samples and a description of how temperature affects Raman spectra. This is followed by a description of precision measurements of the temperature dependence of Raman spectra for individual Si NWs and the demonstration of a new technique to measure the thermal conductivity of individual semiconductor NWs using Raman thermography.

4.1 Important Aspects to Raman Spectroscopy of Semiconductor Nanowires

4.1.1 Size Effects on the Raman Scattering from Individual Semiconductor Nanowires

The following two sections are reproduced in part with permission from the book chapter "Raman Spectroscopy for Characterization of Semiconducting Nanowires" authored by Gregory S. Doerk, Carlo Carraro, and Roya Maboudian, which will be published as part of the book "Raman Spectroscopy for Nanomaterials Characterization" edited by Challa S.S.R. Kumar.

Equation (1.11) in the Introduction implies that the Raman scattered intensity is proportional to the incident radiation intensity, and in turn on the square of the incident electric field amplitude. However, since Raman scattering depends on the dielectric polarization within the crystal, it is the internal field which must actually be considered, and the internal field is altered from the incident field by boundary conditions at the surface that require continuity of the tangential electric field and normal electric displacement vectors. Due to the unique geometries and sizes of NWs, a large dielectric mismatch between the wire and its surrounding medium require special calculations of the internal electric field. These calculations may be performed using computational methods such as finite difference approaches [6] or the discrete dipole approximation [153]; they may also be performed analytically by solving Maxwell's equations by separation of variables. This approach is completely analogous to Mie scattering theory for spherical scatterers. Analytical calculations explain a number of experimental phenomena exhibited in the Raman scattering from individual nanowires.

Consider the cylindrical nanowire geometry shown in Fig. 4.1, with an incident plane wave normal to the cylinder axis and with an electric field amplitude E_o. This is the simplest case to solve analytically and the one most often treated in experimental spectroscopic investigations of single NWs. Possible orientations of linearly polarized incident light with respect to the wire axis are bounded by two cases. The first is the transverse magnetic (TM) polarization where the electric field is polarized parallel to the wire axis, and the second is the transverse electric (TE) polarization where the electric field is polarized perpendicularly to the wire axis. In TM polarization the condition of continuity of the tangential electric field is expected to maximize the internal field, while in TE polarization the dielectric mismatch should suppress the internal field. The incident plane wave may be expanded in cylindrical functions as:

$$E_{inc} = E_o \hat{e} \sum_{n=-\infty}^{\infty} (-i)^n e^{in\theta} J_n(k_o r), \tag{4.1}$$

where $\hat{e}$ is a unit vector in the direction of the field polarization, $k_o = 2\pi/\lambda$ is the propagation constant in free space, and J_n is the Bessel function of integral order n.

In the normal incidence case presented here, the internal and scattered waves are of the same mode and polarization as the incident wave (mixing of the polarizations occurs when the incident wave is at an oblique angle). This yields two limiting cases for the internal electric field [154]:

$$E_{int}^{TM} = E_o \hat{z} \sum_{n=-\infty}^{\infty} (-i)^n e^{in\theta} d_n J_n(mk_o r) \tag{4.2a}$$

$$E_{int}^{TE} = E_o \sum_{n=-\infty}^{\infty} (-i)^n c_n e^{in\theta} \left[\frac{in}{r} J_n(mk_o r)\hat{r} - mk_o J_n'(mk_o r)\hat{\theta} \right] \tag{4.2b}$$

where $m = \sqrt{\varepsilon}$ is the complex index of refraction (ε is the dielectric constant) and prime denotes differentiation with respect to the argument. By applying the surface boundary conditions that require continuity of tangential components of $\boldsymbol{E}$ and the magnetic field intensity $\boldsymbol{H}$, the coefficients c_n and d_n may be related to the far field scattering coefficients

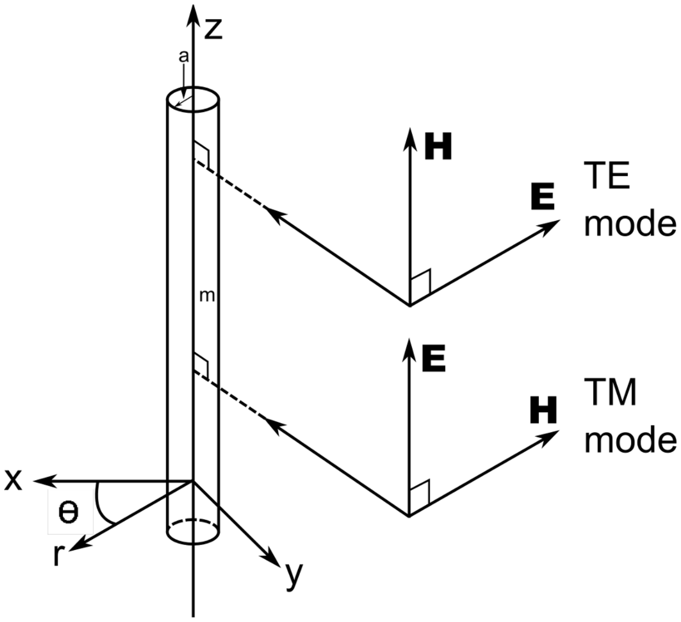

Figure 4.1: Coordinates for scattering of electromagnetic radiation at normal incidence by a cylinder with radius a and complex refractive index m, with the cylinder axis parallel to the z-direction. Cylindrical coordinates are z, r and θ.

a_n and b_n:

$$c_n = \frac{J_n'(k_o a) - a_n H_n'(k_o a)}{J_n'(m k_o a)} \tag{4.3a}$$

$$d_n = \frac{J_n(k_o a) - b_n H_n(k_o a)}{J_n(m k_o a)} \tag{4.3b}$$

Here, H_n refers to the Hankel function of the second kind. The values of a_n and b_n are given by

$$a_n = \frac{J_n(k_o a) J_n'(m k_o a) - m J_n'(k_o a) J_n(m k_o a)}{H_n(k_o a) J_n'(m k_o a) - m H_n'(k_o a) J_n(m k_o a)} \tag{4.4a}$$

$$b_n = \frac{m J_n(k_o a) J_n'(m k_o a) - J_n(m k_o a) J_n'(k_o a}{m H_n(k_o a) J_n'(m k_o a) - H_n'(k_o a) J_n(m k_o a)} \tag{4.4b}$$

The volume averaged intensity of the internal field per unit length is obtained by integrating the squared field amplitudes over the NW cross section, and the presence of Bessel functions in the result that are functions of the reduced optical radius, $m k_o a = 2\pi m a/\lambda$, reveals that the internal field is modulated in a way that depends explicitly on the NW diameter and the wavelength of incident light. This type of calculation has been used successfully to explain observations of enhanced first order Raman scattering per unit volume in Si NWs and nanocones (in reference to bulk Si) [155].

It also helps explain the strong polarization anisotropy or "antenna effects" [8, 153] in the Raman scattering of semiconductor NWs, so named because of the selective Raman scattering of TM polarized light by way of this structural resonance modulation. This behavior is quantified in the polarization anisotropy ratio, calculated by an averaging of the squared field amplitudes of the product of incident and scattered fields [8], determined from a Mie-type solution:

$$\rho = \frac{\langle |E^{TM}|^4 \rangle - \langle |E^{TM}|^2 |E^{TE}|^2 \rangle}{\langle |E^{TM}|^4 \rangle + \langle |E^{TM}|^2 |E^{TE}|^2 \rangle} \tag{4.5}$$

For NWs in the backscattering configuration with the excitation radiation at normal incidence, the term "polarized" refers to the case where both the incident and scattered radiation are polarized along the NW axis; in the "depolarized" case the incident and scattered radiation are polarized parallel and perpendicular to the NW axis, respectively (or vice versa). The polarized configuration gives the maximum signal intensity as both the internal field from the incident light and the Raman scattering field are maximized in the TM polarization. In the depolarized configuration the internal field is still maximized, but this is countered by the fact that the light collected by the spectrometer is from the TE polarization where the Raman scattering field is suppressed. The clear and practical implication of these findings for Raman investigations of single NWs is that the signal is maximized in the TM polarization. This becomes increasingly important as the diameter is decreased and the corresponding Raman scattering cross section becomes exceedingly small (even despite the relative enhancements over bulk crystals).

4.1.2 Effects of Temperature on Raman Spectra

Another intriguing quality of Raman spectroscopy is its capability to measure local temperature quantitatively and precisely. This is possible in two distinct ways, arising due to two different characteristics of the Raman spectra in crystalline solids. The first characteristic is the presence of the phonon occupation number in the Raman scattering cross section in accordance with equation (1.11). While the relation to temperature of the strict intensity of a particular phonon peak is obfuscated by the numerous other components of the Raman scattering cross section, taking the ratio of integrated intensities of the stokes (I_S) and anti-Stokes (I_{AS}) peaks provides the following relationship by which to measure temperature:

$$\frac{I_S}{I_{AS}} = A\left(\frac{\omega_S}{\omega_{AS}}\right)^3 \exp\left(\frac{hc\omega}{kT}\right) \tag{4.6}$$

where ω_S and ω_{AS} are the Stokes and anti-Stokes frequencies, ω is the phonon frequency (the subscript j has been dropped), and A is a constant determined by the light absorption of the sample and the scattering cross sections at the Stokes and anti-Stokes frequencies that should be calibrated for the sample. For bulk samples, the value of A is close to unity due to the fact that the Stokes and anti-Stokes frequencies differ from the frequency of the excitation line by a relatively small amount, making this a convenient measure of local temperature that is not dependent on extraneous factors such as stress or crystal quality. However, the application to NWs is not as straight forward. First, the resonant light interactions of NWs means that the value of A may change for any individual NW as a function of its diameter or the laser wavelength. Secondly, the accuracy of the method is significantly reduced when it becomes difficult to resolve the anti-Stokes peak, which is often a problem for small diameter NWs ($<\sim$ 50 nm) or when low laser powers are used to minimize local heating.

A more precise measurement of local sample temperature is made possible by the anharmonicity of the crystal vibrational potential energy. Phonon-phonon interactions that reduce individual phonon lifetimes, phonon softening, and thermal expansion give rise to increasing peak width and a change in peak frequency (typically negative) with increasing temperature. The variability of peak intensities under real experimental conditions and the factors such as doping or confinement that can affect peak shape and width make the dependence on peak width an imprecise measurement for temperature when applied to NWs. The peak position on the other hand is much more easily and accurately determined. Above room temperature and for a range of a few hundred degrees K the relationship between phonon frequency with temperature is typically linear, though calibration measurements are generally necessary for different types of samples.

4.2 Temperature Dependence of the Raman Spectra for Individual Silicon Nanowires

This section is reproduced in part with permission from: G.S. Doerk, C. Carraro, and R. Maboudian. Temperature dependence of Raman spectra for individual silicon nanowires. *Phys. Rev. B*, 80(7):073306, 2009. Copyright American Physical Society 2009.

The temperature sensitivity of Raman spectrometry may provide valuable insight into the thermal properties of nanostructures. Previous Raman investigations performed on ensembles of Si NWs with small diameters (D $\lesssim$ 20 nm) have assumed bulk anharmonic behavior in order to isolate the effects of quantum confinement [156, 157, 158]. Yet one report has claimed new anharmonic constants relating the temperature dependence of the first order optical phonon frequency from an ensemble of $\sim$20 nm diameter Si NWs [159]. Therefore, it is unclear whether anharmonic constants for silicon nanowires change with decreasing diameter and at what diameter this becomes significant. Furthermore, to date there have been no temperature related Raman studies of EE Si NWs, which would potentially aid in the clarification and verification of emerging models for heat transfer in roughened nanostructures, and will improve our understanding of the behavior of their high frequency phonons in general.

This section presents measurements of the temperature dependence of the Raman spectra for individual VLS Si NWs with diameters in the range of about $\simeq$30 to $\simeq$180 nm and of EE Si NWs with diameters in the range of about $\simeq$50 to $\simeq$130 nm, in the temperature ranges of 20 - 250 °C and 20 - 300 °C, respectively. VLS Si NWs were grown from a galvanically displaced Au film, and EE Si NWs were etched from n-type Si(111) wafers. Synthesis details for both types are given in Chapter 2. Wires were dispersed from suspension in ethanol onto Si(111) dice, each covered with an evaporated tungsten film to mask the substrate. Since both the wires synthesized by VLS epitaxy using $SiCl_4$ and the EE wires are straight, the wires layed flat on the film surface, maintaining good thermal contact. Tungsten was chosen because it is thermally and chemically stable, and forms no silicides below temperatures of 550 °C [160]. A portion of the substrate was covered during the evaporation so that the bulk silicon would be exposed in that region only. Raman spectrometry (JYHoriba LabRAM) was performed in backscattering configuration with an excitation line provided by a HeNe laser (632.8 nm wavelength) through an Olympus BX41 100X confocal microscope (numerical aperture = 0.8; laser spot size <1 μm). Samples were heated on a home-built resistive heating stage and were studied in room atmosphere. Due to the good contact with the substrate, the temperature of the NWs was taken to be the same as the temperature of the substrate, which was measured via the exposed Si section using the Stokes-antiStokes intensity ratio. The parameter A was measured as 0.96 for the Si substrate at room temperature and assumed constant for the range of temperatures studied. Due to the large polarization anisotropy in the Raman spectral intensity of NWs they were aligned along the laser polarization direction to maximize the intensity of the Raman spectra.

In order to properly probe the temperature response of individual Si NWs, the laser power must be large enough for accurate resolution of the Stokes and antiStokes peaks, but not too large so that local heating renders the assumption of near-thermal equilibrium with the substrate invalid. The Stokes to antiStokes peak ratio for the first order optical phonon has been previously used to estimate local temperature, and it is convenient in that it is not influenced by extraneous factors such as stress, doping, and confinement. However, there is no guarantee that the prefactor "A" is the same for any sized NW as for bulk Si, and accurate determination of I_{AS}/I_S becomes increasingly difficult as wire diameter and laser power are decreased. To circumvent the problem of high error in the I_{AS}/I_S ratio for smaller NWs, the Stokes first order optical Raman shift, which redshifts with increasing temperature due to lattice anharmonicity, was directly measured as a function of filtered laser power relative to the full laser power (the full, unfiltered power is approximately 10 mW at the sample). The power at which local heating is acceptably low is designated as the point in which the Raman shift plateaus at a constant value, as shown in Fig. 4.2. The Raman shift of bulk Si does not decrease below 521 cm^{-1}, the expected room temperature value which indicates no local heating, while the 129 nm diameter wire Raman shift decreases minimally ($\sim$0.8 cm^{-1}over the entire power range). The onset of local heating above a relative laser power of 0.05 is clearly seen by the decrease in Raman shift of $\sim$1.2 cm^{-1} for a 65 nm EE wire , and a decrease in Raman shift of $\sim$1.9 cm^{-1} for a the 33 nm VLS wire, the smallest wire studied in this report. Similar results were obtained for the other wires studied. Therefore, the temperature response for all VLS wires in this study was performed at relative laser powers of 0.05 (approximately 0.5 mW or 0.7 mW/μm^2) or less.

For individual Si NWs, the full width at half maximum of the first order Raman peak is rather imprecise due to large variability in absolute peak intensity arising from experimental factors such as correct focus and position of the laser spot. Therefore, investigation was restricted to the temperature dependence of the peak position. The Raman frequency is given by

$$\omega\left(T\right) = \omega_o + \Delta_{TE}\left(T\right) + \Delta_A\left(T\right) \tag{4.7}$$

where ω_o is the frequency at 0 K, $\Delta_{TE}\left(T\right)$ is the frequency shift due to thermal expansion, and $\Delta_A\left(T\right)$ is the frequency shift due to anharmonic phonon-phonon coupling [161]. Above room temperature the relationship between Raman shift and temperature is typically linear. Expanding expressions the the thermal expansion [161] and anharmonic coupling [162] effects in a Maclaurin series and cutting off at linear terms, the slope for this relationship is given approximately by:

$$\left(\frac{d\omega}{dT}\right) \approx -3\omega_o\gamma\alpha + \frac{k_B}{hc\omega_o}\left[4A + 9B\right] \tag{4.8}$$

where γ is the Gruneisen parameter, α is the coefficient of linear thermal expansion, and A and B are the cubic and quartic anharmonic constants respectively [162].

As a result, our data for Raman shift *vs.* temperature are fit with straight lines. Since other anharmonic contributions dominate over thermal expansion [163], a difference in the

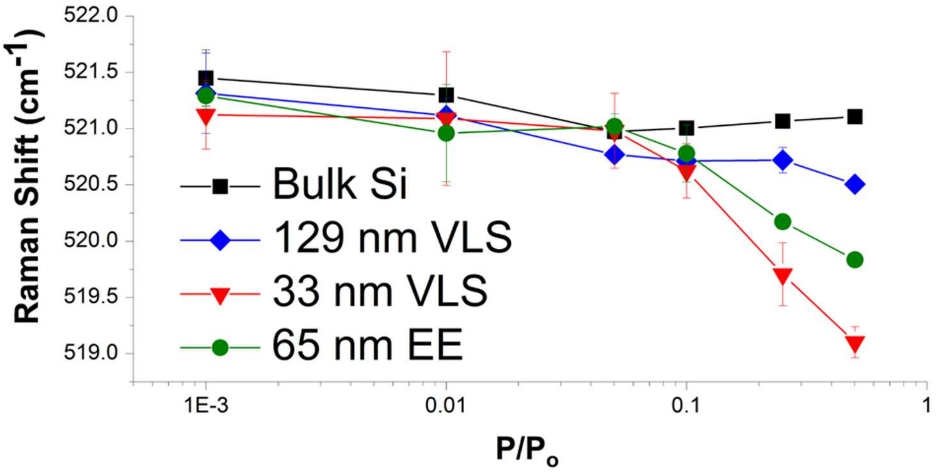

Figure 4.2: Calibration for determination of local heating effect *vs.* relative laser power (log scale) in VLS and EE Si NWs by measurement of the Raman shift of the optical phonon peak. The clear redshifts above a relative laser power of 0.05 for the 33 nm diameter VLS wire and the 65 nm diameter EE wire indicate the onset of significant local heating that skews the wire temperature to higher values than the underlying substrate.

slope of this line would indicate different anharmonic constants. Figure 4.3(a) is a plot of Raman shift versus T for the underlying bulk Si substrate. Linear regression analysis yields a slope for $\left(\frac{d\omega}{dT}\right)$= -0.022 ±.001 cm^{-1} °C^{-1}, which is in good agreement with previous reports that give a value of $\left(\frac{d\omega}{dT}\right) \approx$ -0.024 cm^{-1} °C [161, 163, 164]. The discrepancy may arise from the more limited range of temperature used in our experiment and the assumption of a constant prefactor in equation 4.6 over the full temperature range. However, concerning the anharmonicity of Si NWs, it is important to compare direct measurements made in the same manner. Figure 4.3(b) shows the dependence on temperature of the optical Raman shift of a 50 nm VLS wire, for which linear regression gives a value for $\left(\frac{d\omega}{dT}\right)$ of -0.022 ± .001 cm^{-1} °C^{-1}. Similarly, linear regression of the optical Raman shift dependence on temperature for a ∼50 nm EE NW, shown in Fig. 4.3(c), yields a slope of -0.022 ± .001 cm^{-1}. These values for $\left(\frac{d\omega}{dT}\right)$ are equivalent to the bulk Si value, indicating no change in the anharmonic constants for these nanowires compared to bulk Si. In fact, as shown in Fig. 4.3(d) the temperature dependence of the Raman spectra is nearly the same as for bulk Si across the range of NW diameters examined, with no trend apparent.

Anharmonic contributions may dramatically effect lattice thermal conductivity. For example, strong anharmonic coupling between guest and host atom vibrational modes is believed to be responsible for the glass-like thermal conductivity in crystalline clathrate compounds [165, 166]. Since previous treatments of surface roughness could not properly account for the lower thermal conductivity of EE Si NWs [24], factors such as boundary-induced ad-

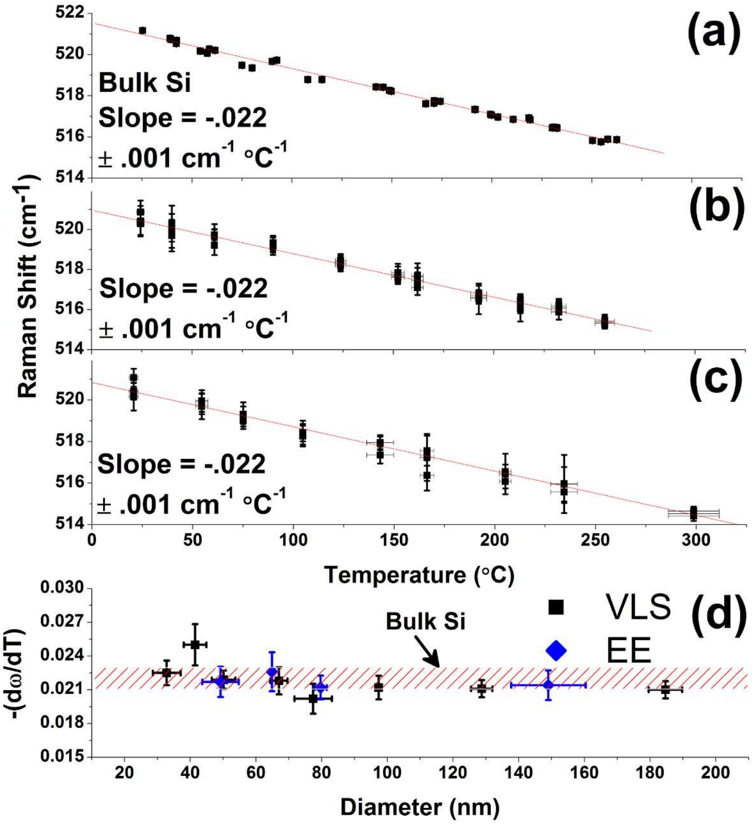

Figure 4.3: (Color online) Temperature dependence of the optical phonon frequency for: (a) A bulk silicon sample, (b) a 50 nm VLS Si NW, and (c) a 50 nm EE Si NW. (d) Slope of optical phonon Raman shift *vs.* temperature for VLS Si NWs ranging in diameter from 33 to 185 nm and for EE Si NWs ranging in diameter from 50 to 150 nm. They are all scattered around the value for bulk silicon, with no apparent trend with diameter, indicating that the slopes are all equal to the bulk silicon value after accounting for experimental error.

justments in the effective lattice anharmonicity of the EE Si NWs may play a role and provide a possible explanation. In light of the surprisingly low thermal conductivity of a ∼50 nm EE NW in Ref. [24] that approaches the amorphous limit, the above results are of particular interest. While heat is believed to be transported primarily by lower frequency acoustic phonons [167], it has recently been suggested that accurate quantitative description of the thermal conductivity in semiconductors requires inclusion of the anharmonic optical phonon decay to acoustic phonons [168, 169].

Thus, a change in the anharmonicity of optical phonons or higher frequency acoustic phonons in nanowires could then help account for reductions in heat transport beyond those described through boundary scattering alone. Measurements were performed of the temperature dependence of the zone-boundary transverse acoustic overtone (2TA) peak in the vicinity of 300 cm^{-1} for a 80 nm EE wire and a 77 nm VLS wire yielding slopes of -0.0133 ± 0.003 cm^{-1} $^{\circ}\text{C}^{-1}$and -0.0135 ± 0.002 cm^{-1} $^{\circ}\text{C}^{-1}$ respectively. These values are nearly identical to that measured for bulk Si, -0.0132 ±0.001 cm^{-1} $^{\circ}\text{C}^{-1}$, indicating that bulk silicon anharmonicity is retained for this two-phonon acoustic interaction as well. Therefore, it may be inferred that lattice anharmonicity cannot play a significant role in the severely depressed thermal conductivity in roughened EE Si nanowires compared with smooth-surfaced VLS Si nanowires.

4.3 Measuring the Thermal Conductivity of Individual Nanowires *via* Raman Thermography

This section is reproduced in part with permission from: G.S. Doerk, C. Carraro, and R. Maboudian. Single nanowire thermal conductivity measurements by Raman thermography. *ACS Nano*, 4(8):4908-4914, 2010. Copyright 2010 American Chemical Society.

Despite recent advances in the understanding of NW properties, the development of NW-based technologies is hindered by a lack of rapid, non-destructive characterization methods with sub-micron resolution. In the measurement of NW and nanotube thermal conductivity, while the micro- heater/thermometer [50] and the 3ω techniques [49] are precise, they are also slow and essentially destructive. As a non-contact probe of local temperature with submicron resolution, Raman thermometry is especially suited for measuring nanostructure thermal properties, and has recently been applied to graphene [170] and carbon nanotube bundles [171]. In such a method, optical absorption of the material at the relevant wavelength must be independently measured or estimated.

This section demonstrates a simple, non-contact method to measure the thermal conductivity of cantilevered NWs by locally heating them along their axes with a focused laser while simultaneously measuring the local temperature at the same spot through Raman spectrometry. Optical absorption is calculated using a solution to Maxwell's equations for an infinite dielectric cylinder and is validated by the good agreement of the extracted thermal conductivities with those expected due to diffuse phonon-boundary scattering. By comparing results performed at reduced pressure to those done in air, we find that convection does not induce significant error for the range of diameters probed. Finally, we note that if a functional relationship for thermal conductivity is known, this method introduces a simple way to directly measure optical absorption cross sections.

Si NWs were synthesized by VLS growth from 50 nm or 200 nm Au colloidal catalysts on the {111} walls of previously fabricated silicon-on-insulator microtrenches.[79] The large height of the trenches (80 μm) makes any Si background signal negligible when collecting Raman spectra from cantilevered NWs. Au agglomeration and ripening leads to a diameter distribution. Though conditions were optimized to minimize NW taper, even very slight tapering gives rise to some error in the measured NW diameters, the implication of which will be discussed in upcoming paragraphs. The NW dimensions were measured from SEM images obtained using a Leo 1550 field emission SEM. The diameter error values used in the analysis are obtained from the NW taper in the region probed by the laser spot and are larger than the resolution of this SEM.

Raman spectra were acquired in backscattering configuration at room temperature. The excitation line was provided by a HeNe laser (632.8 nm wavelength) through an Olympus BX41 super long working distance 100X confocal microscope (numerical aperture = 0.6) which produces a 1.27 μm diameter laser spot. The incident laser light was linearly polarized along the NW axes to maximize scattered intensity and simplify the optical absorption calculation. This was achieved by setting a half-wave plate polarizer in the beam path before the sample to zero and aligning the sample such that the NWs would lie along the laboratory axis corresponding to the direction of the electric field polarization. No polarizers were applied to the collected signal. Power at the sample position was controlled by neutral density filters and varied from 0.25 mW to 2 mW as measured by a hand-held laser power meter. Raman mapping was done using a high-resolution piezoelectric positioning stage (PI P-562.3CD) with a 10 nm minimum step, interfaced with Labspec v.4 software on a personal computer. Steps along the wire axis ranged from 0.2 to 0.5 μm for total probed lengths from 1.2 to 5 μm, while at least 6 steps each 0.33 or 0.5 μm were taken across each NW axis. In some cases the wall contact was not actually in the Raman map, which is acceptable since the thermal conductivity measurement does not depend on thermal contact resistance. Raman spectra at each point are the average of at least three measurements with an integration time of 5s or greater. Some of the measurements were performed with the sample held at pressures less than 10^{-1} Torr using a Linkam THMS350V vacuum stage (pressure reduced by a mechanical pump) with a $\sim$0.3 mm thick borosilicate glass window attached to the piezoelectric stage.

The line of highest Raman signal intensity along the NW axis direction was used to determine the temperature profile. First order optical phonon peak positions in Raman spectra taken along the length of NWs were obtained using fitting functions built-in to the LabSpec software specifically for Raman mapping and a Lorentzian lineshape was used. In a few cases, fitting was also performed (again to a Lorentzian lineshape) using the Origin

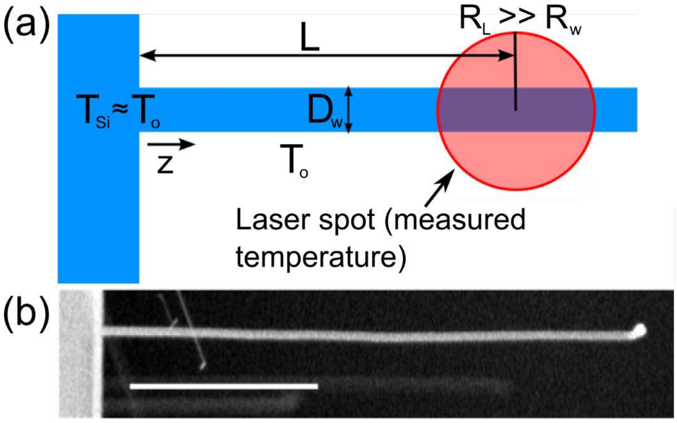

Figure 4.4: (a) Schematic (top view) of the measurement principle. (b) SEM image of an as-grown cantilever Si NW (scale bar = 5 μm).

software package to check the results from fitting in LabSpec and to obtain estimates of the error in peak position, and hence the error in the temperature measured at each point along the wire axis. Conversion of the peak position data to temperature data was accomplished by applying the anharmonic relationship between these two properties. Measurements on each NW were initially performed at a conservatively low power and then analyzed to determine if the thermal conductivity data could be extracted. If a clear temperature rise along the NW axis was not observed, the measurement was performed again at a laser power one level higher. Temperature-position slope values were obtained from at least 5 points, though in most cases 7 to 12 points were used.

Figure 4.4(a) shows a top view schematic of the measurement setup. A Raman map is made around a cantilevered Si NW (an example is shown in Fig. 4.4(b)) by moving the sample using a nanopositioning stage with respect to the laser spot. The laser heats the NW at a length from the trench wall, L, where it crosses the NW axis. Temperature can be measured locally at the same laser spot by the position of the optical phonon peak in the acquired Raman spectra. The trench wall acts as a thermal sink maintaining constant (room) temperature and the heat transfer problem is effectively one-dimensional for two reasons: First, in cases where the effective phonon mean free path for heat transfer in bulk crystals (on the order of a few 100 nm for Si at room temperature [172]) is expected to be larger than the relevant sample dimension, it may not be possible for a temperature gradient to exist across this dimension [173]. This is true for Si NWs with diameters in the range studied here. The axial dimensions are much longer than the same effective phonon mean free path, making local temperature definition unproblematic along NW lengths. Secondly, since the laser spot diameter is much larger than the NW diameter, the measured temperature can be considered radially averaged and the heat problem is rendered one-dimensional.

Radiative heat loss is negligible compared with conduction near room temperature [50, 171]. In the simplest case where convection may also be neglected the problem may be treated with a simple linear heat resistor model. At steady state under these conditions, the temperature will be constant from the laser spot to the end of the NW (opposite side from the NW base). Then the temperature difference is given by

$$\Delta T = \left(R_c + \frac{4L}{\pi D_w^2 k_w} \right) \dot{Q} \tag{4.9}$$

where $\dot{Q}$ is the heat conducted down the wire, D_w is the NW diameter, R_c is the thermal contact resistance at the NW base, k_w is the NW thermal conductivity, and ΔT is the difference between the radially averaged temperature at the laser spot L and the temperature at the NW base ($\Delta T = \bar{T} - T_o$). Considering that ΔT increases linearly with L, we may instead measure the slope S of ΔT vs. L (determined by linear regression) and rearrange (4.9) to develop a simple expression for thermal conductivity that bypasses a dependence on the thermal contact resistance as well as any effect from the uncertainty in the absolute magnitude of L:

$$k_w = \frac{4\dot{Q}}{\pi D_w^2 S}. \tag{4.10}$$

If it is assumed that all of the laser power absorbed is converted to heat that is conducted down the wire, then $\dot{Q}$ is proportional to the laser power at the sample P and the ratio of NW area exposed to the beam to the area of the focused beam spot. Using an average laser power is appropriate since the full laser spot diameter is sampled along the length of NW directly under the beam. Approximating the exposed area as $\pi D_w D_L/2$, where D_L is the laser spot diameter, the NW thermal conductivity may be expressed as

$$k_w = \frac{8cQ_aP}{\pi S D_w D_L} \tag{4.11}$$

The parameter c is a correction factor that represents the proportion of incident radiation transmitted (not extinguished) with a window in place that was necessary when low pressure measurements were performed to examine the assumption of negligible convection. At low pressure ($< 10^{-1}$ Torr) the mean free path of air molecules is over 1000 times larger than the NW diameters, and convection is negligible [171]. This is not necessarily true at ambient pressure.

The window correction factor (c) was determined from the integrated optical phonon peak intensities at ~520 cm^{-1} with and without the window in place. The intensity of light reaching the surface I_i is taken to be related to the intensity of light from the laser at the sample I_L by:

$$I_i = cI_L \tag{4.12}$$

The Raman scattered intensity is proportional to the incident intensity according to eqn. (1.11), but the signal collected will again be affected by extinction at the window. Since the

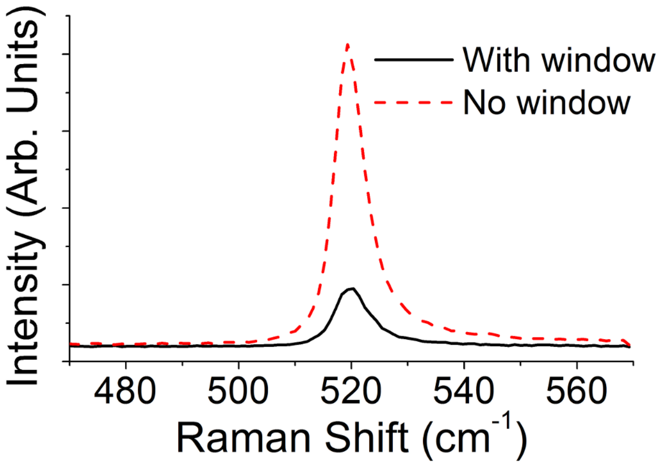

Figure 4.5: Raman spectra used for determining the window correction factor

wavelength of the Raman scattered light will differ in wavelength by $\leq 4\%$ from incident light, we may assume that the proportional extinction at the window is equivalent for the incident and scattered light. The collected Raman scattering intensity I_R will then follow the proportional relationship with the window in place

$$I_R \propto c^2 I_L. \tag{4.13}$$

The value of c may then be obtained from the square root of the ratio of the Raman scattered intensity with the window to that without it at the same laser power:

$$c = \sqrt{\frac{I_{R,window}}{I_{R,no\,window}}} \tag{4.14}$$

where $I_{R,window}$ and $I_{R,no\,window}$ are the integrated intensities in the acquired Raman spectra with and without the window in place, respectively.

Figure 4.5 depicts an example of Raman spectra for bulk Si in the vicinity of the optical phonon line with and without the window in place. The peak intensities were fit with two Gaussian line shapes to get the most accurate integrated intensities. A slight asymmetry to higher wave number in each peak is seen as a result of Fano interference from free holes since these samples were doped with boron at concentrations greater than 1 x 10^{19} cm^{-3} [142]. The value estimated for c was 0.47 ± 0.02.

The most important parameter in equation (4.11) is the absorption efficiency, Q_a, defined as the ratio of the absorption cross section to the geometrically obstructed area [154]. As noted earlier in this chapter, the subwavelength dimensions of NWs result in diameter dependent modulations in their interactions with light from their dielectric mismatch with the environment. In particular, light absorption resonances arise when the wavelength is matched to an eigenmode of the nanowire [8, 6]. As also noted earlier, accurate calculation of these resonances may be performed using finite difference techniques [6, 7] but in simple cases Q_a may be estimated by the more computationally friendly Mie-type solutions to Maxwell's equations, which have been shown to describe the diameter and incident wavelength dependent optical behavior of NWs very well both in Raman spectra [8, 155] and photocurrent measurements [6, 7, 29]. For radiation at normal incidence polarized along the NW axis (TM polarization) the absorption efficiency for an infinite circular dielectric cylinder can be calculated using the following equation [154]:

$$Q_a = \frac{2}{\alpha}\left[Re\left(b_0 + 2\sum_{n=1}^{\infty} b_n\right) - |b_0|^2 - 2\sum_{n=1}^{\infty} |b_n|^2\right] \tag{4.15}$$

where b_n is given in (4.4). In this equation $\alpha = \pi D_w/\lambda$ where λ is the wavelength of incident light. Using complex index of refraction values at $\lambda = 632.8$ nm for bulk single-crystal Si [174], the calculated absorption efficiencies for Si NWs exhibit characteristic resonances at particular diameters as shown in Fig. 4.6. Implicit in this approach are assumptions that the native oxide layer (~2-3 nm) has only a negligible effect on absorption and that this calculation based on a cylinder works well for Si NWs though their actual radial cross sections are hexagonal. Furthermore, because the NWs studied here exhibit varying degrees of tapering, the diameter used in calculation is average over the probed length, the consequence of which will be discussed later. The absorption efficiency Q_a is calculated using Mathematica 5. Common derivative relations for both Bessel and Hankel functions were used [175] and summations were carried up to n = 10, above which no significant changes in the dependence of Q_a on diameter were observed.

Figure 4.8(a) is a SEM image of a 78 nm diameter Si NW measured in this study, and Fig. 4.8(b) is the corresponding Raman intensity map of the same wire in ambient air at a laser power of 0.4 mW. An illustrative Raman spectrum centered on the optical phonon frequency taken at the point marked by a circle in (b) is shown in Fig. 4.8(c). This shape is typical for single-crystal Si and shows no assymetric broadening to lower wavenumber that is characteristic of optical phonon confinement and is usually found only in Si NWs less than ~20 nm in diameter [157]. A line profile of the Raman shift is extracted from the highest intensity vertical line on the Raman map, marked by a black dashed line in (b), and the temperature increase as a function of L is obtained using the known $d\omega/dT$ value, as shown in Fig. 4.8(d). The step size may be made arbitrarily small (limited by the piezoelectric stage resolution) as long as the laser-induced temperature difference increases monotonically along the NW axis and the total temperature increase is greater than the temperature measurement error. Additionally, though the maximum temperature rise does exceed 100 K in some measurements, the thermal conductivity of Si NWs has been found to be very flat in the vicinity of room temperature [21], indicating that it may be considered constant for this limited temperature range.

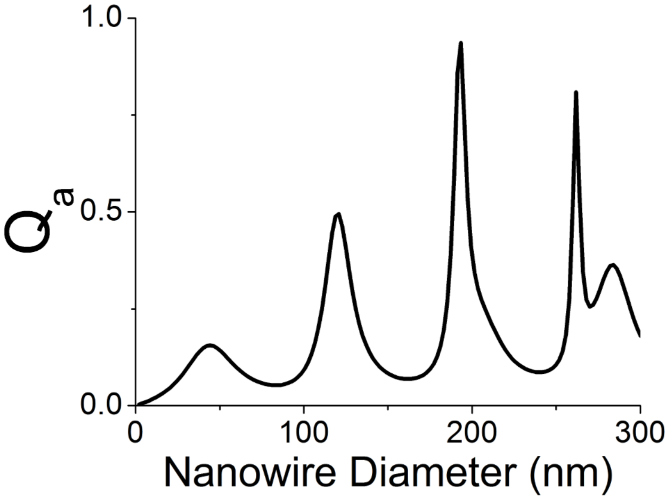

Figure 4.6: Calculated Si NW absorption efficiencies, Q_a as a function of diameter using equation (4.15) in the text.

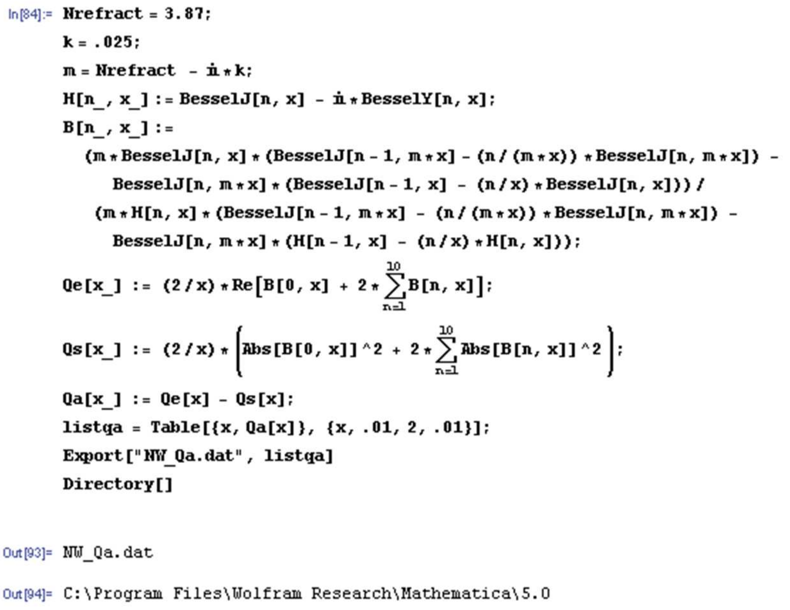

```
In[84]:= Nrefract = 3.87;
         k = .025;
         m = Nrefract  - ⅈ * k;
         H[n_, x_] := BesselJ[n, x] - ⅈ * BesselY[n, x];
         B[n_, x_] :=
           (m * BesselJ[n, x] * (BesselJ[n - 1, m * x] - (n / (m * x)) * BesselJ[n, m * x]) -
              BesselJ[n, m * x] * (BesselJ[n - 1, x] - (n / x) * BesselJ[n, x])) /
            (m * H[n, x] * (BesselJ[n - 1, m * x] - (n / (m * x)) * BesselJ[n, m * x]) -
              BesselJ[n, m * x] * (H[n - 1, x] - (n / x) * H[n, x]));
                                              10
         Qe[x_] := (2 / x) * Re[B[0, x] + 2 * ∑ B[n, x]];
                                             n=1
                                                             10
         Qs[x_] := (2 / x) * (Abs[B[0, x]] ^ 2 + 2 * ∑ Abs[B[n, x]] ^ 2);
                                                            n=1
         Qa[x_] := Qe[x] - Qs[x];
         listqa = Table[{x, Qa[x]}, {x, .01, 2, .01}];
         Export["NW_Qa.dat", listqa]
         Directory[]

Out[93]= NW_Qa.dat

Out[94]= C:\Program Files\Wolfram Research\Mathematica\5.0
```

Figure 4.7: Mathematica code for calculating Q_a.

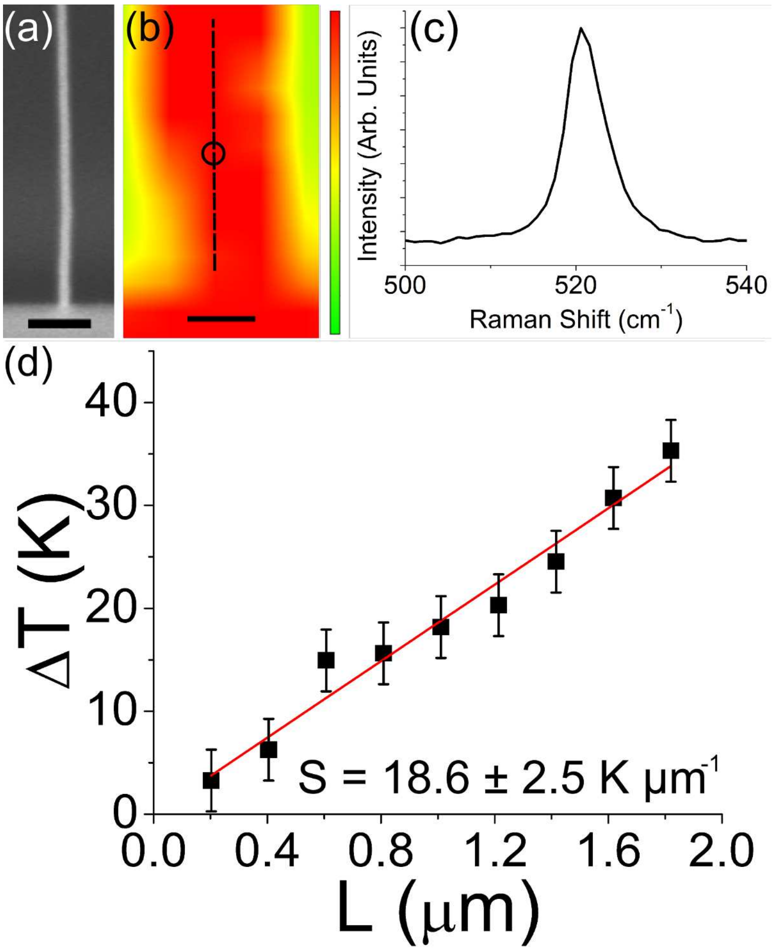

Figure 4.8: Representative measurement on a single ∼78 nm Si NW. SEM image (a) and the corresponding map of the optical phonon integrated peak intensity (b) of this NW. The scale bar is 500 nm for both images. (c) Raman spectrum centered on the optical phonon frequency acquired from the point in (b) marked by a black circle. (d) Temperature difference at the laser spot from the ambient temperature as a function of the distance (L) from the NW-wall contact.

The simplicity of both setup and calculation renders the cantilever geometry used here ideal for the measurement of thermal conductivity through combined laser heating and Raman thermography. The normal incidence of the laser is a noteworthy aid in simplifying the calculation; heating with laser light at an oblique incidence requires the inclusion of transverse electric (TE) cross modes in determining the absorption efficiency [154]. In principle though, Raman thermography may also be applied to nanowires or nanotubes in a variety of in-plane geometries, which are commonly used in many characterization methods. For nanowires in a bridging geometry for instance, the thermal conductivity can be obtained from the curvature of the parabolic temperature-position curve (convection and radiation are asssumed to be negligible). Unfortunately, the thermal contact resistance remains in the expression, adding a level of uncertainty [176]. Typical device geometries (where a NW sits on top of an insulator with metallic electrical contacts) may also be considered, though a term accounting for heat transfer to the substrate must usually be included in the analysis [177]. Nevertheless, with the precision temperature measurements possible through Raman thermometry it may be possible in any setup to decompose the heat transfer problem in a way to isolate thermal conductivity or to study limiting cases such as when thermal contact resistance is negligible, indicating the versatility of Raman thermal measurements. Moreover, Raman thermometry may be used in conjunction with other electrical or optical measurements to reveal concurrent thermal behavior.

In all conditions, care must be taken to distinguish signal from the NW under inspection from other nearby NWs. While the Rayleigh criterion for resolution indicates a minimal in-plane NW separation of approximately half the laser spot size ($\sim$0.6 μm here), easy discrimination of the Raman signal from distinct NWs of the same type suggests a practical separation of a couple of microns. Additionally, there are possible limitations in the length or diameter of NWs investigated through the technique presented here. While the minimum or maximum NW length is not set by the separation of the contacts (as is the case in the microheater method [50]), the length of the NW must be longer than the laser spot diameter to preclude end effects, and the NWs should be long enough so that a temperature-position slope may be obtained with minimal error. However, since the conductive thermal resistance of the NW grows with increasing distance from thermal sink, for large L it may approach equivalence with convective thermal resistance. In the NWs studied here, the length used is also kept to a minimum since the taper of the NW may significantly change the optical absorption behavior across a large L value. Furthermore, in NWs with diameters smaller than those studied here ($<\sim$30 nm), measurements are complicated by the inability to actually see the NWs under the optical microscope, the increased likelihood of destroying the NW with the laser irradiation, and other factors such as optical phonon confinement effects on the Raman spectra [157]. However, the fact that the laser is actually *expected* to heat the NW implies that there is no minimal diameter if proper precautions are used.

The results of thermal conductivity measurements on six Si NWs at low pressure and in air are shown in Fig. 4.9. For comparison, Si NW thermal conductivities above room temperature ($\sim$310 K) previously measured by Li et al. (Ref. [21]) through heated Pt

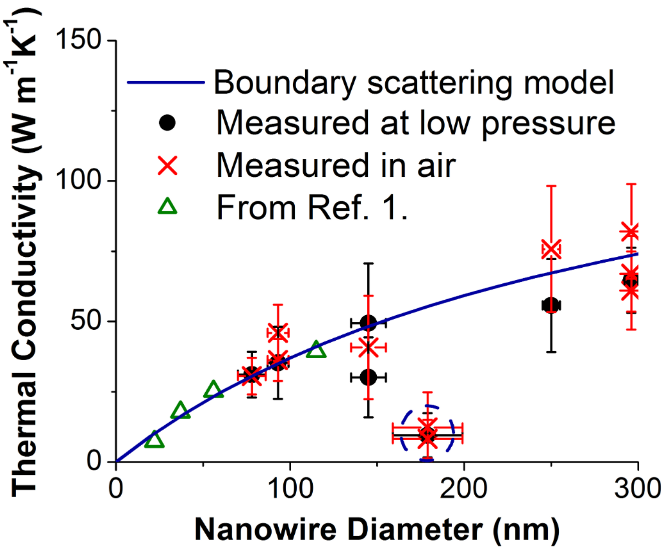

Figure 4.9: Thermal conductivity measurements for individual Si NWs in air and at low pressure. The predicted curve assuming diffuse boundary scattering is included for comparison, as well as previous experimental data from VLS Si NWs in Ref. [21].

microthermometers were included as well as the expected curve for Si NW thermal conductivity if the only additional factor lowering its value from that of pure bulk Si is fully diffuse phonon-boundary scattering. Applying Matthiessen's rule for multiple scattering, the expected NW thermal conductivity is given as

$$k_{w,exp} = \frac{D_w k_{bulk}}{l_{bulk} + D_w} \tag{4.16}$$

where k_{bulk} is the bulk Si thermal conductivity (148 W/mK at room temperature) and l_{bulk} is the effective bulk Si mean free path, which is approximately ∼300 nm as obtained from measurements on thin films [172]. There is reasonable agreement between the measured points and the predicted values.

It is also notable that many of the measurements made in air and those made at low pressure match each other well, although the gaseous mean free path, λ_{mfp} (which is inversely proportional to absolute pressure), is very different in each case. When λ_{mfp} is much larger than the diameter ($\lambda_{mfp}/D \geq 10$) then convection may be understood in terms of individual collisions of gas molecules on the NW surface and its contribution can be calculated according to the kinetic theory of gases [50]. In this regime convective heat transfer is linearly proportional to the pressure [178, 179] and is negligible in comparison to conduction [171, 179]. In the other extreme where $\lambda_{mfp}/D \leq 0.1$ (the continuum regime), thermal gradients with a scale on the order of the NW diameter can exist in the surrounding gas ambient, and convection tends to be more significant. Quantitative heat convection is then usually estimated according to empirical correlations. For the transitional regime in which these measurements in air were performed($\lambda_{mfp}/D \leq 1$) the relative contribution of convection is not always clear. The similarity in NW thermal conductivity values for measurements in air and vacuum suggests that convection is not a major source of error in this measurement. However, other methods of measuring thermal conductivity may be more sensitive than the one presented here, especially if they depend on small, precisely measured temperature differences.

A clear exception to the agreement between the measured data and the boundary scattering model occurs for a diameter of approximately ∼180 nm that is circled in Fig. 4.9. A SEM image of this nanowire is shown in Fig. 4.10(a). The average diameter was used for estimating the value of the calculated Q_a to apply in determining k_w, but due to an anomalously high taper for this NW the actual diameter range probed crosses a large absorption resonance, as seen in Fig. 4.10(c). To examine this aberrant measurement in more detail expected values of ΔT as a function of the L were calculated by replacing the average D_w in equation (4.9) with a value that changes linearly with L as obtained by the measured taper. The value of Q_a is allowed to change as well according to its dependence on D_w in equation (4.15), and the expected thermal conductivity from equation (4.16) is used making it diameter dependent as well. Thermal contact resistance is neglected as it should only shift the temperature difference at the base.

The resulting values are shown alongside the experimentally measured values in Fig. 4.10(b). While the two curves appear to agree near the NW base, the calculated ΔT values quickly fall off before ∼1 μm. The decrease in both k_w and D_w over L should increase ΔT so it is clear that the calculated curve is dominated by the behavior of Q_a. The experimental results then suggest that the NW is absorbing 633 nm wavelength light resonantly. Indeed, with the diameter fixed at the average value of ∼180 nm and by using the thermal conductivity from equation (4.16) at this diameter value, the NW possesses an effective absorption efficiency of approximately ∼0.7 ± 0.3, close to the resonant maximum of ∼0.94 as seen in Fig. 4.10(c). The difference in the mean diameter of this NW from the calculated diameter of the absorption resonance may reflect the inability of this simplified calculation to address absorption in highly tapered NWs. However, previous photocurrent measurements have shown that experimental resonance curves may be shifted and broadened from the calculated Mie resonance values [6, 7, 29]. Furthermore, the geometric cross sectional shape may also affect the specific resonant position [7], so a shift in resonant behavior from the calculated curve due to the fact that the Si NWs here are not perfect cylinders but rather possess a hexagonal cross section cannot be ruled out.

While this is a complication with regard to thermal conductivity measurements, it provides an opportunity to directly and quantitatively measure single nanostructure absorption cross sections. In photocurrent measurements for example, while external quantum efficiency η_E is measured, the internal quantum efficiency η_I and Q_a are coupled and neither is directly measured [6, 7]. Having an independent means of measuring Q_a would make photovoltaic

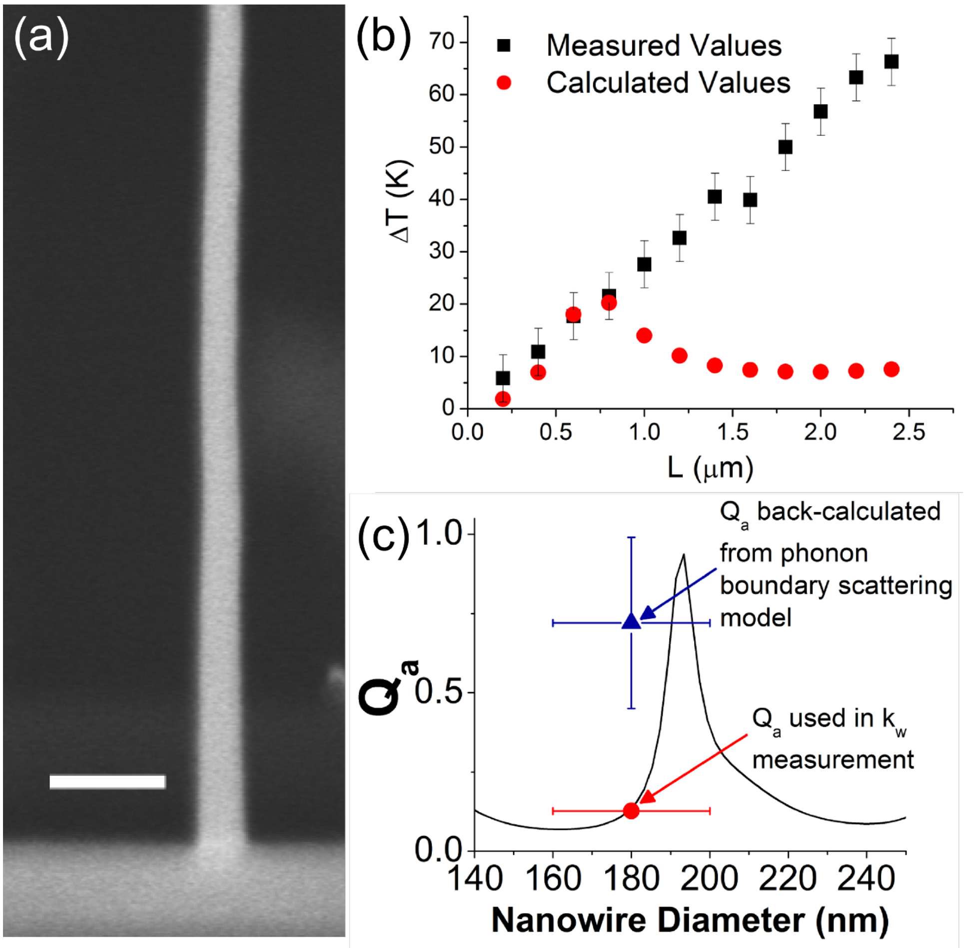

Figure 4.10: Inverse measurement of the absorption efficiency for an individual highly tapered Si NW. (a) SEM image of the tapered Si NW (scale bar = 500 nm). (b) Experimental ΔT vs. L for this NW, and expected values calculated according to equation (4.9) but allowing D_w, Q_a and k_w to vary with L. (c) Comparison of Q_a calculated according to equation (4.15) with the value back-calculated from the experimental data in (b) using k_w predicted by the phonon boundary scattering model at the mean diameter for the NW shown in (a).

characterization of nanostructures more complete. The potential to measure the absolute magnitude of absorption cross sections through Raman thermography by techniques such as the one described here may provide a valuable complement to other photovoltaic measurements. In cases where the thermal conductivity of a nanostructure is well-understood but the morphology makes optical absorption estimates unclear, this is especially valuable.

Chapter 5

Conclusions and Future Work

The preceding chapters have layed out the promises and challenges underlying the synthesis, integration, and characterization of Si NWs (and semiconductor NWs in general). The versatility of VLS growth is embodied in the use of Pt and Au catalysts, the novel synthesis of nanotrees using migration of the catalyst material, and the fabrication of electrically conductive Si nanobeams through the epitaxial growth of NWs that bridge two distinct electrodes. Block copolymer templating of NW growth catalyst seeds and *ex situ* boron doping are demonstrated as promising aids in epitaxial NW device integration, while Raman spectrometry provides a encouraging alternative way to measure critical NW thermal properties. Numerous directions to pursue in continued research could be envisioned, but here only two will be presented.

5.1 Characterization and Applications of Silicon Nanotrees

While HRTEM images have permit tentative assignment of crystal planes to the sawtooth facets found on the primary NWs in the nanotrees described in Chapter 2, other important structural features could be elaborated on further. In particular, the atomic level texture of these facets (they are not atomically smooth), the basal structure of the branches and their particular relationship to the trunk facets, the existence and nature of crystal defects at the interface between the branches and trunk, and the microstructure at the edges and vertices between facets are not very well-understood. Furthermore, since Au remains the dominant catalyst for VLS growth of Si NWs, understanding the ways that Au migrates (whether as droplets or as homogeneous liquid) and atomically distributes on the Si NW surfaces, and how it alters nanotree and NW morphologies is critically important.

High angle annular dark-field scanning TEM (HAADF-STEM) tomography combined with aberration-correction may enable unprecedented point-to-point resolution, tilt angles, and chemical sensitivity for very high fidelity three-dimensional atomic-scale mapping of the structures of these silicon nanotrees simultaneously with their atomic level Au distribution. Special methods for the preparation of single nanotree tomography samples using focused ion beam machining are likely necessary, but the many added insight may arise from such experiments. Indeed preliminary HAADF-STEM images from TEAM 0.5 at NCEM of a silicon nanotree show atomic level Au coverages (monolayers or even individual atoms) on Si nanotree facets.

Though visualization of the dynamic process of Au-induced faceting of silicon nanowires would provide substantial insight into its mechanism, it has yet to be demonstrated. Si NWs that are quenched immediately after growth by cooling rapidly in a non-reducing atmosphere exhibit minimal Au migration from the catalyst tip. Since Au migration has been witnessed during growth at pressures higher than 10^{-5} torr [84], it is possible to monitor the migration of Au from a silicon nanowire catalyst tip at possibly atomic resolution inside TEMs by heating the NW *in situ* with use of the heated sample holders (as long as the native oxide is freshly removed by a vapor HF etch immediately before insertion in the TEM). This type of experiment would provide a precise measurement of the rate of Au surface migration along with direct visual evidence of the mechanisms for Au nanoparticle formation and Au-induced Si faceting on NW surfaces, with special attention paid to any dependence on the diameters of the NWs. It could also potentially provide real-time visualization of radial atomic Au incorporation into the Si lattice.

Finally, in a more applied direction, measuring transport properties of branched NWs is another avenue for future research. To date the literature concerning transport in individual nanostructures with complex morphologies is quite lacking, but there are reasons that it should be interesting. For instance, Moore *et al* demonstrated through Monte Carlo calculations that NWs with large sawtooth faceting may exhibit thermal conductances less than what is expected for diffuse phonon boundary scattering [180], though to date there have been no experimental measurements to determine the real extent of the thermal conductivity reduction for coherent surface roughening (i.e. very regular sawtooth faceting) *versus* the situation with incoherent surface roughening described in the Introduction. Furthermore, density-functional theory calculations by Markussen *et al* suggest that Si nanotrees may exhibit thermoelectric figures of merit rivalling that of the very rough Si NWs [181]. The sawtooth-faceted Si NWs and Si nanotrees in chapter 2 are an ideal platform to study the real impact of these morphological perturbations on thermal transport.

5.2 Other Possible Measurements Using Raman Spectroscopy

While the NW thermal conductivity measurement (or estimation) method based on Raman thermography presented in the preceding chapter is a powerful and convenient addition to the toolbox for characterization and metrology of nanostructures, it is hindered by the need for a separate measurement or calculation of the absorption efficiency. While this may be incorporated into the measurements setup (by for example possibly using photodetectors underneath the NW), it would be better to develop a method that avoids heating with the laser at all, with heat provided to the NW by another source (Raman spectra would still be used to measure local temperature along the NW axis). A convenient setup would be to use Joule heating for NWs incorporated in a 4-point probe electrical setup (such as the one shown in Fig. 5.1) on an insulating substrate so that electrical contact resistances could be estimated. Assuming the very simple case where both inner contacts are at the same constant temperature (T_o), the one dimensional temperature profile along the NW axis can be described by the equation [177]:

$$T(x) = T_o + \frac{I^2\,(R - R_C)}{gL}\left[1 - \frac{\cosh(px)}{\cosh(pL/2)}\right] \tag{5.1}$$
$$p = \sqrt{g/kA}$$

where I is the current, x is the distance along the wire from the midpoint between inner contacts, R is the NW resistance, R_C is the electrical contact resistance, L is the length between the two inner contacts, A is the NW cross sectional area, k is the thermal conductivity, and g is the unified heat transfer coefficient (to the underlying substrate and air by convection, conduction, and radiation). This particular experimental arrangement avoids the need to estimate absorption from incident radiation, but care must be taken then to avoid local heating. If a clear temperature maximum is obtained (from $dT/dx \approx 0$ near $x = 0$), then the effects from g and k can be easily distinguished, guaranteeing their independent measurement. However, in this case the resolution of the measurement becomes critical, as the slope of temperature rise vs. length from the contacts must be carefully distinguished for accurate parameter measurement.

The speed, versatility, sub-micron resolution and non-destructive nature of Raman spectrometric measurements commend their use for determining other important properties in semiconductor NWs. It was already shown in Chapter 3 that Fano interference provides an extremely rapid estimation of doping levels and axial doping uniformity in highly boron doped Si NWs. Another promising characteristic of Raman spectra is their highly sensitive dependence on crystal strain. Very high piezoresistance coefficients measured in Si NWs [182] and the emergence of strain engineering in leading edge integrated circuit technology [183] make the option of combining in situ Raman spectroscopy with mechanical stress and concurrent electrical measurements particularly enticing. It may even be possible to use Raman spectrometry to determine mechanical resonance behavior in NWs by monitoring peak width as the NW will oscillate between an unstrained and a highly strained state (compression and tension simultaneously) at resonance.

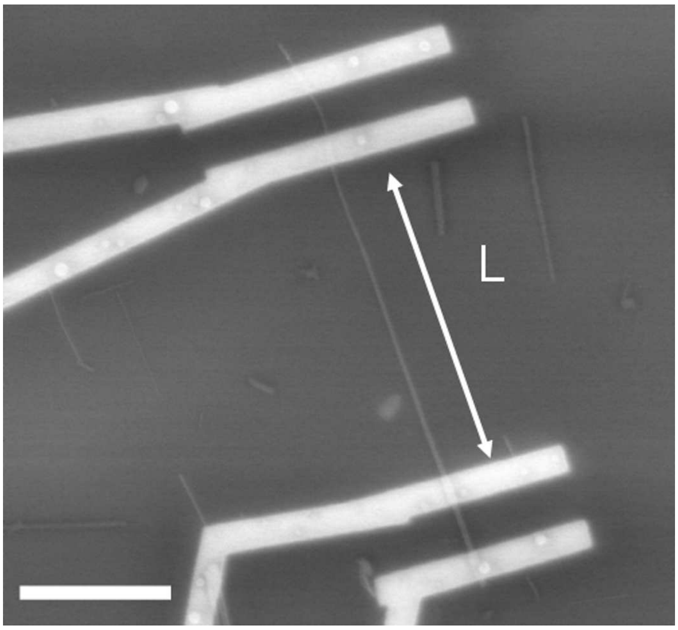

Figure 5.1: Four point probe setup on a single NW that may potentially be used for another thermal conductivity measurement method based on Raman thermography (scale bar = 5 μm)

Bibliography

[1] S. Iijima. Helical microtubules of graphitic carbon. *Nature*, 354(6348):56–58, 1991.

[2] M.S. Gudiksen, L.J. Lauhon, J. Wang, D.C. Smith, and C.M. Lieber. Growth of nanowire superlattice structures for nanoscale photonics and electronics. *Nature*, 415(6872):617–620, 2002.

[3] L.J. Lauhon, M.S. Gudiksen, C.L. Wang, and C.M. Lieber. Epitaxial core-shell and core-multishell nanowire heterostructures. *Nature*, 420(6911):57–61, 2002.

[4] K.A. Dick, K. Deppert, M.W. Larsson, T. Martensson, W. Seifert, L.R. Wallenberg, and L. Samuelson. Synthesis of branched 'nanotrees' by controlled seeding of multiple branching events. *Nature Mater.*, 3(6):380–384, 2004.

[5] D.D.D. Ma, C.S. Lee, F.C.K. Au, S.Y. Tong, and S.T. Lee. Small-diameter silicon nanowire surfaces. *Science*, 299(5614):1874–1877, 2003.

[6] L.Y. Cao, J.S. White, J.S. Park, J.A. Schuller, B.M Clemens, and M.L. Brongersma. Engineering light absorption in semiconductor nanowire devices. *Nature Mater.*, 8(8):643–647, 2009.

[7] L.Y. Cao, P.Y. Fan, A.P. Vasudev, J.S. White, Z.F. Yu, W.S. Cai, J.A. Schuller, S.H. Fan, and M.L. Brongersma. Semiconductor nanowire optical antenna solar absorbers. *Nano Lett.*, 10(2):439–445, 2010.

[8] J. Frechette and C. Carraro. Diameter-dependent modulation and polarization anisotropy in Raman scattering from individual nanowires. *Phys. Rev. B*, 74(16):161404, 2006.

[9] V. Schmidt, S. Senz, and U. Gosele. Influence of the Si/SiO_2 interface on the change carrier density of si nanowires. *Appl. Phys. A: Mater. Sci. Process.*, 86(2):187–191, 2007.

[10] M.T. Bjork, H. Schmid, J. Knoch, H. Riel, and W. Riess. Donor deactivation in silicon nanostructures. *Nature Nanotech.*, 4(2):103–107, 2009.

[11] Y. Cui, Q.Q. Wei, H.K. Park, and C.M. Lieber. Nanowire nanosensor for highly sensitive and selective detection of biological and chemical species. *Science*, 293(5533):1289–1292, 2001.

[12] X.L. Feng, R.R. He, P.D. Yang, and M.L. Roukes. Very high frequency silicon nanowire electromechanical resonators. *Nano Lett.*, 7(7):1953–1959, 2007.

[13] R. Hoffmann. Silicon. *Chem. & Eng. News*, 81(36):27, 2003.

[14] L. Jarup, M. Berglund, C.G. Elinder, G. Nordberg, and M. Vahter. Health effects of cadmium exposure – a review of the literature and a risk estimate. *Scand. J. Work, Environ. Health*, 24(3):240, 1998.

[15] A.I. Kingon, J.P. Maria, and S.K. Streiffer. Alternative dielectrics to silicon dioxide for memory and logic devices. *Nature*, 406(6799):1032–1038, 2000.

[16] B. Jalali, M. Paniccia, and G. Reed. Silicon photonics. *IEEE Microwave Mag.*, 7(3):58–68, 2006.

[17] F.J. Morin and J.P. Maita. Electrical properties of silicon containing arsenic and boron. *Phys. Rev.*, 96(1):28–35, 1954.

[18] C. Kittel. *Introduction to Solid State Physics, 8th ed.* John Wiley & Sons, Inc., New Jersey, 2005.

[19] C. Dames and G. Chen. Theoretical phonon thermal conductivity of Si/Ge superlattice nanowires. *J. Appl. Phys.*, 95(2):682–693, 2004.

[20] C. Dames and G. Chen. Thermal conductivity of nanostructured thermoelectric materials. In *Thermoelectrics Handbook: Macro to Nano.* CRC Press, Taylor and Francis Group, LLC, Boca Raton, FL, 2006.

[21] D.Y. Li, Y.Y. Wu, P. Kim, L. Shi, P.D. Yang, and A. Majumdar. Thermal conductivity of individual silicon nanowires. *Appl. Phys. Lett.*, 83(14):2934–2936, 2003.

[22] N. Mingo, L. Yang, D. Li, and A. Majumdar. Predicting the thermal conductivity of Si and Ge nanowires. *Nano Lett.*, 3(12):1713–1716, 2003.

[23] R. Chen, A.I. Hochbaum, P. Murphy, J. Moore, P.D. Yang, and A. Majumdar. Thermal conductance of thin silicon nanowires. *Phys. Rev. Lett.*, 101(10):105501, 2008.

[24] A.I. Hochbaum, R.K. Chen adn R.D. Delgado, W.J. Liang, E.C. Garnett, M. Najarian, A. Majumdar, and P.D. Yang. Enhanced thermoelectric performance of rough silicon nanowires. *Nature*, 451(7175):163–167, 2008.

[25] P. Martin, Z. Aksamija, E. Pop, and U. Ravaioli. Impact of phonon-surface roughness scattering on thermal conductivity of thin Si nanowires. *Phys. Rev. Lett.*, 102(12):125503, 2009.

[26] M. Kazan, G. Guisbiers, S. Pereira, M.R. Correia, P. Masri, A. Bruyant, S. Volz, and P. Royer. Thermal conductivity of silicon bulk and nanowires: Effects of isotopic composition, phonon confinement, and surface roughness. *J. Appl. Phys.*, 107(8):083503, 2010.

[27] D. Donadio and G. Galli. Atomistic simulations of heat transport in silicon nanowires. *Phys. Rev. Lett.*, 102(19):195901, 2009.

[28] J. Xiang, W. Lu, Y.J. Hu, Y. Wu, H. Yan, and C.M. Lieber. Ge/Si nanowire heterostructures as high-performance field-effect transistors. *Nature*, 441(7092):489–493, 2006.

[29] L.Y. Cao, J.S. Park, P.Y. Fan, B. Clemens, and M.L. Brongersma. Resonant germanium nanoantenna photodetectors. *Nano Lett.*, 10(4):1229–1233, 2010.

[30] M.W. Li, R.B. Bhilvadvala, T.J. Morrow, J.A. Sioss, K.K. Lew, J.M. Redwing, C.D. Keating, and T.S. Mayer. Bottom-up assembly of large-area nanowire resonator arrays. *Nature Nanotech.*, 3(2):88–92, 2008.

[31] E.M. Freer, O. Grachev, X.F. Duan, S. Martin, and D.P. Stumbo. High-yield self-limiting single-nanowire assembly with dielectrophoresis. *Nature Nanotech.*, 5(7):525–530, 2010.

[32] A.K. Shalek, J.T. Robinson, E.S. Karp, J.S. Lee, D.R. Ahn, M.H. Yoon, A. Sutton, M. Jorgolli, R.S. Gertner, T.S. Gujral, G. MacBeath, E.G. Yang, and H. Park. Vertical silicon nanowires as a universal platform for delivering biomolecules into living cells. *Proc. Natl. Acad. Sci. U.S.A.*, 107(5):1870–1875, 2010.

[33] M.D. Kelzenberg, S.W. Boettcher, J.A. Petykiewicz, D.B. Turner-Evans, M.C. Putnam, E.L. Warren, J.M. Spurgeon, R.M. Briggs, N.S. Lewis, and H.A. Atwater. Enhanced absorption and carrier collection in Si wire arrays for photovoltaic applications. *Nature Mater.*, 9(3):239–244, 2010.

[34] T. Bryllert, L.E. Wernersson, L.E. Froberg, and L. Samuelson. Vertical high-mobility wrap-gated InAs nanowire transistors. *IEEE Electron Device Lett.*, 27(5):323–325, 2006.

[35] S. Hu, P.W. Leu, A.F. Marshall, and P.C. McIntyre. Single-crystal germanium layers grown on silicon by nanowire seeding. *Nature Nanotech.*, 4(10):649–653, 2010.

[36] T. Martensson, M. Borgstrom, W. Seifert, B.J. Ohlsson, and L. Samuelson. Fabrication of individually seeded nanowire arrays by vapour-liquid-solid growth. *Nanotechnology*, 14(12):1255–1258, 2003.

[37] H. Schmid, M.T. Bjork, J. Knoch, H. Riel, W. Riess, P. Rice, and T. Topuria. Patterned epitaxial vapor-liquid-solid growth of silicon nanowires on Si(111) using silane. *J. Appl. Phys.*, 103(2):024304, 2008.

[38] A.I. Hochbaum, R. Fan, R.R. He, and P.D. Yang. Controlled growth of Si nanowire arrays for device integration. *Nano Lett.*, 5(3):457–460, 2005.

[39] J.X. Huang, A.R. Tao, S. Connor, R.R. He, and P.D. Yang. A general method for assembling single colloidal particle lines. *Nano Lett.*, 6(3):524–529, 2006.

[40] T. Kraus, L. Malaquin, H. Schmid, W. Riess, N.D. Spencer, and H. Wolf. Nanoparticle printing with single-particle resolution. *Nature Nanotech.*, 2(9):570–576, 2007.

[41] P. Manandhar, E.A. Akhadov, C. Tracy, and S.T. Picraux. Integration of nanowire devices in out-of-plane geometry. *Nano Lett.*, 10(6):2126–2132, 2010.

[42] A. San Paulo, J. Bokor, R.T. Howe, R. He, P. Yang, D. Gao, C. Carraro, and R. Maboudian. Mechanical elasticity of single and double clampled silicon nanobeams fabricated by the vapor-liquid-solid method. *Appl. Phys. Lett.*, 87(5):053111, 2005.

[43] A. Chaudhry, V. Ramamurthi, E. Fong, and M.S. Islam. Ultra-low contact resistance of epitaxially interfaced bridged silicon nanowires. *Nano Lett.*, 7(6):1536–1541, 2007.

[44] D.R. Kim and X.L. Zheng. Numerical characterization and optimization of the microfluidics for nanowire biosensors. *Nano Lett.*, 8(10):3233–3237, 2008.

[45] D.R. Kim, C.H. Lee, and X.L. Zheng. Direct growth of nanowire logic gates and photovoltaic devices. *Nano Lett.*, 10(3):1050–1054, 2010.

[46] E.C. Garnett, Y.C. Tseng, D.R. Khanal, J.Q. Wu, J. Bokor, and P.D. Yang. Dopant profiling and surface analysis of silicon nanowires using capacitance-voltage measurements. *Nature Nanotech.*, 4(5):311–314, 2009.

[47] E. Gil-Santos, D. Ramos, J. Martinez, M. Regulez-Fernandez, R. Garcia, A. San Paulo, M. Calleja, and J. Tamayo. Nanomechanical mass sensing and stiffness spectrometry based on two-dimensional vibrations of resonant nanowires. *Nature Nanotech.*, 5(9):641–645, 2010.

[48] A.D. McConnell and K.E. Goodson. Thermal conduction in silicon micro- and nanostructures. *Ann. Rev. Heat Transfer*, 14:129–168, 2005.

[49] T.Y. Choi, D. Poulikakos, J. Tharian, and U. Sennhauser. Measurement of the thermal conductivity of individual carbon nanotubes by the four-point three-omega method. *Nano Lett.*, 6(8):1589–1593, 2006.

[50] L. Shi, D.Y. Li, C.H. Yu, W.Y. Jang, D. Kim, Z. Yao, P. Kim, and A. Majumdar. Measuring thermal and thermoelectric properties of one-dimensional nanostructures using a microfabricated devices. *J. Heat Transfer*, 125(5):881–888, 2003.

[51] W. Hayes and R. Loudon. *Scattering of Light by Crystals.* John Wiley & Sons, Inc., New York, 1978.

[52] R.S. Wagner and W.C. Ellis. Vapor-liquid-solid mechanism of single crystal growth. *Appl. Phys. Lett.*, 4(5):89–90, 1964.

[53] V. Schmidt, J.V. Wittemann, and U. Gosele. Growth, thermodynamics, and electrical properties of silicon nanowires. *Chem. Rev.*, 110(1):361–388, 2010.

[54] Y. Wu, Y. Cui, L. Huynh, C.J. Barrelet, D.C. Bell, and C.M. Lieber. Controlled growth and structures of molecular-scale silicon nanowires. *Nano Lett.*, 4(3):433–436, 2004.

[55] N. Ferralis, R. Maboudian, and C. Carraro. Temperature-induced self-pinning and nanolayering of AuSi eutectic droplets. *J. Am. Chem. Soc.*, 130(8):2681–2685, 2008.

[56] V. Schmidt, S. Senz, and U. Gosele. Diameter-dependent growth direction of epitaxial silicon nanowires. *Nano Lett.*, 5(5):931–935, 2005.

[57] V. Schmidt, S. Senz, and U. Gosele. Diameter dependence of the growth velocity of silicon nanowires synthesized via the vapor-liquid-solid mechanism. *Phys. Rev. B*, 75(4):045335, 2007.

[58] H.C. Theuerer. Epitaxial silicon films by the hydrogen reduction of $SiCl_4$. *J. Electrochem. Soc.*, 108(7):649–653, 1961.

[59] E.G. Bylander. Kinetics of silicon crystal growth from $SiCl_4$ decomposition. *J. Electrochem. Soc.*, 109(12):1171–1175, 1962.

[60] E. Sirtl, L.P. Hunt, and D.H. Sawyer. High-temperature reactions in silicon-hydrogen-chlorine system. *J. Electrochem. Soc.*, 121(7):919–925, 1974.

[61] C. Carraro, R. Maboudian, and L. Magagnin. Metallization and nanostructuring of semiconductor surfaces by galvanic displacement processes. *Surf. Sci. Rep.*, 62(12):499–525, 2007.

[62] L. Magagnin, R. Maboudian, and C. Carraro. Gold deposition by galvanic displacement on semiconductor surfaces: Effect of substrate on adhesion. *J. Phys. Chem. B*, 106(2):401–407, 2002.

[63] E.I. Givargizov. Fundamental aspects of VLS growth. *J. Cryst. Growth*, 31:20–30, 1975.

[64] M. Ohring. *The Materials Science of Thin Films.* Academic Press, New York, 1991.

[65] S. Kodambaka, J. Tersoff, M.C. Reuter, and F.M. Ross. Diameter-independent kinetics in the vapor-liquid-solid growth of Si nanowires. *Phys. Rev. Lett.*, 96(9):096105, 2006.

[66] S.H. Brewer, W.R. Glomm, M.C. Johnson, M.K. Knag, and S. Franzen. Probin BSA binding to citrate-coated gold nanoparticles and surfaces. *Langmuir*, 21(20):9303–9307, 2005.

[67] M.J. Kosmulski. pH-dependent surface charging and points of zero charge III. Update. *J. Colloid Interface Sci.*, 298(2):730–741, 2006.

[68] J.H. Woodruff, J.B. Ratchford, I.A. Goldthorpe, P.C. McIntyre, and C.E.D. Chidsey. Vertically oriented germanium nanowires grown from gold colloids on silicon substrates and subsequent gold removal. *Nano Lett.*, 7(6):1637–1642, 2007.

[69] S.M. Gates. Adsorption kinetics of SiH_4,Si_2H_6 and Si_3H_8 on the Si(111)-(7x7) surface. *Surf. Sci.*, 195(1-2):307–329, 1988.

[70] P.A. Coon, P. Gupta, M.L. Wise, and S.M. George. Adsorption and desorption kinetics for SiH_2Cl_2 on Si(111)-7x7. *J. Vac. Sci. A*, 10(2):324–333, 1992.

[71] M.T. Borgstrom, G. Immink, B. Ketelaars, R. Algra, and E.P.A.M. Bakkers. Synergetic nanowire growth. *Nature Nanotech.*, 2(9):541–544, 2007.

[72] J.E. Allen, E.R. Hemesath, D.E. Perea, J.L. Lensch-Falk, Z.Y. Li, F. Yin, M.H. Gass, P. Wang, A.L. Bleloch, R.E. Palmer, and L.J. Lauhon. High-resolution detection of Au catalyst atoms in Si nanowires. *Nature Nanotech.*, 3(3):168–173, 2008.

[73] A.R. Guichard, D.N. Barsic, S. Sharma, T.I Kamins, and M.L. Brongersma. Tunable light emission from quantum-confined excitons in $TiSi_2$-catalyzed silicon nanowires. *Nano Lett.*, 6(9):2140–2144, 2006.

[74] K.P. Lisiak and A.G. Milnes. Platinum as a lifetime-control deep impurity in silicon. *J. Appl. Phys.*, 46(12):5229–5235, 1975.

[75] T. Baron, M. Gordon, F. Dhalluin, C. Ternon, P. Ferret, and P. Gentile. Si nanowire growth and characterization using a microelectronics-compatible catalyst: PtSi. *Appl. Phys. Lett.*, 89(23):233111, 2006.

[76] H. Jeong, T.E. Park, H.K. Seong, M. Kim, U. Kim, and H.J. Choi. Growth kinetics of silicon nanowires by platinum assisted vapour-liquid-solid mechanism. *Chem. Phys. Lett.*, 467(4-6):331–334, 2009.

[77] E.C. Garnett, W.J. Liang, and P.D. Yang. Growth and electrical characteristics of platinum-nanoparticle-catalyzed silicon nanowires. *Adv. Mater.*, 19(19):2946–2950, 2007.

[78] M. Cerruti, G.D Doerk, G. Hernandez, C. Carraro, and R. Maboudian. Galvanic deposition of Pt clusters on silicon: Effect of HF concentration and application as catalyst for silicon nanowire growth. *Langmuir*, 26(1):432–437, 2010.

[79] D. Gao, R.R. He, C. Carraro, R.T. Howe, P.D. Yang, and R. Maboudian. Selective growth of Si nanowire arrays via galvanic displacement processes in water-in-oil microemulstions. *J. Am. Chem. Soc.*, 127(13):4574–4575, 2005.

[80] D. Wang, F. Qian, C. Yang, Z.H. Zhong, and C.M. Lieber. Rational growth of branched and hyperbranched nanowire structures. *Nano Lett.*, 4(5):871–874, 2004.

[81] K.A. Dick, K. Deppert, L.S. Karlsson, W. Seifert, L.R. Wallenberg, and L. Samuelson. Position-controlled interconnected InAs nanowire networks. *Nano Lett.*, 6(12):2842–2847, 2006.

[82] A. Lugstein, A.M. Andrews, M. Steinmair, Y.J. Hyun, E. Bertagnolli, M. Weil, P. Pongratz, M. Schrambock, T. Roch, and G. Strasser. Growth of branched single-crystalline GaAs whiskers on Si nanowire trunks. *Nanotechnology*, 18(35):355306, 2007.

[83] T. Kawashima, T. Mizutani, T. Nakagawa, H. Torii, T. Saitoh, K. Komori, and M. Fujii. Control of surface migration of gold particles on Si nanowires. *Nano Lett.*, 8(1):362–368, 2008.

[84] J.B. Hannon, S. Kodambaka, F.M. Ross, and R.M. Tromp. The influence of the surface migration of gold on the growth of silicon nanowires. *Nature*, 440(7080):69–71, 2006.

[85] J. Slezak, M. Ondrejcek, Z. Chvoj, V. Chab, H. Conrad, S. Heun, T. Schmidt, B. Ressel, and K.C. Prince. Surface diffusion of Au on Si(111): A microscopic study. *Phys. Rev. B*, 61(23):16121–16128, 2000.

[86] O.G. Shpyrko, R. Steitel, V.S.K. Balagurusamy, A.Y. Grigoriev, M. Deutsch, B.M. Ocko, M. Meron, B.H. Lin, and P.S. Pershan. Surface crystallization in a liquid AuSi alloy. *Science*, 313(5783):77–80, 2006.

[87] N. Ferralis, F. El Gabaly, A.K. Schmid, R. Maboudian, and C. Carraro. Real-time observation of reactive spreading of gold on silicon. *Phys. Rev. Lett.*, 103(25):256102, 2009.

[88] S. Kodambaka, J.B. Hannon, R.M. Tromp, and F.M. Ross. Control of Si nanowire growth by oxygen. *Nano Lett.*, 6(6):1292–1296, 2006.

[89] F. Oehler, P. Gentile, T. Baron, and P. Ferret. The effects of HCl on silicon nanowire growth: Surface chlorination and existence of a 'diffusion-limited minimum diameter'. *Nanotechnology*, 20(47):475307, 2009.

[90] F.M. Ross, J. Tersoff, and M.C. Reuter. Sawtooth faceting in silicon nanowires. *Phys. Rev. Lett.*, 95(14):146104, 2005.

[91] C. Wiethoff, F.M. Ross, M. Copel, M.H.V. Hoegen, and F.J.M.Z. Heringdorf. Au stabilization and coverage of sawtooth facets on Si nanowires grown by vapor-liquid-solid epitaxy. *Nano Lett.*, 8(9):3065–3068, 2008.

[92] Y.J. Hyun, A. Lugstein, M. Steinmair, E. Bertagnolli, and P. Pongratz. Orientation specific synthesis of kinked silicon nanowires grown by the vapour-liquid-solid mechanism. *Nanotechnology*, 20(12):125606, 2009.

[93] F. Li, P.D. Nellist, and D.J.H. Cockayne. Doping-dependent nanofaceting on silicon nanowire surfaces. *Appl. Phys. Lett.*, 94(26):263111, 2009.

[94] H. Minoda, T. Shimakura, K. Yagi, F.J.M. Heringdorf, and M.H. von Hoegen. Gold-induced faceting on a Si(hhm) surface (m/h-1.4-1.5) studied by spot profile analyzing low-energy electron diffraction. *Surf. Sci.*, 432(1-2):69–80, 1999.

[95] T. David, D. Buttard, T. Schulli, F. Dallhuin, and P. Gentile. Structural investigation of silicon nanowires using GIXD and GISAXS: Evidence of complex saw-tooth faceting. *Surf. Sci.*, 602(15):2675–2680, 2008.

[96] v. Schmidt, S. Senz, and U. Gosele. The shape of epitaxially grown silicon nanowires and the influence of line tension. *Appl. Phys. A*, 80(3):445–450, 2005.

[97] K.W. Schwarz and J. Tersoff. From droplets to nanowires: Dynamics of vapor-liquid-solid growth. *Phys. Rev. Lett.*, 102(20):206101, 2009.

[98] D.J. Eaglesham, A.E. White, L.C. Feldman, N. Moriya, and D.C. Jacobson. Equilibrium shape of Si. *Phys. Rev. Lett.*, 70(11):1643–1646, 1993.

[99] B. Yang, P.P. Zhang, D.E. Savage, M.G. Lagally, G.H. Lu, M.H. Huang, and F. Liu. Self-organization of semiconductor nanocrystals by selective surface faceting. *Phys. Rev. B*, 72(23):235413, 2005.

[100] M.K. Dawood, T.H. Liew, P. Lianto, M.H. Hong, S. Tripathy, J.T.L. Thong, and W.K. Choi. Interference lithographically defined and catalytically etched, large-area silicon nanocones from nanowires. *Nanotechnology*, 21(20):205305, 2010.

[101] K.Q. Peng, Y.J. Yan, S.P. Gao, and J. Zhu. Synthesis of large-area silicon nanowire arrays via self-assembling nanoelectrochemistry. *Adv. Mater.*, 14(16):1164–1167, 2002.

[102] A.I. Hochbaum, D. Gargas, Y.J. Hwang, and P.D. Yang. Single crystalline mesoporous silicon nanowires. *Nano Lett.*, 9(10):3550–3554, 2009.

[103] A.G. Cullis, L.T. Canham, and P.D.J. Calcott. The structural and luminescence properties of porous silicon. *J. Appl. Phys.*, 82(3):909–965, 1997.

[104] A. San Paulo, N. Arellano, J.A. Plaza, R.R. He, C. Carraro, R. Maboudian, R.T. Howe, J. Bokor, and P.D. Yang. Suspended mechanical structures based on elastic silicon nanowire arrays. *Nano Lett.*, 7(4):1100–1104, 2007.

[105] N.J. Quitoriano and T.I. Kamins. Integratable nanowire transistors. *Nano Lett.*, 8(12):4410–4414, 2008.

[106] K.L. Ekinci. Electromechanical transducers at the nanoscale: Actuation and sensing of motion in nanoelectromechanical systems (NEMS). *Small*, 1(8-9):786–797, 2005.

[107] H.B. Peng, C.W. Chang, S. Aloni, T.D. Yuzvinsky, and A. Zettl. Ultrahigh frequency nanotube resonators. *Phys. Rev. Lett.*, 97(8):087203, 2006.

[108] K.I. Seo, S. Sharma, A.A. Yasseri, D.R. Stewart, and T.I. Kamins. Surface charge density of unpassivated and passivated metal-catalyzed silicon nanowires. *Electrochem. Solid-State Lett.*, 9(3):G69–G72, 2006.

[109] R.R. He, X.L. Feng, M.L. Roukes, and P.D. Yang. Self-transducing silicon nanowire electromechanical systems at room temperature. *Nano Lett.*, 8(6):1756–1761, 2008.

[110] R. Lifshitz and M.L. Roukes. Thermoelastic damping in micro- and nanomechanical systems. *Phys. Rev. B*, 61(8):5600–5609, 2000.

[111] M. Aizawa and J.M. Buriak. Block copolymer-templated chemistry on Si, Ge, InP, and GaAs surfaces. *J. Am. Chem. Soc.*, 127(25):8932–8933, 2005.

[112] M. Aizawa and J.M. Buriak. Block copolymer templated chemistry for the formation of metallic nanoparticle arrays on semiconductor surfaces. *Chem. Mater.*, 19(21):5090–5101, 2007.

[113] W. Hwang, J.H. Choi, T.H. Kim, J. Sung, J.M. Myoung, D.G. Choi, B.H. Sohn, S.S. Lee, D.H. Kim, and C. Park. Control of the area density of vertically grown ZnO nanowires by blending PS-b-P4VP and PS-b-PAA copolymer micelles. *Chem. Mater.*, 20(19):6041–6047, 2008.

[114] R.D. Bennett, A.C. Miller, N.T. Kohen, P.T. Hammond, D.J. Irvine, and R.E. Cohen. Strategies for controlling the planar arrangement of block copolymer micelles and inorganic nanoclusters. *Macromolecules*, 38(26):10728–10735, 2005.

[115] S. Forster, M. Zisenis, E. Wenz, and M. Antonietti. Micellization of strongly segregated block copolymers. *J. Chem. Phys.*, 104(24):9956–9970, 1996.

[116] G.S. Doerk, N. Ferralis, C. Carraro, and R. Maboudian. Growth of branching Si nanowires seeded by Au-Si surface migration. *J. Mater. Chem.*, 18(44):5376–5381, 2008.

[117] I. Horcas, R. Fernandez, J.M. Gomez-Rodriguez, J. Colchero, J. Gomez-Herrero, and A.M. Baro. WSxM: A software for scanning probe microscopy and a tool for nanotechnology. *Rev. Sci. Inst.*, 78(1):013705, 2007.

[118] J. Chai and J.M. Buriak. Using cylindrical domains of block copolymers to self-assemble and align metallic nanowires. *ACS Nano*, 2(3):489–501, 2008.

[119] S.H. Yun, S. Il Yoo, J.C. Jung, W.C. Zin, and B.H. Sohn. Highly ordered arrays of nanoparticles in large areas from diblock copolymer micelles in hexagonal self-assembly. *Chem. Mater.*, 18(24):5646–5648, 2006.

[120] T.H. Kim, J. huh, J. Hwang, H.C. Kim, S.H. Kim, B.H. Sohn, and C. Park. Ordered arrays of PS-b-P4VP micelles by fusion and fission process upon solvent annealing. *Macromolecules*, 42(17):6688–6697, 2009.

[121] R. Ruiz, H.M. Kang, F.A. Detcheverry, E. Dobisz, D.S. Kercher, T.R. Albrecht, J.J. de Pablo, and P.F. Nealey. Density multiplication and improved lithography by directed block copolymer assembly. *Science*, 321(5891):936–939, 2008.

[122] I. Bita, J.K.W. Yang, Y.S. Jung, C.A. Ross, E.L. Thomas, and K.K. Berggren. Graphoepitaxy of self-assembled block copolymers on two-dimensional periodic patterned templates. *Science*, 321(5891):939–943, 2008.

[123] K.O. Stuen, C.S. Thomas, G.L. Liu, N. Ferrier, and P.F. Nealey. Dimensional scaling of cylinders in thin films of block copolymer-homopolymer ternary blends. *Macromolecules*, 42(14):5139–5145, 2009.

[124] J.M. Papalia A.P. Marencic, D.H. Adamson, P.M. Chaikin, and R.A. Register. Thin films of block copolymer-homopolymer blends with a continuously tunable density of spherical microdomains. *Macromolecules*, 43(17):6946–6949, 2010.

[125] Y. Cui, X.F. Duan, J.T. Hu, and C.M. Lieber. Doping and electrical transport in silicon nanowires. *J. Phys. Chem. B*, 104(22):5213–5216, 2000.

[126] K.K. Lew, L. Pan, T.E. Bogart, S.M. Dilts, E.C. Dickey, J.M. Redwing, Y.F. Wang, M. Cabassi, T.S. Mayer, and S.W. Novak. Structural and electrical properties of trimethylboron-doped silicon nanowires. *Appl. Phys. Lett.*, 85(15):3101–3103, 2004.

[127] Y.F. Wang, K.K. Lew, T.T. Ho, L. Pan, S.W. Novak, E.C. Dickey, J.M. Redwing, and T.S. Mayer. Use of phosphine as an n-type dopant source for vapor-liquid-solid growth of silicon nanowires. *Nano Lett.*, 5(11):2139–2143, 2005.

[128] H. Schmid, M.T. Bjork, J. Knoch, S. Karg, H. Riel, and W. Riess. Doping limits of grown *in situ* doped silicon nanowires using phosphine. *Nano Lett.*, 9(1):173–177, 2009.

[129] G. Imamura, T. Kawashima, M. Fujii, C. Nishimura, T. Saitoh, and S. Hayashi. Distribution of active impurities in single silicon nanowires. *Nano Lett.*, 8(9):2620–2624, 2008.

[130] D.E. Perea, E.R. Hemesath, E.J. Schwalbach, J.L. Lensch-Falk, P.W. Voorhees, and L.J. Lauhon. Direct measurement of dopant distribution in an individual vapour-liquid-solid nanowire. *Nature Nanotech.*, 4(5):315–319, 2009.

[131] R.A. Schlitz, D.E. Perea, J.L. Lensch-Falk, E.R. Hemesath, and L.J. Lauhon. Correlating dopant distribution and electrical properties of boron-doped silicon nanowires. *Appl. Phys. Lett.*, 95(16):162101, 2009.

[132] E. Koren, Y. Rosenwaks, J.E. Allen, E.R. Hemesath, and L.J. Lauhon. Nonuniform doping distribution along silicon nanowires measured by kelvin probe force microscopy and scanning photocurrent microscopy. *Appl. Phys. Lett.*, 95(9):092105, 2009.

[133] P. Xie, Y.J. Hu, Y. Fang, J.L. Huang, and C.M. Lieber. Diameter-dependent dopant location in silicon and germanium nanowires. *Proc. Natl. Acad. Sci. U. S. A.*, 106(36):15254–15258, 2009.

[134] L. Pan, K.K. Lew, J.M. Redwing, and E.C. Dickey. Effect of diborane on the microstructure of boron-doped silicon nanowires. *J. Cryst. Growth*, 277(1-4):428–436, 2005.

[135] A. Colli, A. Fasoli, C. Ronning, S. Pisana, S. Piscanec, and A.C. Ferrari. Ion beam doping of silicon nanowires. *Nano Lett.*, 8(8):2188–2193, 2008.

[136] S. Hoffmann, J. Bauer, C. Ronning, T. Stelzner, J. Michler, C. Ballif, V. Sivakov, and S.H. Christiansen. Axial p-n junctions realized in silicon nanowires by ion implantation. *Nano Lett.*, 9(4):1341–1344, 2009.

[137] R.A. Beckman, E. Johnston-Halperin, N.A. Melosh, J.E. Green, and J.R. Heath. Fabrication of conducting Si nanowire arrays. *J. Appl. Phys.*, 96(10):5921–5923, 2004.

[138] S. Ingole, P. Aella, P. Manandhar, S.B. Chikkannanavar adn E.A. Akhadov, D.J. Smith, and S.T. Picraux. *Ex situ* doping of silicon nanowires with boron. *J. Appl. Phys.*, 103(10):104302, 2008.

[139] E.A. Haupfear and L.D. Schmidt. Kinetics of boron deposition from $BBr_3 + H_2$. *Chem. Eng. Sci.*, 49(15):2467–2481, 1994.

[140] Z.H. Walker and E.A. Ogryzlo. Rate contstants for the etching of intrinsic and doped polycrystalline silicon by bromine atoms. *J. Appl. Phys.*, 69(4):2635–2638, 1991.

[141] G. Imamura, T. Kawashima, M. Fujii, C. Nishimura, T. Saitoh, and S. Hayashi. Raman characterization of active B-concentration profiles in individual p-type/intrinsic and intrinsic/p-type Si nanowires. *J. Phys. Chem. C*, 113(25):10901–10906, 2009.

[142] F. Cerdeira, T.A. Fjeldly, and M. Cardona. Effect of free carriers on zone-center vibrational modes in heavily doped p-type Si. 2. Optical modes. *Phys. Rev. B*, 8(10):4734–4745, 1973.

[143] E. Anastassakis, A Pinczuk, E. Burnstein, F.H. Pollak, and M. Cardona. Effect of static uniaxial stress on Raman spectrum of silicon. *Solid State Comm.*, 8(2):133–138, 1970.

[144] V. Magidson and R. Beserman. Fano-type interference in the Raman spectrum of photoexcited Si. *Phys. Rev. B*, 66(19):195206, 2002.

[145] G.L. Vick and K.M. Whittle. Solid solubility and diffusion coefficients of boron in silicon. *J. Electrochem. Soc.*, 116(8):1142–1144, 1969.

[146] G. Glass, H. Kim, P. Desjardins, N. Taylor, T. Spila, Q. Lu, and J.E. Greene. Ultrahigh B doping ($<= 10^{22}$ cm^{-3}) during Si(001) gas-source molecular-beam epitaxy: B incorporation, electrical activation, and hole transport. *Phys. Rev. B*, 61(11):7268–7644, 2000.

[147] R.B. Fair. Boron diffusion in silicon - concentration and orientation dependence, background effects, and profile estimation. *J. Electrochem. Soc.*, 122(6):800–805, 1975.

[148] E.B. Ramayya, D. Vasileska, S.M. Goodnick, and I. Knezevic. Electron transport in silicon nanowires: The role of acoustic phonon confinement and surface roughness scattering. *J. Appl. Phys.*, 104(6):063711, 2008.

[149] S.E. Mohney, Y. Wang, M.A. Cabassi, K.K. Lew, S. Dey, J.M. Redwing, and T.S. Mayer. Measuring the specific contact resistance of contacts to semiconductor nanowires. *Solid State Electron.*, 49(2):227–232, 2005.

[150] H.D. Tong, S. Chen, W.G. van der Wiel, E.T. Carlen, and A. van den Berg. Novel top-down wafer-scale fabrication of single crystal silicon nanowires. *Nano Lett.*, 9(3):1015–1022, 2009.

[151] A. Lugstein, M. Steinmair, C. Henkel, and E. Bertagnolli. Scalable approach for vertical device integration of epitaxial nanowires. *Nano Lett.*, 9(5):1830–1834, 2009.

[152] S. Habicht, Q.T. Zhao, S.F. Feste, L. Knoll, S. Trellenkamp, B. Ghyselen, and S. Mantl. Electrical characterization of strained and unstrained silicon nanowires with nickel silicide contacts. *Nanotechnology*, 21(10):105701, 2010.

[153] G. Chen, J. Wu, Q.J. Lu, H.R.H. Gutierrez, Q. Xiong, M.E. Pellen, J.S. Petko, D.H. Werner, and P.C. Eklund. Optical antenna effect in semiconducting nanowires. *Nano Lett.*, 8(5):1341–1346, 2008.

[154] M. Kerker. *The scattering of light, and other electromagnetic radiation.* Academic Press, New York, 1969.

[155] L.Y. Cao, B. Nabet, and J.E. Spanier. Enhanced Raman scattering from individual semiconductor nanocones and nanowires. *Phys. Rev. Lett.*, 96(15):157402, 2006.

[156] R. Gupta, Q. Xiong, C.K. Adu, U.J. Kim, and P.C. Eklund. Laser induced Fano resonance scattering in silicon nanowires. *Nano Lett.*, 3(5):627–631, 2003.

[157] S. Piscanec, M. Cantoro, A.C. Ferrari, J.A. Zapien, Y. Lifshitz, S.T. Lee, S. Hofmann, and J. Robertson. Raman spectroscopy of silicon nanowires. *Phys. Rev. B*, 68(24):241312, 2003.

[158] Z. Su, J. Sha, G. Pan, J. Liu, D. Yang, C. Dickinson, and W. Zhou. Temperature-dependent Raman scattering of silicon nanowires. *J. Phys. Chem. B*, 110(3):1229–1234, 2006.

[159] Y. Chen, B. Peng, and B. Wang. Raman spectra and temperature-dependent Raman scattering of silicon nanowires. *J. Phys. Chem. C*, 111(16):5855–5858, 2007.

[160] Y. Pauleau, F.C. Dassapa, P. Lami, J.C. Oberlin, and F. Romagna. Silicide formation in metal/Si structures and diffusion barrier properties of CVD tungsten films. *J. Mater. Res.*, 4(1):156–162, 1989.

[161] H.H. Burke and I.P. Herman. Temperature dependence of Raman scattering in $Ge_{1-x}Si_x$ alloys. *Phys. Rev. B*, 48(20):15016–15024, 1993.

[162] M. Balkanski, R.F. Wallis, and E. Haro. Anharmonic effects in light scattering due to optical phonons in silicon. *Phys. Rev. B*, 28(4):1928–1934, 1983.

[163] J. Menendez and M. Cardona. Temperature dependence of the first-order Raman scattering by phonons in Si, Ge, and alpha-Sn: Anharmonic effects. *Phys. Rev. B*, 29(4):2051–2059, 1984.

[164] V.V. Brazhkin, S.G. Lyapin, I.A. Trojan, R.N. Voloshin, A.G. Lyapin, and N.N. Mel'nik. Anharmonicity of short-wavelength acoustic phonons in silicon at high temperatures. *JETP Lett.*, 72(4):195–198, 2000.

[165] J.S. Tse, D.D. Klug, J.Y. Zhao, W. Sturhahn, E.E. Alp, J. Baumert, C. Gutt, M.R. Johnson, and W. Press. Anharmonic motions of Kr in the clathrate hydrate. *Nature Mater.*, 4(12):917–921, 2005.

[166] M. Christensen, A.B. Abrahamsen, N.B. Christensen, F. Juranyi, N.H. Andersen, K. Lefmann, J. Andreasson, C.R.H. Bahl, and B.B. Iversen. Avoided crossing of rattler modes in thermoelectric materials. *Nature Mater.*, 7(10):811–815, 2008.

[167] G.P. Srivastava. Phonon conductivity of insulators and semiconductors. *J. Phys. Chem. Solids*, 41(4):357–368, 1980.

[168] M. Kazan, S. Pereira, J. Coutinho, M.R. Correia, and P. Masri. Role of optical phonons in Ge thermal conductivity. *Appl. Phys. Lett.*, 92(21):180302, 2008.

[169] M. Kazan, S. Pereira, M.R. Correia, and P. Masri. Contribution of the decay of optical phonons into acoustic phonons to the thermal conductivity of AlN. *Phys. Rev. B*, 77(18):105–114, 2008.

[170] A.A. Balandin, S. Ghosh, W.Z. Bao, I. Calizo, D. Teweldebrhan, F. Miao, and C.N. Lau. Superior thermal conductivity of single-layer graphene. *Nano Lett.*, 8(3):902–907, 2008.

[171] I.K. Hsu, M.T. Pows, A. Bushmaker, M. Aykol, L. Shi, and S.B. Cronin. Optical absorption and thermal transport of individual suspended carbon nanotube bundles. *Nano Lett.*, 9(2):590–594, 2009.

[172] Y.S. Ju and K.E. Goodson. Phonon scattering in silicon films with thickness of order 100 nm. *Appl. Phys. Lett.*, 74(20):3005–3007, 1999.

[173] D.G. Cahill, W.K. Ford, K.E. Goodson, G.D. Mahan, A. Majumdar, H.J. Maris, R. Merlin, and S.R. Phillpot. Nanoscale thermal transport. *J. Appl. Phys.*, 93(2):793–818, 2003.

[174] B.K. Sun, Z. Xiang, and C.P. Grigoropoulos. Spectral optical functions of silicon in the range of 1.13-4.96 eV at elevated temperatures. *Int. J. Heat Mass Transfer*, 40(7):1591–1600, 1997.

[175] F.B. Hildebrand. *Advanced Calculus for Applications.* Prentice Hall, New York, 1964.

[176] I.K. Hsu, R. Kumar, A. Bushmaker, S.B. Cronin, M.T. Pettes, L. Shi, T. Brintlinger, M.S. Fuhrer, and J. Cumings. Optical measurement of thermal transport in suspended carbon nanotubes. *Appl. Phys. Lett.*, 92(6):063119, 2008.

[177] E. Pop, D.A. Mann, K.E. Goodson, and H.J. Dai. Electrical and thermal transport in metallic single-wall carbon nanotubes on insulating substrates. *J. Appl. Phys.*, 101(9):093710, 2007.

[178] D.R. Wright, D.C. Hartman, U.C. Sridharan, M. Kent, T. Jasinski, and S. Kang. Low temperature etch chuck: Modeling and experimental results of heat transfer and wafer temperature. *J. Vac. Sci. Technol. A*, 10(4):1065–1070, 1992.

[179] R. Piejak, V. Godyak, B. Alexandrovich, and N. Tishchenko. Surface temperature and thermal balance of probes immersed in high density plasma. *Plasma Sources Sci. Technol.*, 7(4):590–598, 1998.

[180] A.L. Moore, S.K. Saha, R.S. Prasher, and L. Shi. Phonon backscattering and thermal conductivity suppression in sawtooth nanowires. *Appl. Phys. Lett.*, 93(8):083112, 2008.

[181] T. Markussen, A.P. Jauho, and M. Brandbyge. Surface-decorated silicon nanowires: a route to high-ZT thermoelectrics. *Phys. Rev. Lett.*, 103(5):055502, 2009.

[182] R.R. He and P.D. Yang. Giant piezoresistance effect in silicon nanowires. *Nature Nanotech.*, 1(1):42–46, 2006.

[183] M. Chu, Y.K. Sun, U. Aghoram, and S.E. Thompson. Strain: A solution for higher carrier mobility in nanoscale MOSFETs. *Annu. Rev. Mater. Res.*, 39:203–229, 2009.

Appendix A

Electron Beam Lithography Procedure

Generating DXF Files:

1. Open up Photomask.svg in Inkscape (or similar program like Adobe Illustrator, etc).
2. Open up SEM/optical image of NWs in electrode area. Adjust transparency and scale appropriately to align this image to the photomask pattern.
3. Draw Bezier curves over the NWs that you are interested in or may obstruct the path of metal lines to the NWs of interest.
4. When finished, save as a new .svg file.
5. Also save as a .dxf file (user better better dxf format).
6. Open up DesignCAD.
7. Import the .dxf file you created. Check that it looks good.
8. Save as a .dc2 file. Save as DesignCAD 2D ASCII and append .dc2 extension to file name.

Adjusting DC2 Files:

1. If you have not done this in DesignCAD (above) then, convert .dxf files to .dc2 files.
   This may not work properly with dxf files that arent from DesignCAD.
   Run DCFiles.exe.
   Dxf file = input.
   Dc2 file = output.
   *Do not include file name extensions.

2. Open .dc2 file.
3. Zoom out "z", set zoom factor (ex. = 0.5).
4. Zoom to selection:
   Enter → zw.
   Select area of interest with mouse cursors.
5. Set scale to actual μm units:
   Have measured distance between alignment markers available.
   Select → Select all.
   Move/Copy → Select scale.
   Enter.

$$Xscalefactor = \frac{ActualXdistance(in\mu m)}{DesignCADdistance} \tag{A.1a}$$

$$Yscalefactor = \frac{ActualYdistance(in\mu m)}{DesignCADdistance} \tag{A.1b}$$

6. Repeat steps 3 and 4.
7. Recenter:
   Select → Select all.
   Right click by lower left (LL) alignment marker.
   Move/Copy → Move.
   Left click at location for LL alignment marker that makes contact pad area symmetric about the origin.
   Enter.
8. Zoom out (repeat steps 3 and 4).
9. Change layer.
   Press "L" (or go to "Layer Options").
   Change current layer to 2 (or higher if desired).
   Press F2.
10. Draw lines.
    Press "V"
    Click points of line → Press Enter when done with line.
11. Set layer parameters.
    Go to Layer Options.
    F6 → Select layer # (X) → Set color to #X.
    F10 → Set line width (0.25 results in ~400 nm lines, 0.625 → ~1 μm lines).
    F2.

12. Exit.
    Press F8.
    When prompted save the file as "C:\DC6\Filename".

13. Move the file to a floppy disk.

Sample Preparation:

1. Disperse NWs onto sample.

2. UVO clean for ∼30 minutes.

3. Clean chips → immerse in acetone and dry with N_2

4. Spin on MMA:
   Use a couple of drops from a regular pipette.
   Spin at 4000 rpm for 1 min.
   Bake at 120–180 ° for > 1 min. (this may need to be redetermined depending on the hot plate used).

5. Spin on PMMA, same conditions as for MMA.

6. Make sure the middle of the chip is coated uniformly.

7. Check wires of interest under an optical microscope.

Pattern Writing (alignbx2 and amark2 files are in DC6 folder of XPS computer)

1. Copy pattern files to directory on NPGS computer:
   DIR → lists directories.
   mkdir directoryname → makes a directory called "directoryname".
   cd .. → goes back 1 step.
   cd directoryname → goes to directory called "directoryname".
   copy name.ext c:\destination → copes file name.ext to folder "destination".
   floppy disk = A:.
   * = wildcard character.
   A:*.* c:\destination → copies all files in A: to folder "destination".

2. Align SEM as described in Jeol107 manual.
   Focus on scratch first.
   Use slow scan to make patterns more clear.
   Do alignments and focusing away from NW region.
   Image (and write) at ∼10–12 pA.
   Nominal stigmation values are: X = 21, Y = -177.

3. Set magnification to 550X.

4. Switch to slow scan mode.

5. Coarse alignment:
   mrf alignbx2 (read = y, next = n). Area does = 100 μC/cm^2, line spacing = center to center distance = 100 nm.
   When ready to align/write, set beam blank to external and toggle from SEM to NPGS. Remember also to remove the PCD (Faraday cup) immediately before writing.
   pg alignbx2 (runs alignbx2). Remember to press "p" if you set the mode to "p" (i.e. Pause only for p).
   Quickly write over box that appears on the screen with a Sharpie.
   Return to image mode. Quickly match box on substrate to written box.

6. Fine alignment.
   mrf amark2
   Set mode to "w" for all layers (setting on top line for each layer).
   Remember to note that this is an alignment file.
   Area does = 100 μC/cm^2.
   Line spacing = center to center distance = 100 nm.
   Set beam blank to external and toggle from SEM to NPGS. Remove the PCD immediately before writing.
   al amark2 . Do fine alignment.

7. Write pattern.
   mrf pattern ("pattern" is pattern file name).
   Set the mode to "p" for the layer you want to write. Set to "s"(skip) for any layers you do not want to write.
   Area dose = 650 μC/cm^2.
   Line spacing = center to center distance = 100 nm.
   pg pattern a (a → the file is aligned using your previous alignment). Remember to press "p" to actually write.

8. When finished, wipe Sharpie marks off of SEM screen.

9. Shut down the microscope as described in the manual.